Strategy for emissions - and instability prevention in gas turbines

vorgelegt von
Diplom-Ingenieur (TU Berlin),
Peter Albrecht,
aus Berlin

Von der Fakultät V - Verkehrs- und Maschinensysteme der
Technische Universität Berlin
zur Erlangung des akademischen Grades

Doktor der Ingenieurwissenschaften
-Dr.-Ing.-

genehmigte Dissertation

Promotionsausschuss:

Vorsitzender:	Prof. D. Peitsch
Gutachter:	Prof. C. O. Paschereit
Gutachter:	Prof. F. Dinkelacker
Gutachter:	Prof. E. Gutmark

Tag der wissenschaftlichen Aussprache: 11. Juni 2010

Berlin 2010
D83

Abstract

Well-distributed premixed flames within the combustion chamber have shown to be less sensitive for thermo-acoustic instabilities. The assumption can be derived from tests done in this study and might be traced back to reduced local heat release rates so that the feeding energy for p' excitation is not able to overcome the dissipation losses. It is interesting to note that several basic investigations of the swirl-stabilized premix combustion show a spreading of the flame without any pilot injection near the LBO limit. To preserve an efficient combustion process and the spreading of the flame over a wide operating range, a strategy for instability control and NO_x emission reduction is proposed. Thereby, the main flame is supported by premix pilot flames that were located at the apex of the burner and/or at the combustor dump. It can be concluded that pilot premix flames at the burner apex represents an adequate tool for local extinction prevention. Note, the conventional spark plug used for pilot mixture ignition in this study erode very fast. To overcome this problem, either spark plugs with higher lifing or a laser-induced ignition system is proposed. The latter could be installed outside of the combustion chamber while the laser beams are directed through one of the cooling boreholes into the recirculation zones. Moreover, tests with the pilot ring located at combustor dump have shown that the initial p' increase could be delayed to a richer mixture without an increase in NO_x emissions. For industrial applications, the pilot ring, in conjunction of a laser-induced ignition system or high-lifing spark plugs, seem to be the best choice to control the p' level without NO_x increase and to prevent local extinction near the lean limit.

lean premix combustion, swirl burner, NO_x emission, thermoacoustic instabilities, combustion control, premixed pilotflame, spark plug

Zusammenfassung

Eine breit „verschmierte“ Flammenfront innerhalb der Brennkammer in axialer Richtung scheint weniger anfällig gegenüber thermo-akustischen Instabilitäten zu sein. Diese Annnahme lässt sich aus Testergebnissen in dieser Studie und auch aus älteren Studien ableiten und dürfte auf ein niedriges lokales Wärmefreisetzungsniveau zurück zuführen sein, was die Druckschwankungen nicht weiter anzufachen vermag. Derartige Verbrennungszustände findet man nahe der Verlöschgrenze vor, wo sich die Flammenfront von vielen Drallbrennern weiter im Brennraum verteilt. Um eine derartige Verteilung der lokalen Wärmefreisetzungsrate auch noch bei mageren oder bei fetteren Betriebspunkten unter Voraussetzung einer effizienten Verbrennnung (niedrige Konzentrationen an Kohlenmonoxid CO und unverbrannten Kohlenwasserstoffen UHC) aufrecht zu erhalten, wird in dieser Studie eine Strategie zur Instabilitätskontrolle und zur Vermeidung von NO_x Emissionen vorgeschlagen. Dabei wird die Hauptflamme durch Pilot Vormischflammen stabilisiert, die am Brennerkopf und am Brenneraustritt installiert worden sind. Aus den Ergebnissen der atmospherischen Verbrennungsuntersuchungen lässt sich zusammenfassen, dass eine installierte Pilot-Vormischflamme am Brennerkopf sehr gut zur Vermeidung von lokalen Verlöschen herangezogen werden kann, ohne die NO_x Emissionen ansteigen zu lassen. Die dabei verwendete konventionelle Zündkerze verschleißt aber selbst unter atmospherischen Bedingungen viel zu schnell als das es für eine Anwendung in einer Gasturbine in Frage kommen würde. Als Alternative wird ein Laserinduziertes Zündsystem vorgeschlagen, dass ausserhalb der Brennkammer installiert werden könnte und einen Laserstrahl durch eine Bohrung (z.B. Kühlluftbohrung) in den Brennraum leitet. Ausserdem zeigen Tests mit einem Pilotring am Austritt des Drallbrenners, dass der erwartete Anstieg der Druckamplituden zu fetteren Gemischen verzögert werden kann, ebenfalls ohne die NO_x Emissionen ansteigen zu lassen. Für industrielle Anwendungen wäre der Pilotring in Zusammenhang mit einem Laser-induzierten Zündsystem oder einer sehr verschleißarmen Zündkerze besonders geeignet, um einerseits die Druckamplituden ohne NO_x Anstieg zu kontrollieren und andererseits das lokale Verlöschen nahe der Verlöschgrenze zu verhindern.

Magerverbrennung, Vormischverbrennung, Drallbrenner, NO_x Emission, thermoakustische Instabilitäten, Verbrennungskontrolle, vorgemischte Pilotflamme, Zündkerze

Contents

List of Figures

List of Tables

Chapter 1

Introduction

Today's gas turbine technology is established in a wide range of applications, especially for thrust generation in aircraft and for producing electrical power. It is often used for driving all kinds of mechanical moving parts such as pumps and compressors. The greatest advantages of gas turbines against other powering systems e.g. steam turbine systems and piston engine systems, are low mass, compact design and low intial costs based on power output. Moreover, gas turbines are air-breathing devices and can be used in nearly all environments while the operation of steam turbines is restricted to places where a high amount of water for process cooling can be provided e.g. nearby rivers and lakes. Another advantage of today's gas turbines are the low emission characteristic for soot, SO_2 and NO_x, gas turbines are able to keep below environmental emission restriction without additional cleaning devices. Significant increased passenger numbers during the last twenty years and the common wish to cover great distances in shorter times increase the demand on gas turbines for passenger and business aircraft [6]. These kind of thrust units is the only one in the world that is able to accelerate today's aircraft to nearly the speed of sound ($M = 0.8 - 0.9$) also at high altitude (up to 18 km) while the fuel consumption can be kept to a moderate level. The reason can be found in significantly reduced friction losses at that flight level and can be mainly attributed to low molecular viscosity and density. Due to stringent environmental emissions restrictions and increasing fuel prices expected in the future, comercial aircraft and gas turbine design might be more optimized towards extremely low fuel consumptions than maximum flight speed. New gas turbines concepts e.g. open rotor gas turbines, combined with new combustion concepts, and new aircraft design concepts e.g. blended wing body design are able to reduce significantly the fuel consumption and the emissions at $M = 0.7 - 0.8$. The increased demand on stationary gas turbines for electrical power generation was especially driven during the last three decades by the increased demand on power-peaking units ([23], [36]). This is especially the case in countries with a high number of power-peaking devices e.g. air condition systems and a high amount of renewable energy sources that generate unexpected fluctuations in power generation or consumption. The demand on power peaking units increases dramatically in 2006 when the river levels were at extremely low levels in some parts of U.S.A. during the dry summer months and an efficient cooling of steam power plant and nuclear power plants could not be guaranteed anymore. During these weeks, all stationary gas turbines in these region had to be operated in order to compensate the reduced power output from main power stations and to provide additional electricity power for the air-conditioning systems. Temporarily, the price per kWh for electricity from gas turbines increases by a factor of 30 when compared to regular electricity prices within this period [36]. Gas turbines are also attractive for countries where the power grid is not well developed, but the electricity

consumption grows locally extremely fast e.g. in some Arabian and Asian countries such as United Emirates, China and India. In most cases, the gas turbine manufacturer are able to deliver customer-specified solutions that give the customer the opportunity to increase the power output in the future by a second gas or a steam turbine.
To compensate for the expected increase in electrical power consumption in the future, gas turbines combined with steam turbines, called combined cycle power plants become an alternative solution beside conventional steam power plants in terms of power output, cycle efficiency and emissions. Today's biggest gas turbine, SGT5-8000H designed to operate in a combined cycle is manufactured by Siemens and has a power output of 340 MW in single mode and an expected power output in combined cycle of 530 MW while the cycle efficiency is assumed to be over 60 % in combined cycle mode [78]. Currently, tests are being conducted in Irsching (Germany) and will be completed in 2011. This kind of gas turbine generation is able to deliver similar power output to a steam turbine and is, therefore, capable of use for producing electrical power for base-load duties. It can be strongly expected for the future that the number of combined-cycle power plants will increase continuously and will replace some older steam powerplants due to its greater range of power output, moderate costs and extremely low emissions without additional cleaning devices e.g. filters.

It can be concluded that the fuel consumption for producing thrust and electrical power by gas turbines will significantly increase in the future and will, therefore, be responsible for a world-wide emission increase of NO_x and CO_2. Other emissions like sulfur dioxides (SO_2), soot and unburnt hydrocarbons (UHC) are not longer significant at today's gas turbines. While nitrous oxides NO_x are toxic for human beings, carbon dioxide CO_2 generated by fossil-fuels will intensify the greenhouse effect that is responsible for global warming. Therefore, it is essential to develop emission reduction methods that prevent a further increase of wold-wide pollution even though the demand on electrical power will steady increase in the future. An overview of emission reduction measures is now presented.

1.1 Nitrous oxides and carbon dioxide reduction measures for gas turbines

Numerous measures to reduce CO_2 and especially NO_x emissions are summarized e.g. in [15] while the most effective ones for gas turbine base on the adaptation of flame temperature. Other measures are either less suitable for gas turbines or might be used in some decades, first, and will be not further discussed in this chapter.
It can be shown in general that increasing flame temperatures let decrease the CO_2 emissions while NO_x emissions will increase. To understand the contrary behavior, the CO_2 and NO_x formation will be explained shortly. CO_2 emissions are generated during chemical reaction between fossil fuels containing Carbon, C, and Oxygen, O_2, and can not be completely prevented. To minimize these emissions, fuel with reduced or without Carbon content can be chosen or the amount of fuel consumption can be reduced by increasing the cycle efficiency. Most manufacturers try to combine both options by increasing the flexibility of the gas turbine in burning fuels. To lower the fuel consumption and, hence, increase cycle efficency, the combustor inlet presssure and the combustion inlet temperature should be increased (see Figure 1.1). Today's gas turbines with pressure ratios up to $30-50$ achieve further increase in cycle efficiency only when combustion temperature is further increased but the NO_x formation is

strongly affected by the temperature level and by the residence time of the exhaust gases within the combustion chamber [98, 102]. There are three explored and accepted mechanisms for NO_x production, the prompt NO, the fuel NO and thermal NO whereas the latter one is the most relevant for gas turbine engine combustion using kerosine, oil or natural gas [15]. In general, the gas turbine combustion takes place at flame temperatures higher than 1370 K where the thermal NO formation is the predominant mechanism. This mechanism was presented firstly by Zeldovich [103] and is, therefore, also well known as the Zeldovich mechanism. Depending on the residence time and the flame temperature, the NO_x emissions can achieve extreme concentrations within the exhaust gases, especially at flame temperature greater than 2200 K where only milliseconds of residence time are nescessary to generate a considerable amount of NO_x emissions. At flame temperatures of 1800 K, the residence time of products of combustion can achieve some seconds to produce the same amount of NO_x emissions. For this reason, most of the NO-reducing techniques try to reduce peak temperatures and try to keep the residence time and the oxygen concentration within the primary combustion zone (near the burner) low. It can be concluded that one promising way to reduce CO_2 emissions and NO_x emissions simultaneously is a further optimization of the combustion process where high flame temperatures can exist within the primary zone while the residence time of combustion products is kept extremely low.

In the beginning of the gas turbine age (1900-1970), emission restriction didn't exist and gas turbines were designed primarily for high cycle effiency[1], wide operating range and high reliability. The first patent for a gas turbine was given to the german Franz Stolze in 1897. His gas turbine still had a negative cycle efficiency i.e. the compressor needs more energy than the turbine was able to deliver, but, he motivated others to further investigate this kind of power generation. Some years later, the first real gas turbine could be designed with $2-3$ % cycle efficiency. Impressive cycle efficiency increases could be achived when more heat-restistant materials and cooling methods were available. Since the beginning of the 1930's, both, the English F. Whittle and the German H.-J. von Ohain had developed independly an improved gas turbine for aircraft that was commissioned in the same year, 1937. In the same period, the first stationary gas turbine from BBC in Switzerland was also commissioned that has a power output of 4 MW. In the following years, engineers concentrated on increasing the cycle efficiency by increasing combustion inlet pressure and combustion inlet temperature. The relationship between the two parameters is presented in Fig. 1.1 and in the following equation 1.1 [51]

$$\eta_{th} = \frac{\frac{T_3}{T_1}\eta_{s,T}\eta_{s,V} - \Pi^m}{\frac{T_3}{T_1}\eta_{s,V} - \Pi^m + (1-\eta_{s,V})} \cdot \frac{\Pi^m - 1}{\Pi^m} \tag{1.1}$$

with

T_3	Combustion chamber inlet temperature
T_1	Ambient temperature
$\eta_{s,T}$	Turbine efficiency
$\eta_{s,V}$	Compressor efficiency
Π	Pressure ratio of the compressor
m	$m = \frac{\kappa - 1}{\kappa}$ with ratio of specific heats $= \frac{c_p}{c_v}$ κ

Primarily, the cycle efficiency is influenced by the combustor inlet pressure and subsequently

[1] Note, higher cycle efficiency is directly linked with less carbon dioxide emission as lower fuel consumption is needed to generate the same power output.

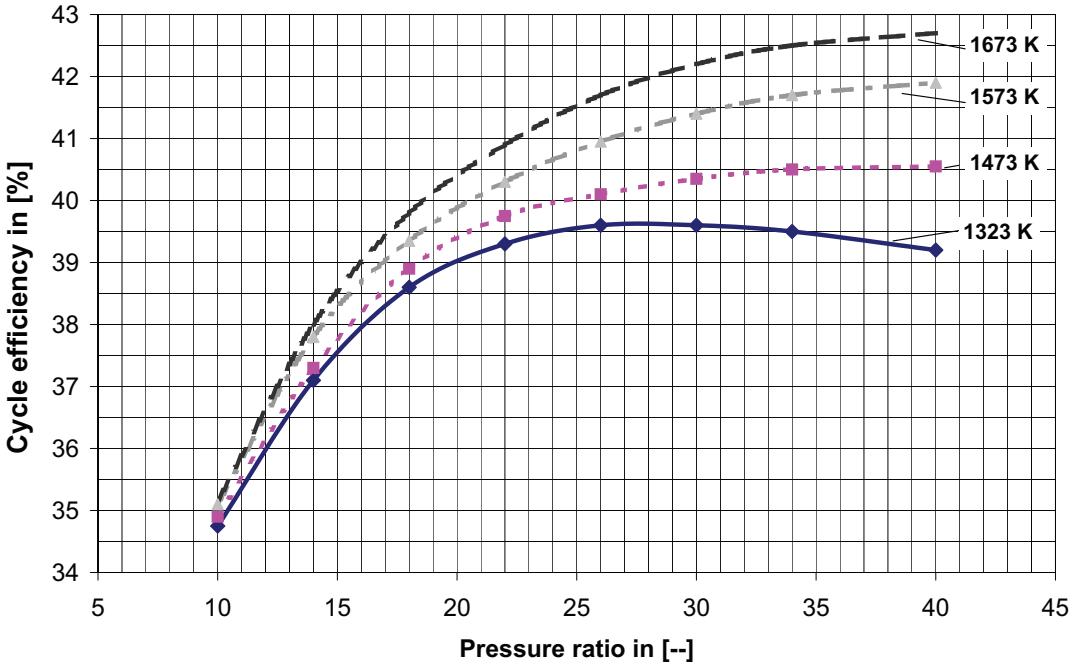

Figure 1.1: Cycle efficiency at different pressure ratios and combustor inlet temperatures. The pressure ratio is defined as the ratio between compressor inlet and combustor inlet pressure [79].

by the inlet temperature. A pressure ratio increase from 10 to 20 is more efficent in term of the cycle efficiency increase than a pressure ratio increase from 20 to 30. While at a lower pressure ratio difference, the cycle efficiency could be increased to 5.5 %, only 0-2.5 % could be achieve for the higher pressure ratio depending on the combustion temperature. At pressure ratios higher than $10-20$, the efficiency can be further increased by increasing the combustion inlet temperature.

The first emission reduction measure for soot, CO and NO_x were taken into account at stationary gas turbine development in the beginning of 1970, when human health and nature conservation became a major issue in politics [12]. At this time, gas turbines were operated using diffusion flames. The risk of flash backs is minimized with this kind of flames as fuel and air is seperately injected into the combustion chamber and the flame can be well stabilized within the shear layer of the fuel and air flow. This kind of flames generate a high amount of NO_x emission due to its extremely high temperatures. The NO_x mechanism is explained in more detail in section 4.5.1. To reduce the NO_x emissions without new combustion concepts, gas turbine manufacturer added water into the combustion zone to reduce the flame temperature. Dramatic reduction in emission of nitrous oxides (NO_x) could be achieved after 1979 first when the stationary gas turbine manufacturer were forced by the governments to develop low-emission burners for their gas turbines [39]. Unfortunately, the low-emission burners are prone to instabilities so that existing pressure fluctuations within the flow can be intensified at certain phase shifts (details are discussed in section 4.6). The instabilities can result in pressure fluctuations with high amplitudes and are able to damage or even destroy parts of

the combustion chamber and other parts. To control these instabilities, today's stationary gas turbines are equipped with active and passive control systems. An overview of these systems is given in [69, 70]. So far, these systems can fail (e.g. power failure) or are designed only for defined operating points so that these systems are not inherent i.e. the system is not able to stabilize by itself. In worst cases, the gas turbine has to be completely shut down even though control systems were embedded. This might be one reason why this combustion type is not established in a flight gas turbine. To prevent instabilities and to have extremely low NO_x emissions, flameless combustion was proposed as an alternative to premixed combustion. The combustion takes place simultaneaously in the entire combustion chamber; its heat release rate is well distributed within the entire combustion chamber which significantly reduces the danger of pressure pulsations (see also section 2.2). This is also the reason why the flame becomes invisible to the human eyes and explains the definition "flameless". This combustion requires a long combustion chamber to guarantee complete combustion that may only be realized in stationary gas turbines and not in flight gas turbines. Another disadvantage is the extremely low flame temperature that has negative effects on the cycle efficiency and results in increased CO_2 emissions.

1.2 Motivation of this work

Lean premixed combustion established in gas turbines for emission reduction is susceptible to thermo-acoustic instabilities (low dynamic stability) and prone to lean blow out (low static stability). To prevent unstable conditions, control strategies with failsafe running functions and with low emission characteristics (NO_x, CO, CO_2 and UHC[2]) are highly desirable e.g. for aircraft engines that require very durable and light weight components with no moving parts. In this study an avoidance strategy for pressure pulsation and NO_x emissions is proposed that might have the potential to fulfill the requirements. The basic idea of the strategy is the use of a premixed pilot[3] to sustain a well distributed heat release rate within the combustion chamber that is less sensitive to thermo-acoustic instabilities. Preliminary combustion investigations have shown that:

1. The pilot equivalence ratio, Φ_{Pilot}, can be adapted in that way that local flame temperature peaks that are mainly responsible for NO_x formation can be prevented.

2. Premixed pilot flames can be used for lean blow out extension.

3. Premixed pilot can suppress pressure oscillation excitation by influencing the heat release distribution.

4. Some of the swirl-stabilized combustors common used in industrial gas turbines show a spreading of the flame front extremely close to the lean blow out (LBO) limit linked with reduced amplitude of pressure oscillations.

All mentioned advantages are combined within the avoidance strategy to guarantee both, low NO_x emissions and low RMS pressure level, at every operating point without using error-prone components.

[2] Unburned Hydro-Carbons

[3] The premixed pilot represents an additional fuel/air injection into the combustion chamber.

1.3 Outline

In this study, the potential of the avoidance strategy will be proven in terms of its practicability for gas turbine applications. Thereby, the focus is directed towards the following questions:

1. Do swirl-stabilized combustors show a low pulsation level near LBO in general, independent of the boundary condition within the combustion chamber? (see section 2)

2. How effective is the premixed pilot in terms of local extinction prevention, NO_x emission reduction and thermo-acoustic instability suppression when compared to the conventional pilot diffusion? (see section 6.2 and 6.3)

3. What is the mechanism of low pulsation behavior near lean blow out and the suppressing effect of premixed pilot? (see section 6.3.4)

The use of an atmospheric test rig facility and the measurement techniques will be described in section 3 and 4 while the premixed pilot flame generation will be discussed in section 5. Finally, the advantages of the avoidance strategy with different control methods are presented in section 6.

Chapter 2

State of the art

The typical pulsation behavior of the generic EV-10 swirl-stabilized combustor (Alstom) will be discussed in detail in this work. The tests were conducted at different main air mass flow rates, different preheated main air temperatures and at atmospheric conditions. In all test cases, a typical pulsation behavior of the combustor near LBO could be observed (Fig. 2.1). While the combustion at richer mixtures is typically stable with low pulsation level (region 5)

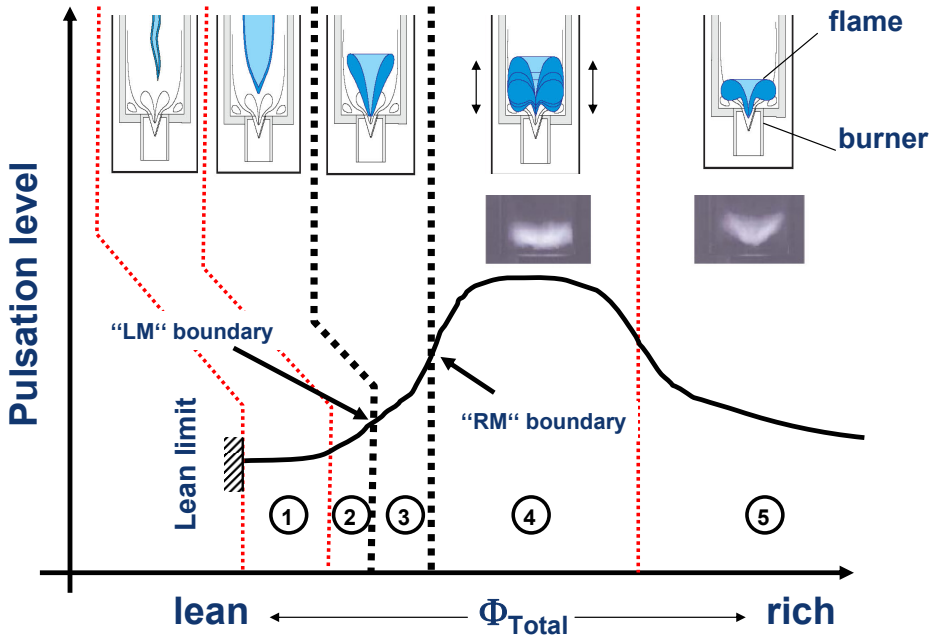

Figure 2.1: Typical pulsation behavior of different industrial swirl-stabilized burners and corresponding flame fronts for different equivalence ratios, Φ_{Total}. Region 3, located between the "Lean mixture (LM)" and "Rich mixture (RM)" boundary, is proposed as an operating range for gas turbines where low pressure oscillations and high thermal efficiency can be achieved. The sketches and images of the flame front were taken from [27] and [29].

and is characterized by a compact and attached flame, the pulsation level increased rapidly into leaner mixtures and became unstable (region 4). The flame at these conditions differs significantly from the stable case as it was also shown in [27, 29, 92, 37] and jumped forth and back periodically in axial direction. If the operating point is shifted further towards leaner mixture (region 3), the pulsation level decreases rapidly and the flame starts to lift up from the combustor dump when compared to the flames at richer mixture. Similar flames close to

the lean blow out could be also detected by Prakash [75] and Taupin [99]. Extremely close to the lean blow out (region 2 and region 1), the flame lifts up completely but stabilizes along the centreline further downstream again with a length of up to several burner diameters, depending on Φ_{Total}. A similar pulsation behavior can be also detected in other swirl-burner geometries as will be shown in the next section.

2.1 Stability maps of different swirl stabilized combustors

A single swirl burner (ALSTOM EV-5) was investigated at atmospheric conditions by Fritsche [27] at different inlet combustion chamber temperatures, different mass flow rates and varied combustor lengths. In all cases, he identified two different flame regimes where a transition of the flame structure occurred. The test conditions are detailed in table 2.1. While the NO_x

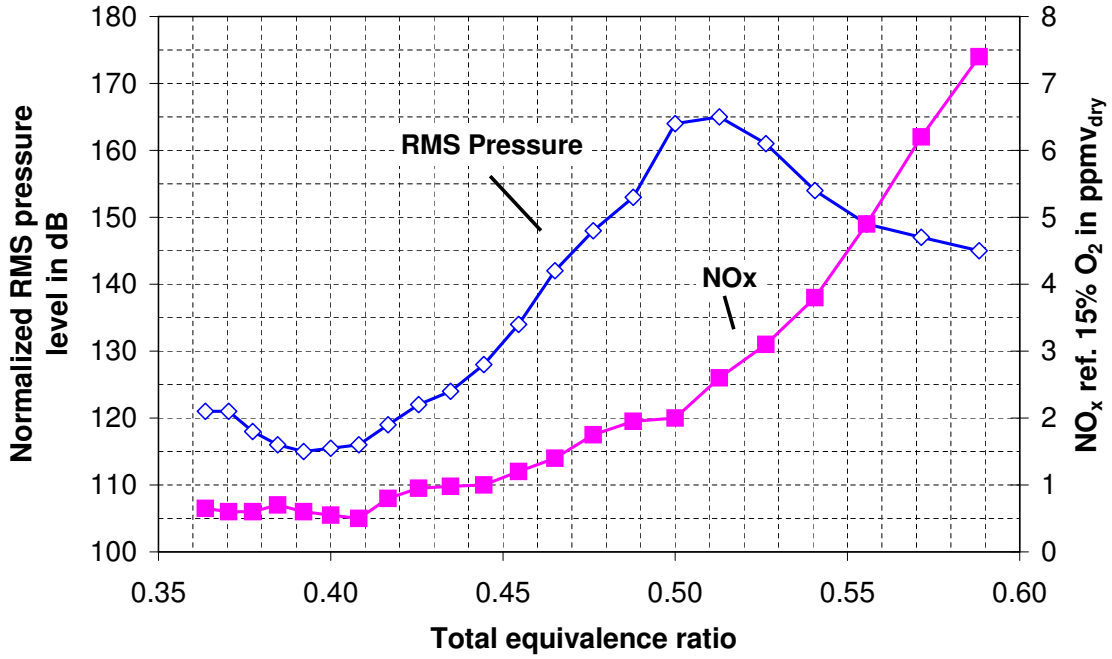

Figure 2.2: NO_x formation and pulsation behavior of the EV-5 swirl burner geometry for different operating points [27].

emissions continuously decrease as the mixture becomes leaner, the pressure amplitudes increase and reach a maximum at $\Phi_{Total} = 0.51$ (Fig. 2.2). At $\Phi_{Total} < 0.51$, the pressure amplitudes start to decrease until lean blow out occurs at $\Phi_{Total} \approx 0.36$. Note, extremely high concentrations of CO and UHC near $\Phi_{Total} = 0.36$ up to around 1700 ppmv were measured and indicates insufficient combustion and probably not the "real" lean blow out of the EV-5 burner. Moreover, Fritsche also mentioned in his study that the flame stabilizes further downstream of the tube and not nearby the swirl burner. Therefore, a more realistic lean limit for this swirl burner type is expected at $\Phi_{Total} = 0.41 - 0.42$ where CO emissions of around 300 ppmv and UHC emissions of around 100 ppmv were measured.
The thermo-acoustic instabilities were also investigated under atmospheric conditions by Lenz [53] with three swirl-stabilized combustors commonly used in Siemens gas turbines. In all tests, he could show reduced pulsations close to the lean blow out limit, independent of the combustor geometry used (Fig. 2.3).

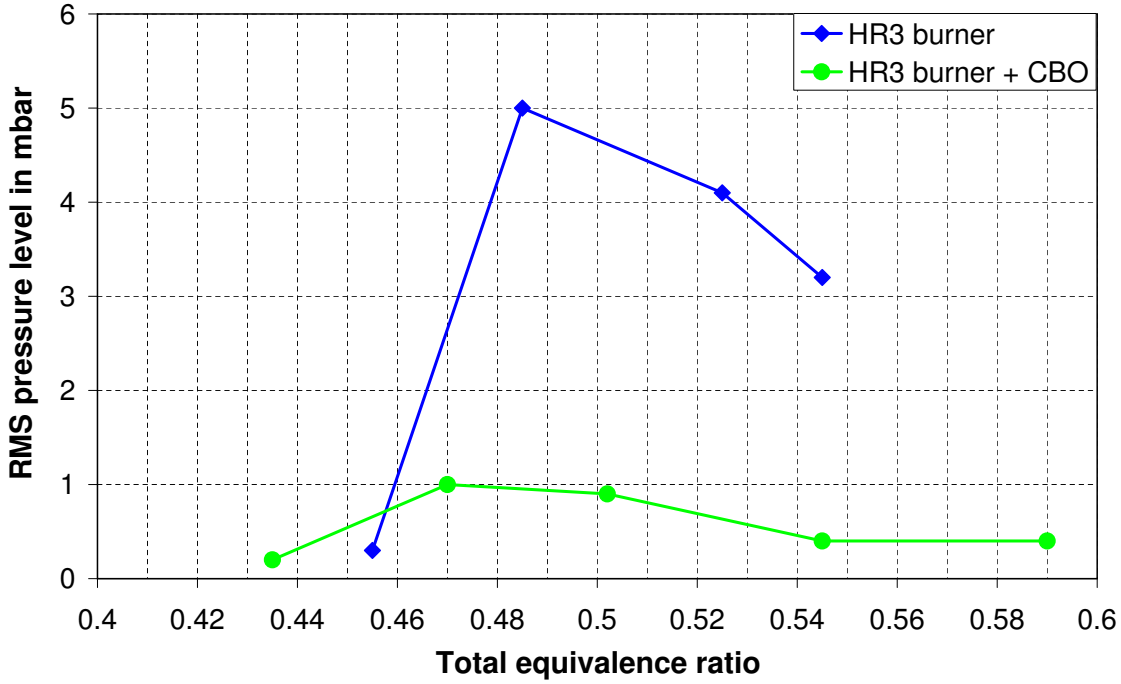

Figure 2.3: RMS pressure levels for different combustor geometries at atmospheric conditions [53].

Kunze [48] conducted atmospheric combustion tests with an annular combustion chamber where two different swirl-stabilized combustors were mounted. In one test case, all combustors mounted in the chamber featured a swirl number that was twice time higher than the SN in the other test case (SN=0.8) . Fig. 2.4 shows the stability map for combustors with the highest swirl number configuration and more realistic for industrial used swirl burners where pulsations seem to be reduced near lean blow out.

Seo [92] investigated thermo-acoustic instabilities with a single swirl-stabilized combustor at different preheat temperatures under pressurized conditions. He showed that the RMS pressure levels decreased significantly close to the lean blow out, independent of the combustion chamber pressure (see Fig. 2.5). He assumed that the heat release fluctuations are not sufficient to excite pressure fluctuations. Furthermore, the dynamic stability close to the lean blow out limit was significantly influenced by the chamber pressure. An increase in chamber pressure led to an increase of the RMS pressure level at the same $\Phi = 0.5-0.52$ near LBO.

A gas turbine model combustor was investigated by Giezendanner [29] under atmospheric conditions and ambient temperatures of 300 K. Further test conditions are mentioned in table 2.1. The stability map shown in Fig. 2.6 was generated at a constant amount of fuel flow rate while the air mass flow rate was varied. The combustion behavior was similar to the other cases and indicated reduced pressure pulsations close to the lean blow out.

In Taupin [99], the pulsation of a swirl-stabilized combustor was investigated at atmospheric and pressurized conditions. For the atmospheric condition case, two stable combustion conditions could be detected extremely close to the lean blow out ($\Phi_{Total} = 0.57$) and at richer mix-

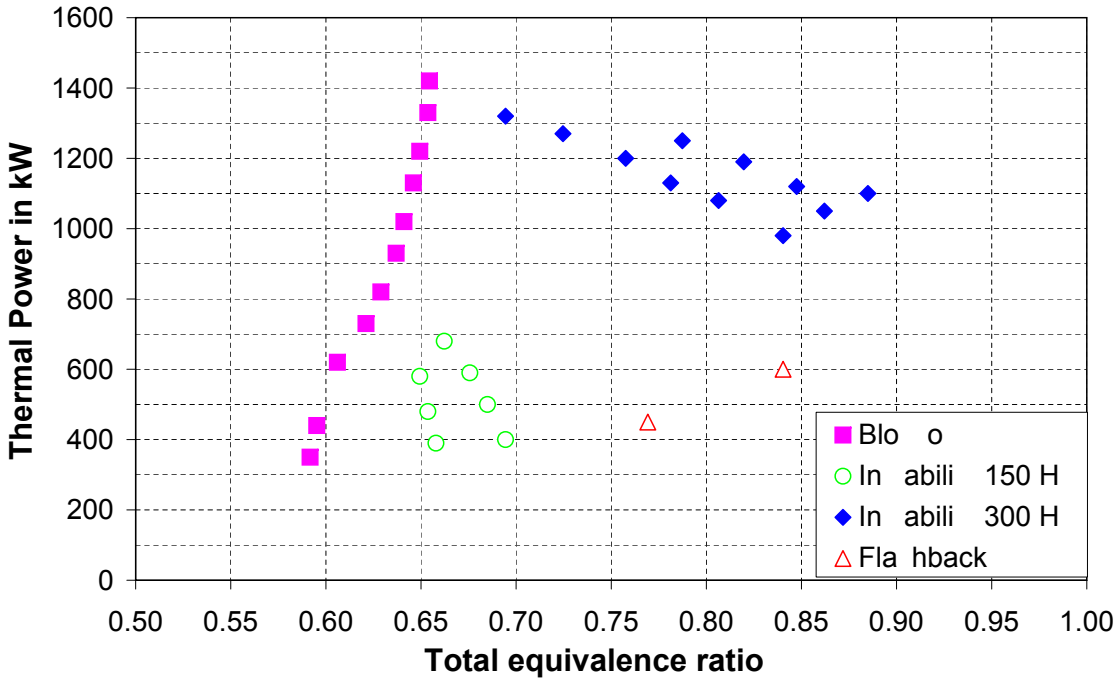

Figure 2.4: Stability map of an investigated swirl burner from Kunze [48].

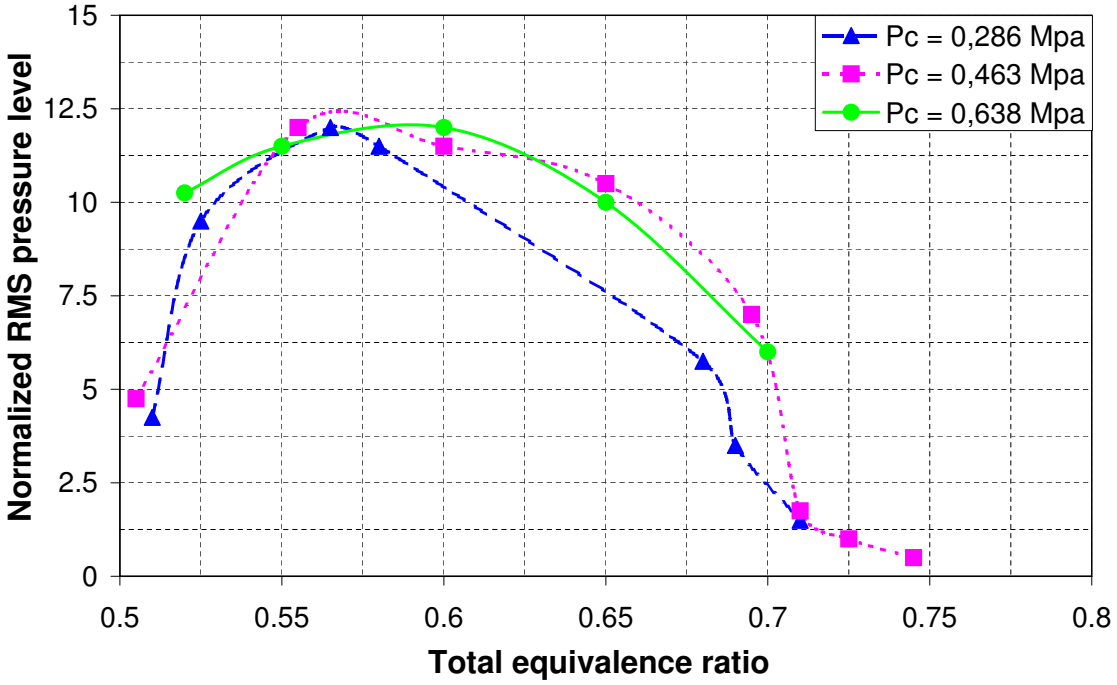

Figure 2.5: RMS pressure level at varied combustion chamber pressures from Seo [92].

ture ($\Phi > 0.7$), stable conditions for the pressurized case could be only found at $\Phi_{Total} > 0.7$. Near the lean blow out limit, acoustic measurements for the pressurized case showed a distinct fundamental at a very low frequency of 16 Hz that does not correspond with the acoustic mode of the combustion chamber. Taupin assumed that this instability was generated by a

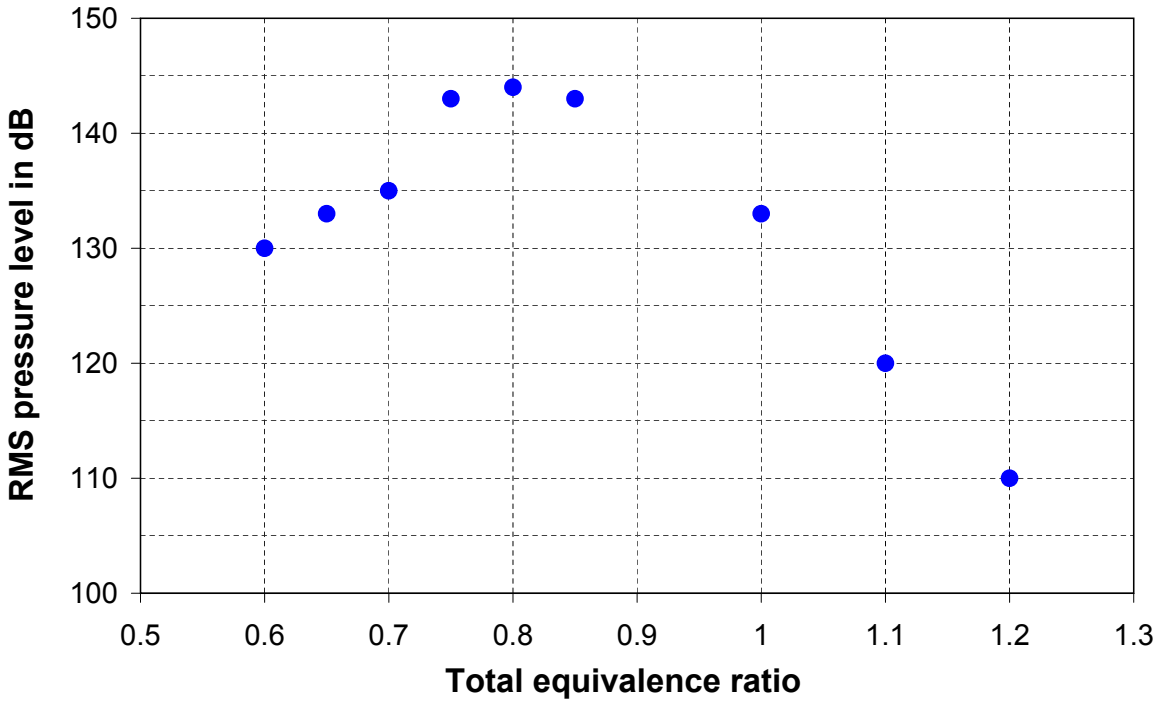

Figure 2.6: Stability map of aero engine model combustor from Giezendanner [29]. Tests were conducted at constant fuel mass flow rate while the air mass flow rate was varied.

coupling of periodic extinction and periodic vortex shedding.

The pulsation behavior of a generic swirl burner typically used in modern industrial gas turbines was closer investigated in [89] under atmospheric conditions. A stability map of the burner is shown in Fig. 2.7 for a preheat temperature of 673 K. The instabilities at richer mixture ($\Phi_{Total} > 0.7$) are traced back to a precessing vortex core (PVC). Temporal flow fluctuations were generated with a frequency of around 252 Hz that are close to the observed fundamental frequency of the unstable mode (262 Hz).

Kendrick [43] investigated the pressure level of a swirl-stabilized combustor for different center-line pilot mass flow rates and different combustion chamber pressures. In Fig. 2.8, the stability map of the baseline configuration without piloting[1] is shown for a chamber pressure of ≈ 15 bar and confirms low pressure amplitudes near the lean blow out limit.

In Lee [52], the amplitude of pressure oscillations is shown for different operating points and indicate a decrease of the amplitude at leaner mixtures. The tests were conducted at atmospheric conditions and 673 K preheat temperature (Fig. 2.9).
Fig. 2.10 presents a schematic stability map of the stationary gas turbine GT26 that featured reduced RMS pressure levels near lean blow out. Pulsation do not always decrease in gas turbines as the stability map for the stationary gas turbine GT13E in Fig. 2.10 proved. The operating conditions for the 78 used burner within this type of gas turbine are very specific. 54 of these burners are operated in richer mode when compared to the rest of the burners. It is not mentioned in the work whether an increase of RMS pressure level can be expected for

[1] the main flame is stabilized by the central recirculation zone

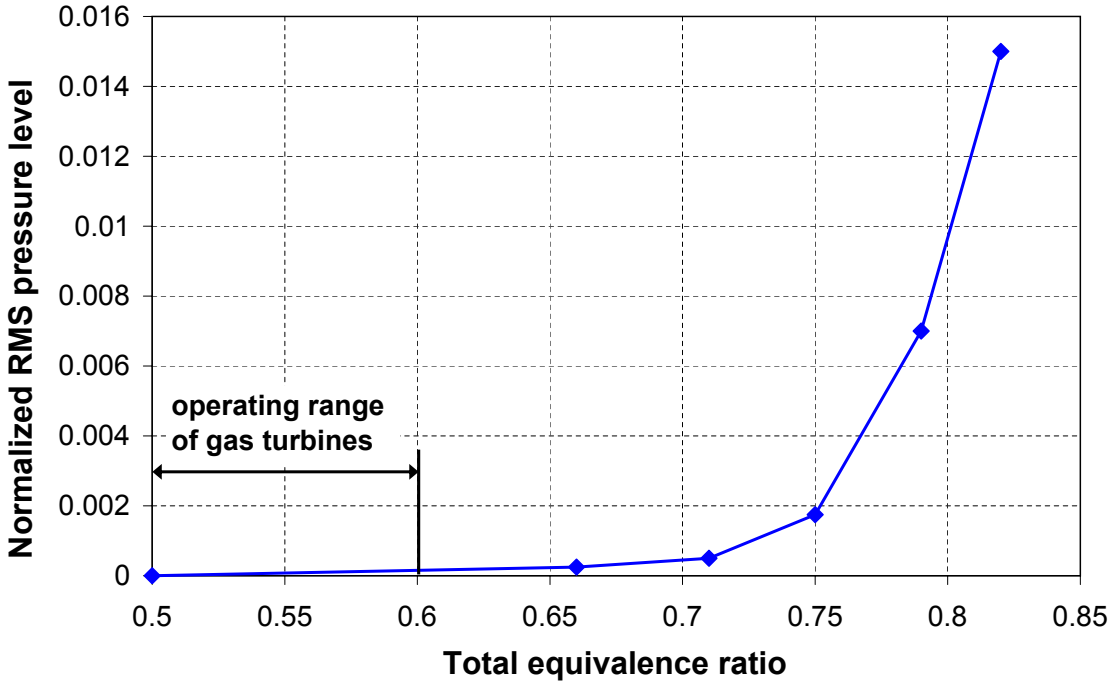

Figure 2.7: Pressure amplitudes of the combustion oscillations as a function of the equivalence ratio from Schildmacher [89].

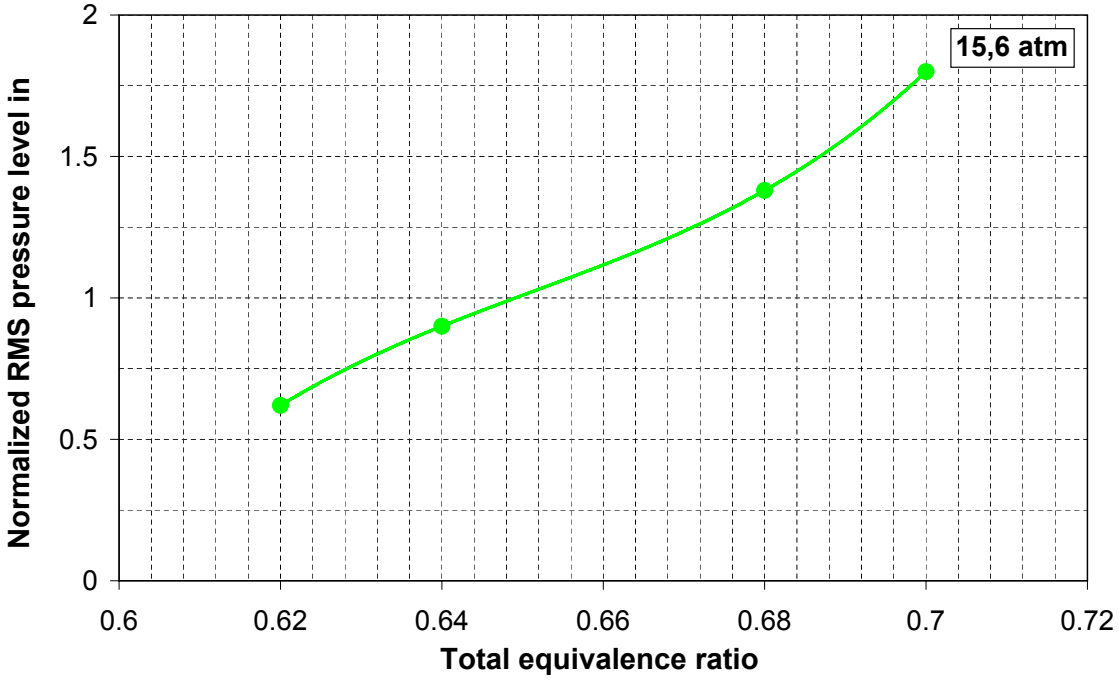

Figure 2.8: Acoustic performance of a swirl-stabilized combustor from Kendrick [43].

the case when all burner are run with the same fuel/air ratio.

In Nair [66], an increase in pressure pulsation was observed with decreasing Φ_{Total} as seen in

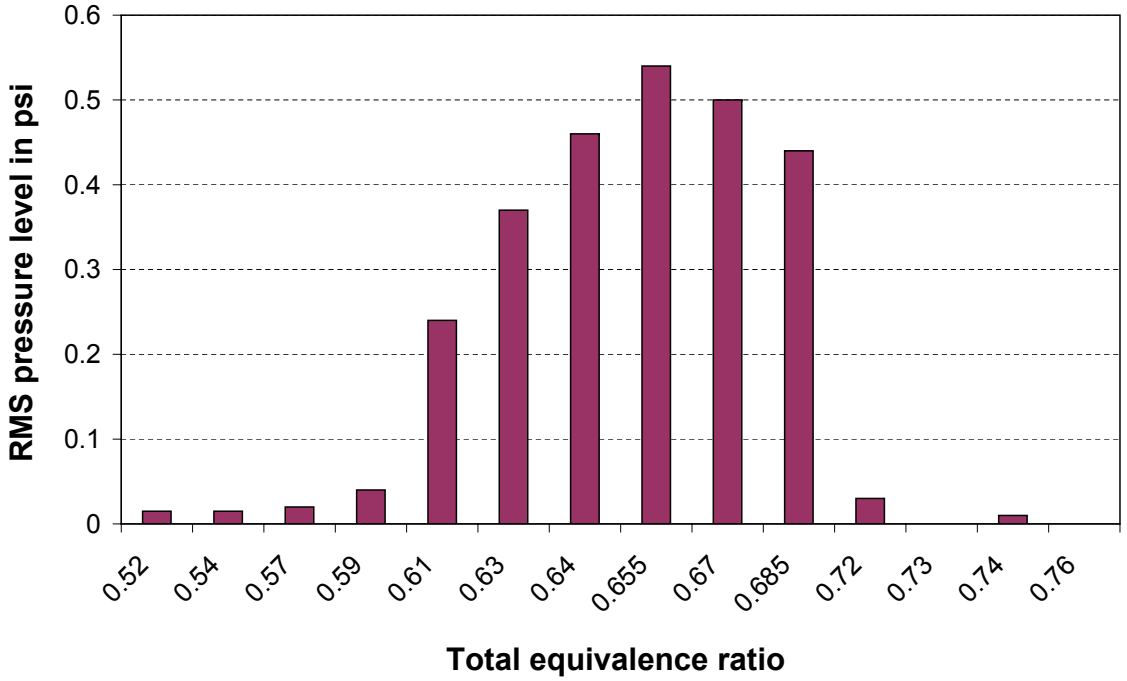

Figure 2.9: Stability map of a swirl-stabilized combustor used in Lee [52].

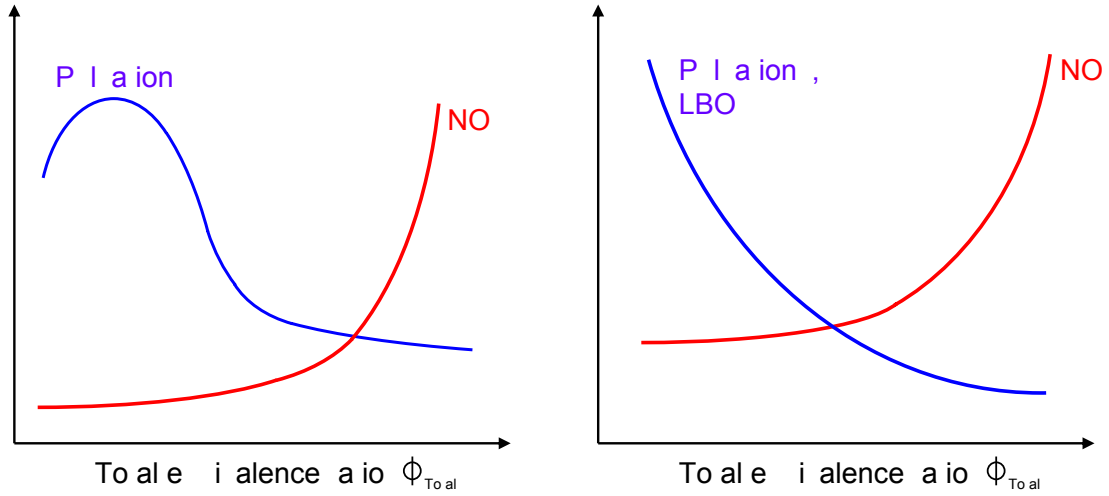

Figure 2.10: Typical pulsation behavior of the gas turbine GT26 (left) and GT13E (right) from Kocanovic [44].

Fig. 2.11. A swirl burner was tested under atmospheric conditions and at ambient temperatures (300 K). It should be noted that the swirl number of the burner is two times lower than the one of industrial combustor. It can be concluded that reduced pulsation behavior does not occur only in single burner test rigs ([89, 43, 27, 52, 93, 29, 92]) but also in real gas turbines e.g. GT26 from Alstom with nearly 1 GW thermal power output ([44]) or in generic annular combustion chambers ([56, 48, 53, 35]). A summary is given in table 2.1 where the tested combustor designs are listed in order of the thermal power output. The pulsation levels

Table 2.1: Overview of tested swirl burners with **LOW** pulsation near lean blow out.

Company	Thermal Power	Pressure	Temperature	Swirl Burner Type			Test facility	References
−−	kW	10^5 Pa	K	Type	Size	used in	−−	−−
Alstom	262000	30	800	EV17	Full Size	GT26	annular combustion chamber	[44]
Siemens	12000	1	650	unidentified	Full Size	unidentified	annular combustion chamber	[56]
Siemens	4500	1	715	Hybrid burner	Full Size	V84.3A	1/8 annular combustion chamber	[53, 35]
Siemens	1200	1	300	Generic	unidentified	(V94.3A)	annular combustion chamber	[48, 45]
Siemens	730	≈ 20	673	Generic	Full Size	unidentified	Single burner	[89]
P & W	unidentified	16	650	unidentified	(Full Size)	FT8	Single burner	[43]
Alstom	70	1	650	Generic	EV5	−−	Single burner	[27]
unidentified	10	1	300	Generic	unidentified	(Aircraft engine)	Single burner	[29]
unidentified	unidentified	6	670	Generic	unidentified	unidentified	Single burner	[92]
unidentified	unidentified	1	673	Generic	unidentified	unidentified	Single burner	[52]
unidentified	unidentified	1	unidentified	Generic	unidentified	unidentified	Single burner	[93]

Table 2.2: Overview of tested swirl burners with **HIGH** pulsation near lean blow out.

Company	Thermal Power	Pressure	Temperature	Swirl Burner Type			Test facility	References
−−	kW	10^5 Pa	K	Type	Size	used in	−−	−−
Alstom	160000	≈ 20	700	EV17	full size	GT13	Silo combustion chamber	[44]
Siemens	1200	1	300	Generic	unidentified	(V94.3A)	annular combustion chamber (SN=0.4)	[48]
unidentified	100	1	300	Generic	unidentified	unidentified	Single burner(SN=0.39)	[66]

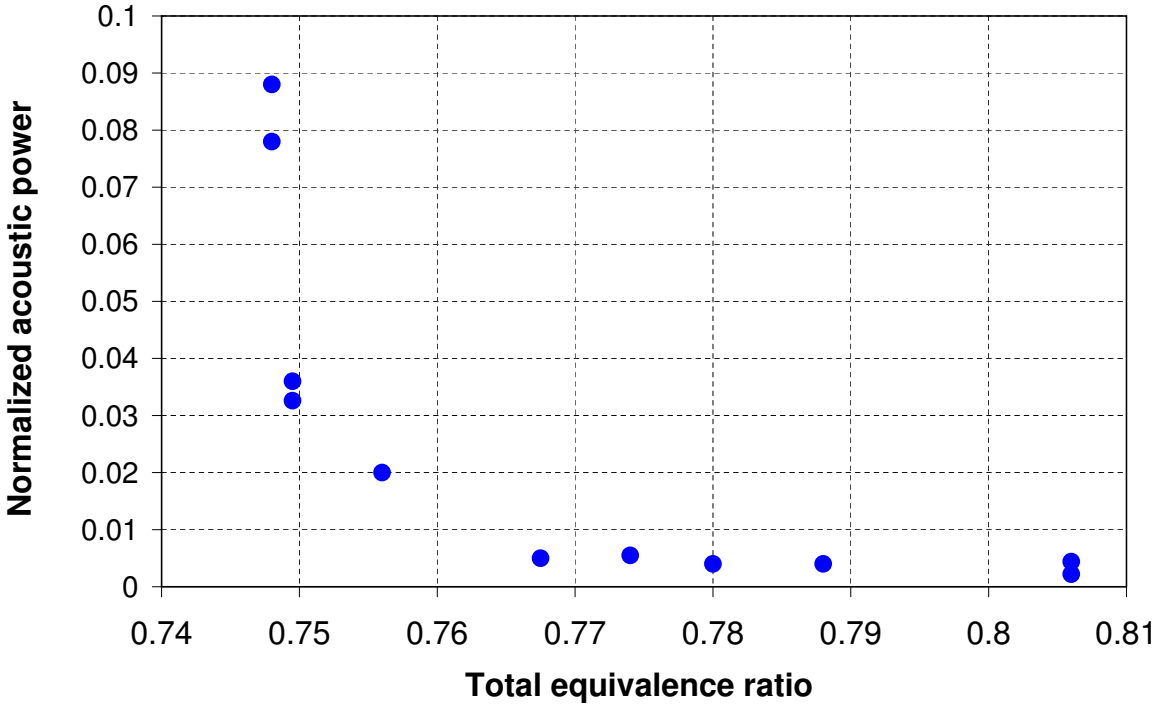

Figure 2.11: Variation in normalized acoustic power in the swirl burner in the 10-200 Hz frequency band for various equivalence ratios near blow out at a combustor exit velocity of 6.6 m/sec (see [66]).

did not decrease at leaner mixture under all combustion conditions as the stability maps of combustors investigated in [44, 48, 66] have shown. Technical details of the combustor design and test setup are listed in table 2.2. To understand why the pulsation behavior differs significantly to the cases presented in table 2.1, the test conditions for each combustor design is now discussed in detail.

Kokanovic [44] shows in his work a schematic stability map of the gas turbine Alstom GT13E that features a silo combustion chamber with EV17 swirl burners. The main part of the swirl burners were operated in rich mode while a quarter of them were operated at mixtures under the flammability limit to reduce the NO_x emissions. The cause for an increase of the pulsation level at leaner mixtures can be most likely traced back to the chosen operating points for the swirl burners that could excite pressure pulsations. Note, the flame front at rich mixture is very compact and the local heat release rate in the range of the critical time delay for p' excitation might be higher while extremely lean conditions increase the danger of local extinction.

Swirl burners used in [48] and in [66] do not represents industrial standards as the swirl number are factor two smaller when compared to e.g. ABB and Siemens burners. The typical swirl number for industrial applications is in the range of 0.7-0.9 (see [49]). Lieuwen [57] conducted tests with the same combustor described in [66] and noted that the sensitivity of the reaction rate increases to leaner mixture. Thus, the heat release rate fluctuations generated by small perturbations can easily excite pressure fluctuations.

2.2 Causes for low pulsation

The investigated swirl burners listed in table 2.1 indicated decreased amplitudes of pressure oscillations near the lean limit. This oscillation behavior might be caused by two main mechanisms:

1. The overall time delay between injection and ignition of the mixture changes with decreasing Φ_{Total} (spreading of the flame front in axial direction) so that either the phase-shift between heat release fluctuation and pressure oscillations becomes greater than 90° and/or the frequency of the heat release fluctuations is shifted out of the range of the acoustic modes of the systems.

2. The premixed flame close to the lean blow out is mostly spread within the combustion chamber in axial direction so that the local heat release rate per volume is much lower when compared to richer operating points. Thus reduces the feeding energy for p' excitations and would explain the reduced pressure level.

The last mechanism is very attractive for gas turbine application as it might reduce the pressure oscillations even though its frequency would match with the acoustic mode of the system.

Fritsche [27] summarized that the transition of the flame structure between region 5 and region 3 shown in Figure 2.1 takes place within a Φ-band and is characterized by an axially oscillating flame front in region 4 while the transition between the flame structures in region 2 and 3 occurred nearly instantly (Fig. 2.1). The transition at richer mixture (region 4) is referred to as "slow transition" and the one at leaner mixtures as "fast transition". The cause of the "slow transition" might be traced back on the coupling of the heat release fluctuations Q' and pressure fluctuations p' and is defined by the extended Rayleigh criterion (equation 2.1, [17]).

$$\frac{1}{T}\int_{t_0}^{t_0+T}\int_V \frac{\gamma-1}{\bar{\rho}\bar{a}^2} p'Q' dV dt > \frac{1}{T}\int_{t_0}^{t_0+T}\oint_S p'\mathbf{u}'\cdot\mathbf{n} dS dt \tag{2.1}$$

with

T	period of harmonic oscillation ($T=\frac{1}{f}$),
$p'(t)$	Pressure fluctuation,
$Q'(t)$	Heat release fluctuation,
S	Surface,
$\mathbf{n}$	Normal vector,
$\mathbf{u}$	Vector of Velocities,
γ	ratio of specific heats,
V	Volume,
ρ	density,
a	speed of sound.

Moreover, the acoustic energy feeding by Q' expressed by the left term in equation 2.1 has to exceed the dissipation losses expressed by the right term in equation 2.1 before p' can be further excited. Several excitation mechanisms could be identified in former works (e.g. [50, 74, 58]) whereas the "Richards-Lieuwen" mechanism seems to be the most important (see [87]). Q'

is generated by fuel-air ratio fluctuations and can induce p' if the convective time delay between the fuel injection and the ignition of the mixture is located in the range of one of the acoustic modes of the systems (see [60, 57]). It is interesting to note that a broad-band time delay generated by a well distributed premixed flame within the combustion chamber appears to be linked with reduced pressure oscillations as it can be assumed to be in regions $1-3$, Fig. 2.1. The assumption seems to be confirmed by former works (table 2.1) and by experimental results in this study. Another explanation might be a reduced local heat release rate in the range of the critical time delay for p' excitation (section 6.3.4) that is not sufficient to overcome the dissipation losses.

Similar conclusions can be drawn from investigations with flameless combustion where the heat release takes place within the substantial part of the combustion chamber. Such flames show a broad-band time delay and low heat release rates at every location so that further p' excitations becomes very difficult due to dissipation losses [18]. This is also why fluid dynamic instabilities e.g. vortex shedding have less impact on p' excitation under these conditions when compared to compact premixed flames. Wuenning [102] mentioned that the high stability of flameless combustion can be also traced back to the random flame initiation at many locations simultaneously and not only at a single point e.g. the stagnation point. For this reason, region 3, with low p' and (still) efficient combustion is attractive for gas turbine operation as flame temperatures that are responsible for NO_x formation can be kept low ([15]). A control method is required that is able to prevent local extinctions at the "lean mixture (LM)" boundary of region 3 and is able to suppress/delay the increase of pressure pulsation at the "rich mixture (RM)" boundary. State of the art control methods for local extinction prevention and instability suppression will be discussed in section 2.3.

2.3 Concept for instability suppression and LBO extension

Failsafe and passive control concepts for lean premixed combustion are highly desirable in gas turbines, especially for aircraft applications as one hand side they do not consist on moving parts in general and other hand side they are applied at combustion conditions where the danger of thermo-acoustic instabilities and emissions are already reduced. For premixed combustion, such conditions can be found in region 3 and 5 as shown in Fig. 2.1.
Most combustors for aircraft gas turbines are operated in region 5 between $\Phi_{Total} = 1.2-1.4$ to reduce the danger of pulsations and high NO_x formation. But, $\Phi_{Total} > 1$ leads to incomplete combustion and thus would reduce the combustion efficiency as the injected fuel can not be fully burnt due to the lack of oxygen. To overcome this problem, different concepts are used by aircraft gas turbine manufacturers. Rolls-Royce engines are equipped with pilot and main combustors that are designed for different operating conditions. While the pilot combustors are used alone at take-off, the main combustors with leaner primary zone is supported only with a small pilot combustor flame at cruise where low NO_x emissions are required. Pratt & Whitney engines[2] keep the NO_x emissions low by reducing the residence time of reaction products in hot zones. Thereby, the reaction products and unburned hydrocarbons (UHC) are mixed with cooling air downstream of the primary zone to reduce the averaged flame temperature and Φ_{Total}, quickly. NO_x formation can be extensively suppressed with this concept that is referred as RQL-concept (**R**ich-burn, quick-**Q**uench, **L**ean-burn) while the danger of soot generation increases, especially at take-off, where a significant amount of soot

[2] PW4000 and PW6000

could be generated if the residence time for hot products within the primary zone is too short.

Region 3 represents another operating range where much lower NO_x emissions could be achieved when compared to current concepts in aircraft engines. So far, none of the gas turbine manufacturers have proposed this region for gas turbine operation. The reason might be found in the narrow Φ-band where the lean premixed combustion can be operated without efficiency losses (local extinction, region 1 and 2) and high pulsation level (instabilities, region 4). To extend region 3, a suitable control method is required that is able to control both the local extinction and the pressure pulsation. In the past, the pilot diffusion[3] appeared to fulfill the requirements as it provides the main combustion with additional radicals so that the range of efficient combustion can be significantly extended (see section 6.2). The pilot fuel injection can be modulated by special valves in order to reduce the NO_x emissions and to suppress significantly thermo-acoustic instabilities (see [82, 71, 3, 72]). But, the combustion within the diffusion pilot flame front runs at stoichiometric conditions $\Phi = 1$ where nearly the highest NO_x emission rate (per unit time) is achieved [15][4]. Moreover, fuel modulation is mostly realized by mechanical moving parts that can wear and fail. Therefore, an alternative control method is required that prevents local extinction and instabilities, like the diffusion pilot but without an increase in NO_x emissions and without mechanical valves. Premixed pilot[5] seems to fulfill the requirements. Kendrick [43] showed in his study that the premixed pilot flame is able to suppress thermo-acoustic instabilities in a swirl-stabilized combustor. The tests were conducted at pressurized conditions up to 15 bar. Premixed pilot flames are able to sustain the main combustion shortly before local extinction occurs if the pilot flame can be sufficiently stabilized and controlled e.g. by a spark or a laser beam. Therefore, a device is required that is able to mixture the fuel and air before ignition, prevent flash backs and can be easily mounted into current combustion chambers. In the following section, the main components for premixed pilot flame generation will be explained in detail.

Main components for premixed pilot flame generation

The main components for premixed pilot flame generation are the ignition source and the device where the pilot combustion takes place (pulsation tube).

Ignition sources

Ignition sources for a fuel/air mixture could be a conventional spark plug or a laser ignition device. A wire heated up by a high current represents another option but is not further mentioned in the following as the consumed energy is much higher when compared to the other methods. The use of conventional spark plugs is limited on gas turbines with low maintenance rate as the durability of a spark plug strongly depends on the pressure, temperature, and the rate of sparks per minute. In gas turbines with high pressure and temperature levels, the spark plug service life is dramatically reduced for continuous operation and for high frequencies. The reason for the lower durability at extreme conditions (e.g. 40 bar and $900 - 1200$ K) can be explained by the increased minimum breakdown voltage with increased pressure that directly leads to an accelerated aging of the ignition electrode ([46]). The typical life span of standard spark plugs used in natural gas engines and at an extremely low spark

[3] meaning pilot fuel injection and/or diffusion flame generation within the combustion chamber

[4] The maximum formation of NO_x emissions is achieved at $\Phi_{Total} \approx 0.8$ for H_2, methane CH_4 and propane C_3H_5.

[5] meaning injection - and/or ignition of a premixed pilot mixture into the combustion chamber

rate of 5 Hz and 40 bar, 900 K is estimated to be 8000 hours[6]. Special compositions and a better arrangement of the electrodes promise reduced erosion and increased service life so that typical maintenance rates for stationary gas turbines of approx. 10000 hours ([51]) could be achieved. With the development of high durable laser ignition devices, the service life can be dramatically increased so that pilot premixed flames become very attractive for controlling the main combustion. The improved durability of laser spark plugs can be explained by different location of flame ignition and laser beam generation (see Fig. 2.12). When the sensitive laser

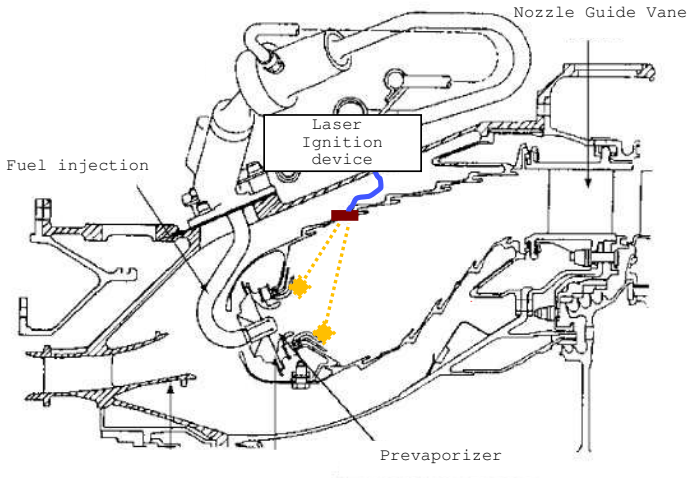

Figure 2.12: Gas turbine equipped with laser ignition device for premixed pilot mixtures ignition.

system could be mounted outside of the combustion chamber, the laser beams are led through a quartz glass or cooling borehole into the high pressurized combustion chamber (Fig. 2.12). The principle of the laser ignition device can be described by a coherent emission from the high power pulsed laser that is focused on a tiny volume inside of the combustion chamber (away from the wall) so that the fuel/air mixture is ionized by the existing high electric field gradient at that position. The ignition takes place if the energy is high enough to exceed the dielectric strength of the mixture. Currently, several patents ([32, 85]) exist for different laser ignition devices. In [32], a laser based ignition system consisted of a high power pulsed laser and a coupling for a plurality of laser plugs. This device is thought to ignite a natural gas/air mixture in stationary gas engines at pressures up to 200 Bar. Preliminary investigations in [64] have shown that atomized kerosine can be also ignited by laser-ignition. Even though the tests were conducted under atmospheric conditions, it seems to be likely that the laser-ignition should work at pressurized conditions by increasing the laser energy. So far, the commercial use of laser ignition devices is prevented by its size, costs and its weight.

Pulsation tube

Concepts for a pulsation tube for premixed pilot mixture are given by many patents written between 1900 and 1950. Most of them were mainly thought as a propulsion system for air vehicles. The thrust was generated by a pulsed detonation within the combustion chambers that were either valve-less [30, 31, 80] or equipped with flaps [90, 24, 41, 7, 62]. The solutions without flaps are especially attractive for the use in gas turbines even though the pulsed

[6]Robert Bosch GmbH; Automotive Aftermarket, Spark Plug & Filters (AA-SF ENS1)

detonation cannot be used to sustain the premixed combustion extremely close to the lean blow out. The detonation wave ($\approx$ 2000 m/s) might extinguish the main flame. However, the detonation of a fuel/air mixture can be suppressed if the diameter of the combustion chamber is chosen smaller than the characteristic cell sizes within the detonation wave, so that only a low velocity deflagration wave can propagate. A typical cell size for a methane-air mixture [40] is 300 mm at atmospheric pressure, the detonation of a kerosine-oxygen mixture [84] requires a tube diameter of approx. 70 mm under ambient conditions. Moreover, the detonation mechanisms (detonation transition and deflagration-to-detonation transition) are influenced mainly by the N_2 concentration within the air, inlet temperature, pressure, droplet size of the liquid fuel and fuel vaporized molar fraction. While an increase in pressure and temperature improve the detonation ability of the mixture, larger droplet size and increased concentration of N_2 reduce this ability in general.

Reynst [81] presented a pulsed combustion chamber without flaps and without a periodically operated spark plug, which is the best design choice with respect to high durability. The frequency of the self-oscillating combustion was fixed by the combustion chamber outlet diameter and inlet pressure level, so that the design is not useful in respect to flame instability control as the frequency and the phase shift have to be adapted very quickly.

In [101], an actuator with no mechanical valves or flaps is described that produces periodically generated flame kernels and is able to suppress instabilities at 100 Hz by 5 dB for closed-loop operation under 2 Bar conditions. The periodic ignition of the stoichiometric mixture of fuel and air is realized in the described actuator by a spark plug whose frequency could be varied from 50 Hz to over 1 kHz.

2.4 Conclusion

Previous studies have shown that the pulsation level of different swirl-stabilized combustors commonly used in gas turbines decreases to the lean limit, independent of the combustion chamber pressure and inlet temperature. Thus, narrow operating range near LBO exists under certain conditions where NO_x and pressure pulsation level are low. To extend this range, different control methods are proposed and evaluated under atmospheric conditions in section 6. The investigations were conducted at atmospheric conditions, but the results can be extrapolated to pressurized conditions as the mechanism responsible for low pressure pulsation near LBO is independent of the boundary conditions. Moreover, the NO_x formation near the lean blow out is only slightly dependent on pressure as previous studies in [19, 55, 54, 67, 96] have shown. The mechanism for local extinction prevention (see section 6.2) bases on a sufficient radical pool at the lower stagnation point of the central recirculation zone is also independent of the boundary conditions. Premixed pilot injection and flames appear to extend the operating range near LBO efficiently without an increase in NO_x ([2]). To control the premixed pilot flame directly, a pulsation tube similar to the one described in [101] has been proposed in this study and is described in section 5.1.

Chapter 3

Versatile atmospheric single burner test rig

A versatile atmospheric single burner test rig is required to investigate closer the emission and the pulsation behavior of a swirl-stabilized burner with and without applied control strategy described in section 1.2. Several parts of the single burner test rig could be provided by the EPFL-Lausanne (Switzerland) and are shown in Fig. 3.1. The test rig was mounted vertically

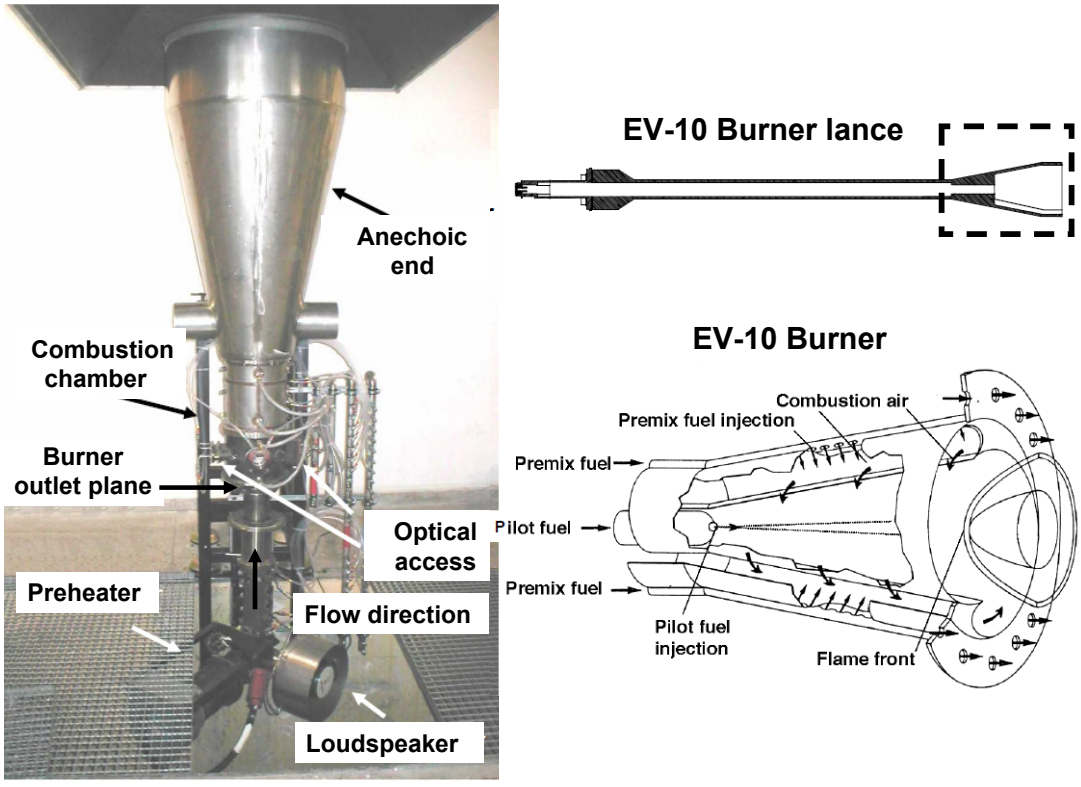

Figure 3.1: Main parts of the atmosheric single burner test rig.

at the combustion laboratory at the Hermann-Föttinger-Institut. Due to the limited height between the laboratory floor and the chimney, the air pre-heater and the loudspeaker were located inside a maintainance channel while the other parts (the burner lance, the combustion chamber and the anechoic end) could be placed above it. For the tests described in this thesis,

some modification were done to the burner test rig (compare Fig. 5.1 and Fig. 3.1). The anechoic end was replaced by a 1.3 m tube to achieve a more unstable combustion system. Also, the original combustion chamber, lined with ceramic was replaced by a quarzglass tube to improve the access with ICCD camera and photomultiplier cable. Theoretically, the test rig is designed for swirl-stabilized burners up to 150 mm outlet diameter (e.g. EV-15 burner from ABB/Alstom) and corresponds with nearly $1-1.2$ MW thermal power. For this thesis, a smaller burner with nearly 100 mm outlet diameter (EV-10 burner from Alstom) was chosen that has an approximately cross sectional expansion ratio of 4 and a thermal power range between 50 kW and 450 kW. Currently (2010), higher thermal power than 240 kW can not be provided under stationary conditions due to the limited air mass flow (see section 3.2, air supply) and the limited flow temperature through the exhaust duct and through the exhauster (see section 3.3). The burner exit was located at the entrance of the quarzglass combustion chamber, referred as burner outlet plane in Fig. 3.1. Just above that position, the burner flame can be stabilized by the strong vortex of the fuel/air mixture (see section 3.1). A continuous and safe operation of the burner can be guaranteed by the installed control and safety system described in section 3.2, closed loop control and safety measures. In the following sections, the swirl-stabilized burner is described in detail as well as the required supply lines, auxiliary units and safety measures to guarantee a stationary operation of the swirl-stabilized flame within the combustion chamber.

3.1 Swirl-stabilized EV-burner

The EV-burner (EV-environmental) consists of displaced half cones with two slots between them, such that air is forced to enter into the cone circumferentially [42]. In Fig. 3.1 is shown an EV-10 burner with an outlet outer diameter of nearly 100 mm that was used in this study. There is also EV-5 with 50 mm, EV-15 with 150 mm and EV-17 with 170 mm outlet diameter. At each of burner slots, main fuel can be injected through 62 boreholes, 0.7 mm diameter, that are distributed equidistantly between the apex and the burner exit. Pilot fuel or pilot fuel/air mixture can be injected at the EV-10 apex using a pilot lance. The injected pilot fuel is mainly used at the start-phase of combustion and for further control during the main combustion. Note the pilot lance equipment was slightly modified for the tests described in this study (see section 5.1). The special design of the EV-burner guarantees flame stabilization at the burner exit. To understand the physical background of the flame stabilization, the mechanism will be explained in more details in the following section.

Flame stabilization

In general, a flame can be sustained respectively stabilized at a location within the combustion chamber where new reaction partners (fuel/air mixture) are able to exceed the ignition temperature. To ensure a sufficient temperature increase of the reaction partners, the residence time within the hot temperature region is normally increased by reduced flow velocities. This can be realized by different flameholder concepts: the bluff-body flameholder e.g. a flate plate and the aerodynamic flameholder that is applied in swirl-stabilized burner used in this study (see Fig. 3.2). Both concepts guarantee flame stabilization by a recirculation of hot gases and entrained fresh combustable mixture, once the mixture ecxeeded the ignition temperature. While the recirculation zone of the bluff body is generated by the wake, the aerodynamic flameholder is generated by a swirling flow and will be explained in more detail below. For bluff-body flameholders, many pioneer studies in the 1950's, e.g. [61, 104, 94], were carried out

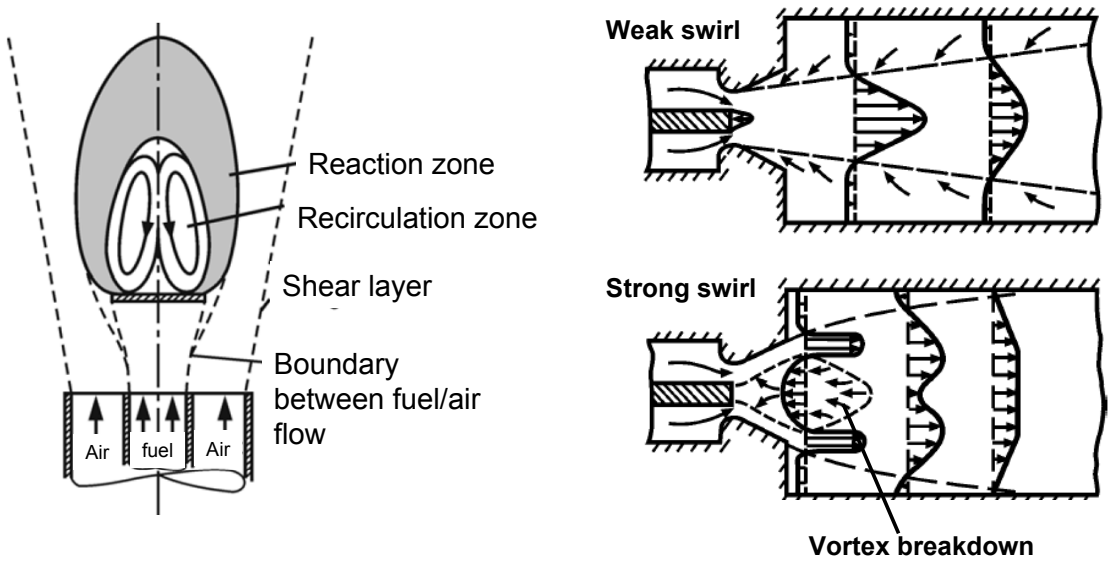

Figure 3.2: Difference between bluff-body flameholder (left) and aerodynamic flame holder (right). Note, a recirculation zone (vortex breakdown) can be generated in case of the aerodynamic flameholder concept only when a sufficient strong swirling flow exist.

to get a better understanding of the flame stabilization process. Later in the 1980's, the studies focused more on bluff body optimization [77, 83, 11] to better predict the stability limits in terms of the flow conditions (pressure, temperature, velocity, turbulence level), equivalence ratios and the bluff-body dimensions. Today, the bluff-body is often used for flame stabilization in ramjet and turbojet afterburner systems. In commercial gas turbines, this kind of flame stabilization is not often used as the reaction takes place extremely close to the wall so that addional cooling or special materials are required to resist the flame temperatures. The aerodynamic flameholder doesn't show this disadvantage and represents the prefered solution in today's gas turbines.

The aerodynamic flameholder effect can be realized in a radial swirler, as shown in Fig. 3.1 where the flow is forced in circumferential direction and generate a pressure gradient in radial direction due to centrifugal forces. The generated circumferential velocity at each radii is similar to a so-called Hamel-Oseen vortex that describes the behaviour of a solid vortex at lower radii and a potential vortex at higher radii. Therefore, the lowest pressure can be expected within the centre according to equation 3.1, where the circumferential velocity can be assumed to be zero.

$$\frac{w^2}{r} = \frac{1}{\rho}\frac{\partial p}{\partial r} \tag{3.1}$$

Further downstream, the axial velocity of the flow at the centreline will further decreases due to the divergent channel of the burner (see bernoulli equation 3.2 valid for swirling flows). Note, the divergent channel of the burner (cross-section area expansion of 4 or more) is primarily chosen to prevent an increase of the axial velocity by the volume expansion in the reaction zone by a factor of 6. This measure stabilizes further the vortex breakdown in reacting flows

[39].

$$p = p_0 + \frac{\rho}{2} \cdot w^2 \tag{3.2}$$

If the swirl is strong enough, a recirculation zone or a so-called vortex breakdown can be formed as shown in Fig. 3.2, right sketch. To quantify the strength of the swirl, the parameter swirl number S_N was introduced and represents the ratio of the circumferential (G_ϕ) and the axial momentum (G_x) (see equation 3.3).

$$S_N = \frac{G_\phi}{G_x \cdot R} \tag{3.3}$$

where G_ϕ and G_x can be expressed as follow:

$$G_\phi = \int_0^R (c_u \cdot r) \cdot \rho \cdot c_{ax} \cdot 2 \cdot \pi \cdot r dr \tag{3.4}$$

$$G_x = \int_0^R c_{ax} \cdot \rho \cdot c_{ax} \cdot 2 \cdot \pi \cdot r dr + \int_0^R p \cdot 2 \cdot \pi \cdot r \cdot dr \tag{3.5}$$

Beside the above definition of S_N, there are also slightly different definitions depending on the swirler type, which are mentioned in [16].

Mass flow limits

The mass flow limits of fuel and air mass flow rates are required for the design of the supply line dimensions and can be derived directly from the maximum thermal power output of $\dot{Q}_{burner,max} = 1.2$ MW for the EV-15 burner. Assuming an estimated caloric value of $H_{fuel} = 10$ kWh/m^3 at ambient conditions and a density of $\rho_{f,ambient} = 0.73$ kg/m^3, the appropriate fuel mass flow rate can be derived from equation 3.6.

$$\dot{m}_{f,max} = \dot{Q}_{burner,max} \cdot \frac{\rho_{f,ambient} \cdot t}{H_{fuel}} = 87.6 kg/h \tag{3.6}$$

Based on the maximum fuel mass flow rate for the EV-15, the maximum air mass flow rate under lean conditions at an equivalence ratio of $\Phi_{lean} = 0.4$ and for stoichiometric fuel air ratio $FAR_{stoic} = 0.0585$ can be calculated by equation 3.7.

$$\dot{m}_{air,max} = \dot{m}_{f,max} \frac{1}{\cdot FAR_{stoic} \cdot \Phi_{lean}} = 3718 kg/h \tag{3.7}$$

Note, 32.8 kg/h fuel mass flow rate and 1370 kg/h air mass flow rate should be provided for the EV-10 burner to achieve the mentioned heat release of 0.45 MW under the same lean condition. Thereby, the fuel is injected with a rough outflow velocity of $c = 153$ m/s through each of the boreholes (Total cross section area of all 62 boreholes is $A = 6.8 \cdot 10^{-5}$ m^2 and a fuel density $\rho_s = 0.85$ kg/m^3 for methane). Under these outflow conditions, the static temperature of 286 K only slightly differ from assumed total temperature of 292 K as the Mach number is low with $M = 0.35$. Both values can be derived iteratively from equation 3.8.

$$\begin{aligned} a &= \sqrt{\kappa_f \cdot R_f \cdot t_s} \\ M &= \frac{c}{a} = 0.35 \\ t_s &= \frac{T_T}{(1 + (\frac{\kappa_f - 1}{2}) \cdot M^2)} = 286K \end{aligned}$$

with κ_f ratio of specific heat (1.33) $= \frac{c_p}{c_v}$
T_T Total temperature (292 K)
R_f Gas constant (478 $m^2/(s^2 \cdot K)$) for methane

(3.8)

3.2 Components of the single burner test rig facility

The single burner test rig facility consists of several components that guarantee the continuous and controlled operation of the swirl-stabilized combustor. Four different supply lines are indicated in the flow chart shown in Fig. 3.3:

1. water supply for combustion chamber cooling and water-cooled microphone,
2. air supply for the combustion process and for cooling the quartzglass combustion chamber, tubes etc.,
3. natural gas supply for the combustion process,
4. exhaust duct for sucking the exhaust out of the laboratory.

Moreover, safety techniques for the detection of harmful emissions e.g. CO and UHC was installed within the laboratory to switch off the fuel supply in emergency cases. A closed loop control of fuel and air mass flow rate was chosen to keep the set mass flow rate constant even though the boundary conditions (pressure and temperature fluctuation) would change during the tests. All components will be discussed in more detail in the following section (see also [1]).

Water supply specification

The water supply was realized by a closed cycle cooling system as seen in Fig. 3.3. It has some advantages in comparison to an open cooling system:

1. environment-friendly due to low water consumption,
2. low fixed cost in comparison to open cycle as the price for fresh water and foul water is much higher than the electrical cost for the closed cycle system.

To estimate the size of the closed cycle cooling system, the maximum heat transfer from the exhaust to the water has to be estimated, firstly. The heat transfer calculation is made with a water-cooled tube mounted above the quartzglass combustion chamber. The quarzglass features a height of ≈ 0.25 m and a diameter of 250 mm.
It is assumed that a maximum temperature difference of 1000 K exists between the exhaust and the wall temperature. Furthermore, the exhaust temperature is assumed to be 1800 K, much higher than the allowed temperature of 1600 K and the wall temperature should be remain at 800 K. To calculate the needed water volume flow, an overall heat release rate $\dot{Q}_{Total}$ by radiation and convection was estimated by

$$\dot{Q}_{Total} = \dot{Q}_{radiation} + \dot{Q}_{convection} \tag{3.9}$$

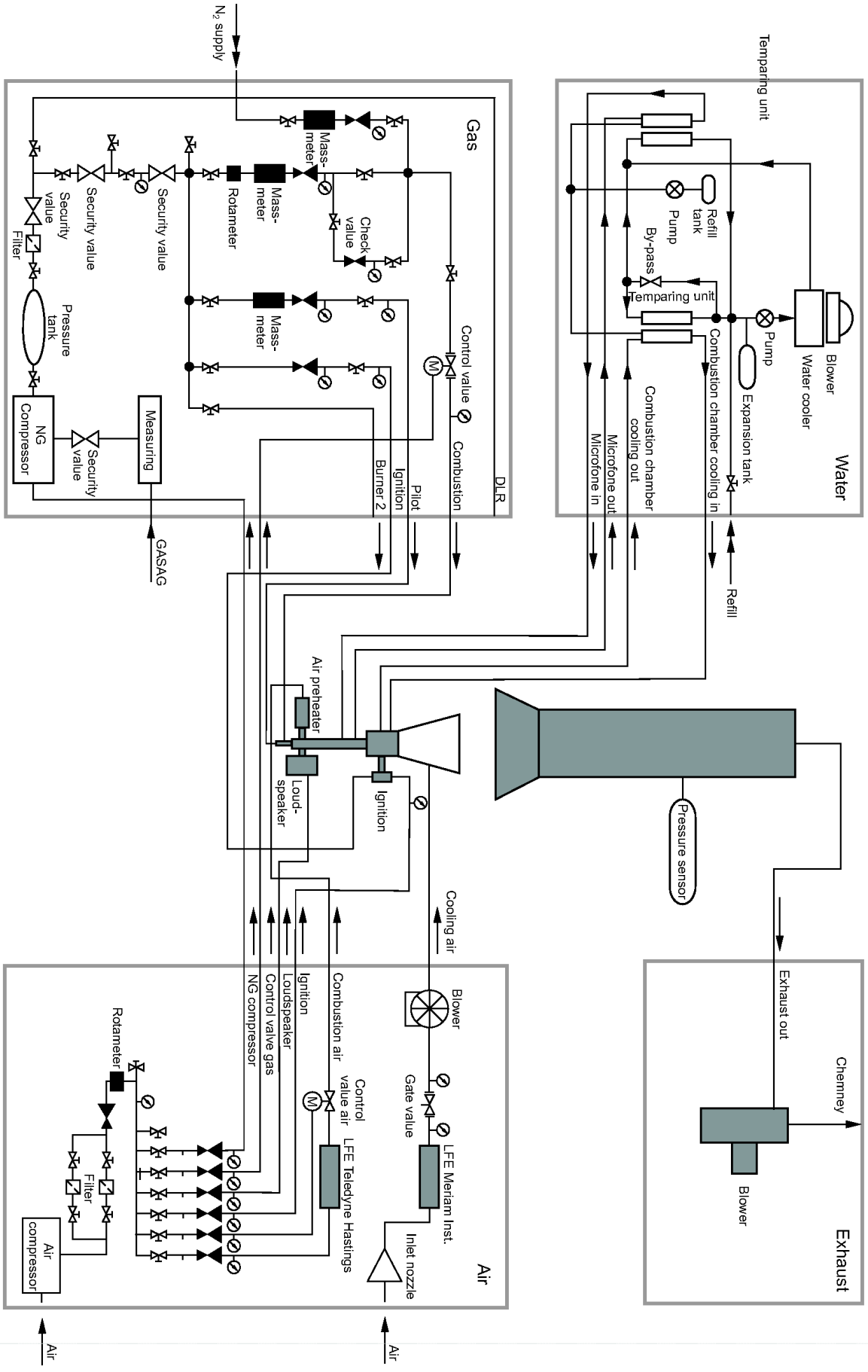

Figure 3.3: Flow chart of the single burner test rig facility.

with

$$\dot{Q}_{radiation} = A \cdot \epsilon \cdot \sigma_s \cdot (T_{Gas}^4 - T_{Wall}^4); \quad \dot{Q}_{convection} = A \cdot \alpha \cdot (T_{Gas} - T_{Wall}) \tag{3.10}$$

The following values are used in eq. 3.10:

1. The heat transfer area $A = 0.19$ m^2, that can be derived from the geometry of the water-cooled combustion chamber.

2. The emission grad $\epsilon \approx 0.05$ that is typical for combustion of methane/air mixture with low soot formation.

3. Stefan-Boltzmann-constant $\sigma_s = 5.67 \cdot 10^{-8}$ W/(m$^2\cdot$ K^4).

4. The exhaust temperatures T_{Gas} and wall temperature T_{Wall} mentioned further above.

5. The heat transfer coefficient $\alpha \approx 60$ W/(m $\cdot$ K) that can be assumed for the presented case (see Wärmeatlas Cc1-Cc4).

If $\dot{Q}_{radiation}$ and $\dot{Q}_{convection}$ is filled into equation 3.9, $\dot{Q}_{Total}$ of nearly 17 kW can be calculated. The required water volume flow to absorb the 17 kW can be derived from the following equation 3.11.

$$\dot{V} = \frac{\dot{Q}_{total}}{\rho_w \cdot c_w (t_2 - t_1)} \cdot 3600 \approx 0.73 m^3/h. \tag{3.11}$$

The calculation based on the water density $\rho_w = 1000$ kg/m^3, the heat coefficient $c_w = 4.18 \cdot 10^3$ J/(kg·K) and on a water temperature difference between in - and outlet of 20 K. Experimental tests at 200 kg/h air mass flow rate, at 373 K air preheat temperature for $\Phi = 0.6$ and with a cooling water temperature of 333 K confirmed the conservative estimation. The water temperature difference between inlet and outlet is only 5 K at an experimental measured volume flow rate of 0.76 m^3/h.

Air supply

Six air supply lines seen in Fig. 3.3 deliver the test rig facility with cooling air and air for the combustion process. All of them are equipped with a safety valve that limit the maximum pressure to 8 bar even though approximately 20 bar can be provided by the air screw compressor with a maximum air mass flow rate of 700 kg/h. Some of the devices connected with the air lines e.g. the laminar flow element (LFE) are only designed for a maximum pressure of 10 bar gauge. The air distributor was designed for 40 bar pressure gauge. Two LFEs from Meriam and Hastings Instrument can be mounted into the air supply line. While the Meriam LFE is designed for air mass flow rates up to 730 kg/h, the LFE from Hastings Instrument is able to measure up to 450 kg/h. A straight pipe before and after the LFE has to be mounted to guarantee correct flow inlet and outlet conditions. The installed pipe before the LFE is 9.3 LFE-diameters long and 4.6 LFE-diameters behind the LFE that exceed the required minimum length of 5 LFE-diameter before and 3 LFE-diameters after the LFE.

Natural gas supply

The fuel for the pilot and main combustion is delivered by the GASAG gas network that is directly connected with the gas supply line of test rig facility. To increase the fuel pressure from ≈ 100 mbar up to 9 bar gauge, a piston gas compressor is used. Under these conditions, the gas compressor is able to deliver a continuous fuel mass flow rate of 85 kg/h, which is still below the maximum allowed fuel amount of 90 kg/h restricted by GASAG. At fuel mass flow rates greater than 90 kg/h, the static pressure at the compressor inlet drops below ambient pressure as a result air might sucked into the line at emergency cases. Currently, the test rig facility cannot be operated with such a high amount of fuel as some of the components are not yet designed for the power (see section 3.3). Moreover, the fuel line "combustion" is equipped with only one coriolis massmeter that limits the fuel mass flow rate to 29 kg/h at 10 bar (absolute) as it can be seen in Fig. 3.4. At higher mass flow rates, the Mach number

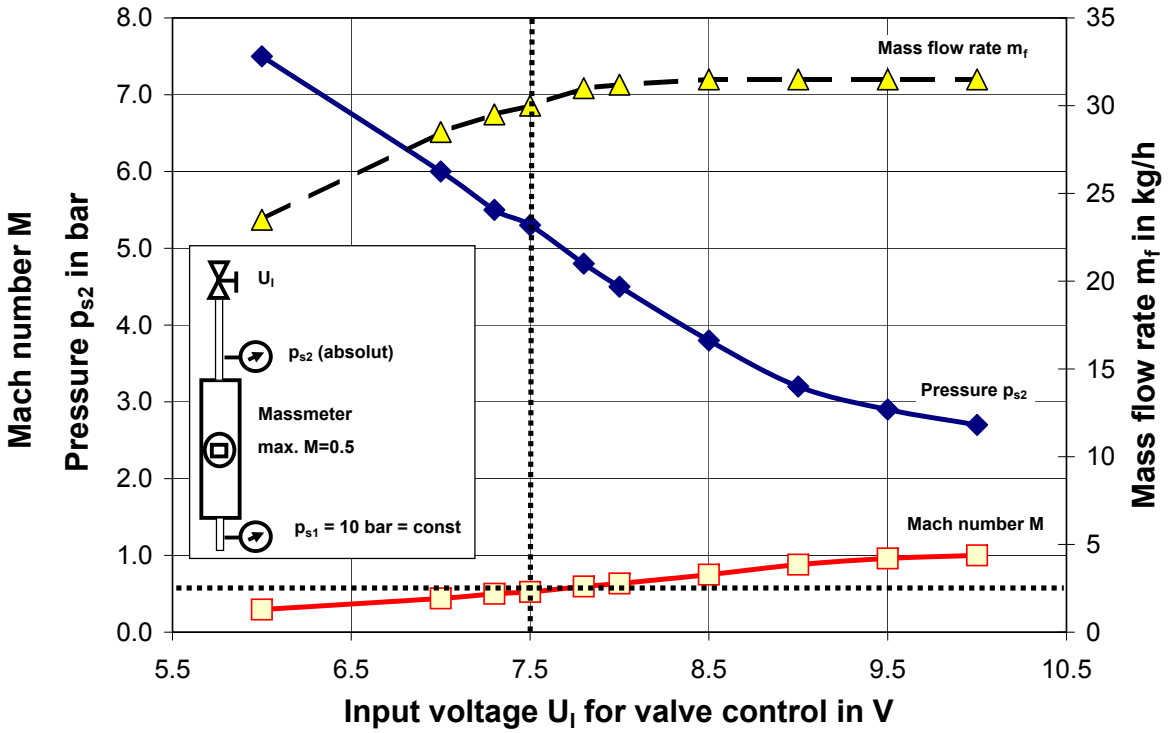

Figure 3.4: Measurement limit of the coriolis massmeter at Mach number M=0.5.

limit of 0.5 for the coriolis massmeter would be exceeded and measurement errors would significantly increase. Note, the coriolis massmeter tube has only a 3.5 mm tube diameter. A static pressure of 5.3 bar shortly behind the coriolis massmeter could be measured at these conditions so that the corresponding Mach number of 0.5 can be calculated iteratively using the following equations:

$$t_s = \frac{T_T}{(1+(\frac{\kappa_f-1}{2})\cdot M^2)} = 286K \tag{3.12}$$

$$M = \frac{c}{a_s} = 0.52 \tag{3.13}$$

$$c = \frac{\dot{m}_f}{\rho_s \cdot A} = 223m/s \tag{3.14}$$

$$a_s = \sqrt{\kappa_f \cdot R_f \cdot t_s} = 426m/s \tag{3.15}$$

$$\rho_s = \frac{p_s}{R_f \cdot t_s} = 3.9kg/m^3 \tag{3.16}$$

The temperature upstream of the coriolis massmeter was assumed to be $T_T = 300$ K while κ_f, R_f are mentioned at equation 3.8. Further details concerning the measurement principle are mentioned in section 4.2.

Closed loop control of the mass flow rates

During the combustion operation, the equivalence ratio, Φ_{Total}, is kept constant by using a closed loop control system for the main fuel and main air mass flow rate. Deviation in the mass flow rate are compensated efficiently and with only small oscillation amplitudes as shown in Fig. 3.8 [4]. A **P**roportional-**I**ntegral-**D**ifferential (PID) controller programmed in LabVIEW, a flow rate measurement device and a pneumatic slide valve are used to realized the closed loop (see Fig. 3.5, flow chart). For air mass flow rate a laminar flow element (LFE) is used. To keep the mass flow rate constant, the predicted mass flow rate $\underline{w}$ will be continously

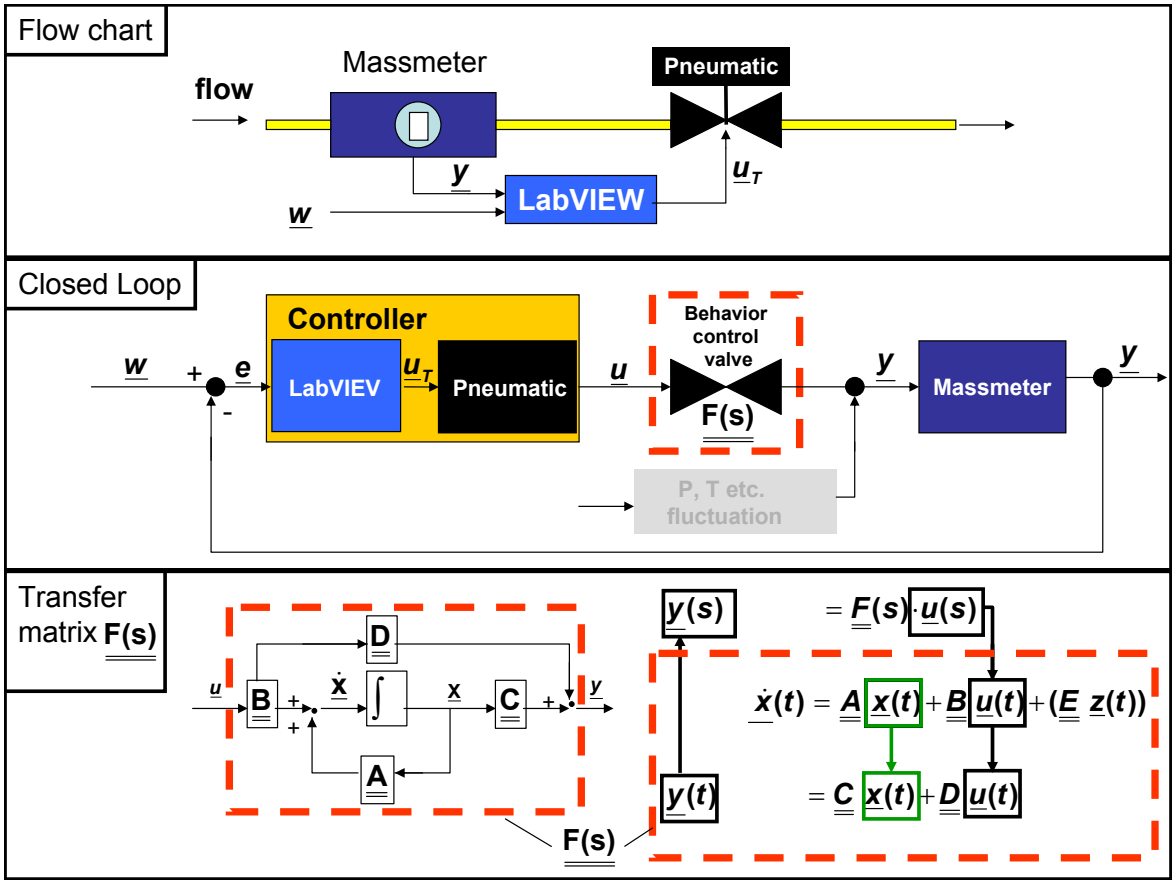

Figure 3.5: Example for flow chart and corresponding closed loop control scheme of the fuel mass flow rate.

compared with the actual mass flow rate $\underline{y}$ measured by the massmeter (see Fig. 3.5, closed loop). The deviation, $\underline{e}$, is analyzed by the PID-controller and a corresponding voltage signal $\underline{u_T}$ is generated for the pneumatic valve that varies the cross section area of the slide valve $\underline{u}$. The behavior of the mass flow rate by changing $\underline{u}$ is described by the transfer matrix $\underline{\underline{F(s)}}$ that can be derived from the states model seen in the chart "transfer matrix $\underline{\underline{F(s)}}$", Fig. 3.5. The meaning of the matrices are:

1. Dynamic matrix $\underline{\underline{A}}$ that characterizes the eigen-behavior of the system,

2. Input matrix $\underline{\underline{B}}$ that characterizes the impact of the input parameters,
3. Output matrix $\underline{\underline{C}}$ that includes the state parameters influence on the output parameter,
4. "Input-Output" matrix $\underline{\underline{D}}$ that includes the input parameters influence on the output parameters,
5. Perturbation matrix $\underline{\underline{E}}$ describes the impact of known fluctuations or uncertainty e.g. mechanical moving part could abrade with the time and the slide valve opening location would slightly differ for the same input voltage signal; thus changes the mass flow rate.

If the transfer matrix $\underline{\underline{F(s)}}$ is known, then the PID controller setup can be optimized to the slide valve behavior. In this study, $\underline{\underline{F(s)}}$ of the slide valve could not be directly determined as the cross section area of the slide valve opening, expressed by $\underline{u}$, is unknown (see Fig. 3.5, closed loop). To circumvent this problem, the pneumatic behavior of the controller is taken into acount to investigate the mass flow rate for different pneumatic pressures. Both, $\underline{\underline{F(s)}}$ of the slide valve and the pneumatic behavior of the slide valve is referred to as adjustment characteristic of the slide valve and can be investigated when the mass flow rates (through the slide valve) are represented at different input voltages $\underline{u_T}$ of the slide valve pneumatic system as shown in Fig. 3.6. Preliminary tests have shown that the mass flow rate could be

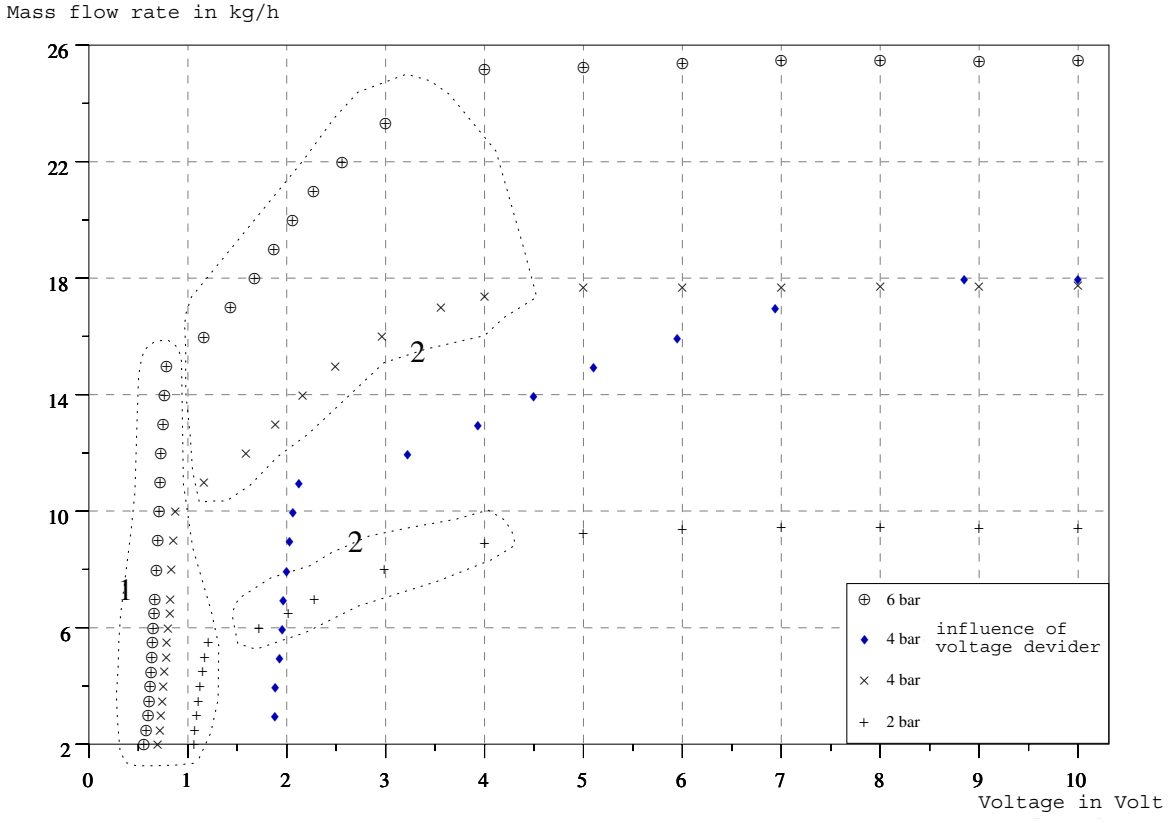

Figure 3.6: Adjustment characteristic of the fuel slide valve for different pneumatic pressure.

only adjusted between 0 and 5 Volt even though the input voltage can be varied between 0 and 10 Volt (see Fig. 3.6 case 2 bar, 4 bar (cross marker) and 6 bar). If a voltage devider is embedded into the controller then the mass flow rate can be varied up to input voltage of 9 Volts (see Fig. 3.6, case 4 bar, diamond marker). Further details are mentioned in [100, 13].

Safety measures

Different safety measurements were integrated within the test rig facility to guarantee the monitoring and the shutdown of the combustion process in emergency cases. Emission sensors for methane CH_4 and carbon monoxide CO were installed in the laboratory will activate the electromagnetic valves, referred as "security valves" in Fig. 3.3, if the CO concentration exceeds the MAK limit[1] or the CH_4 concentration within the air exceeds 40 % of the lower explosion limit. Furthermore, a pressure sensor was installed within the exhaust duct to check exhaust operation.

3.3 Operating limits

The operating range of the atmospheric single burner test rig facility seen in Fig. 3.7 is limited by several factors:

1. the used auxiliary power supplies,
2. thermal load capacity,
3. safety restrictions,
4. the static stability (lean blowout limit).

Currently, several auxiliary power units from a smaller test rig facility are used that limit the fuel and air mass flow rate. Therefore, the EV-10 cannot be operated in the range of 0.45 MW (section 3.1), even though all supply lines were designed for the power. The maxi-

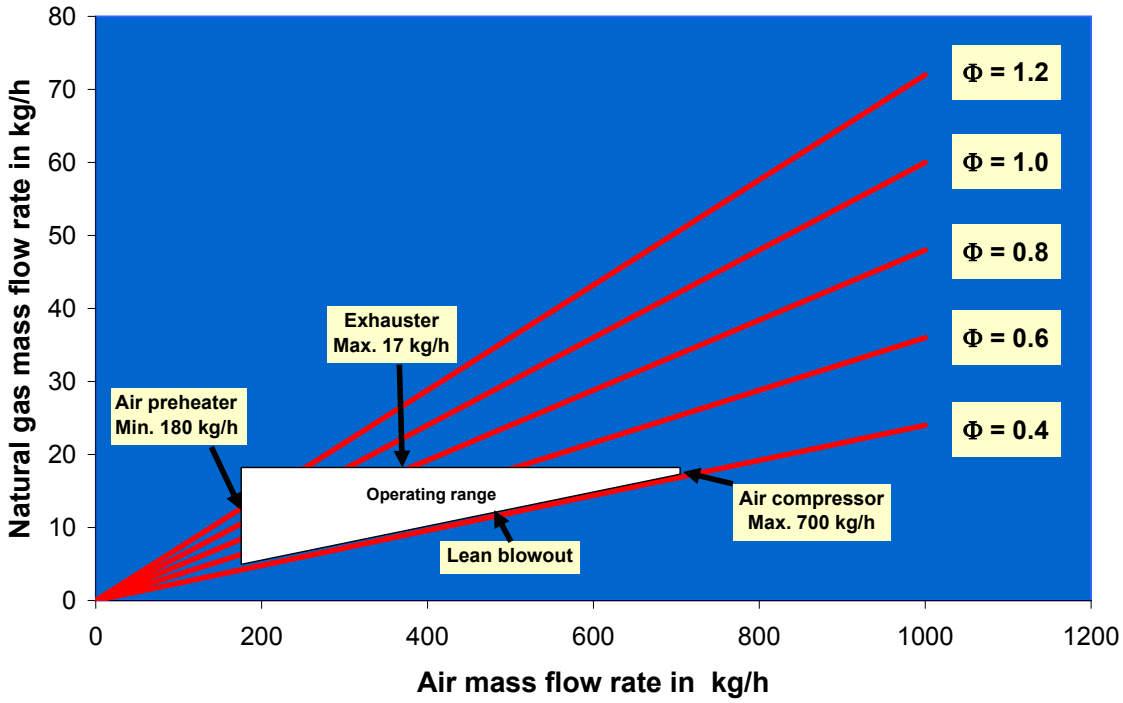

Figure 3.7: Operating limits of the swirl-stabilized combustor EV-10.

mum fuel mass flow rate is restricted by the maximum allowable exhauster blade temperature

[1]MAK(Maximale Arbeitsplatz Konzentration) limit for CO: 30 ppm

of 450 K. The material temperature is achieved at 17 kg/h respectively ≈ 240 kW. Moreover, the German "TÜV"(Technischer Überwachungsverein) demands that the fuel concentration within the exhaust must not exceed 25 % of the lower explosion limit under any operating conditions. If the lower explosion limit is assumed to be at an equivalence ratio Φ_{LBO} of 0.35 where lean blowout (LBO) definitely occurs under atmospheric condition and 600 K preheat air temperature. then 25 % of the lower explosion limit at lean blow out can be derived from an averaged stoichiometric $FAR_{stoic} = 0.0585$ for natural gas (Berlin):

$$FAR_{25\%} = \Phi_{LBO} \cdot FAR_{stoich} \cdot 0.25 = 5.125 \cdot 10^{-3}. \tag{3.17}$$

To calculate the TÜV restricted fuel mass flow rate that can be left unburned (worst case) through the exhaust duct, the maximum air mass flow rate of the exhauster, Staefa Wirz, type-025/500 is required. Under ambient conditions (300 K, 1 bar), an electrical power of 8.9 kW was measured at 2900 RPM that corresponds with an air mass flow rate of 5400 m^3/h. The air mass flow rate decreases with increasing exhaust temperature and achieved its minimum of $\dot{m}_{Air,min} = 4500$ kg/h at the maximum allowable temperature of 450 K. The air density can be calculated at $\rho_{air} = 0.78$ kg/m^3 under these conditions. The maximum fuel mass flow rate allowed by TÜV can be derived from equation 3.18 with the minimum air mass flow rate and with $FAR_{25\%}$ from equation 3.17

$$\dot{m}_{F,max,TV} = \dot{m}_{Air,min} \cdot FAR_{25\%} < 21.6 kg/h. \tag{3.18}$$

Therefore, no explosive mixture can be generated within the exhaust duct if the maximum fuel mass flow rate of 17 kg/h (restricted by the exhauster) is left unburned through the exhaust duct. Other limitation factors of the maximum achievable heat release is the air compressor with a maximum continuous air mass flow rate of 700 kg/h and the preheater with a minimum air mass flow rate of 180 kg/h. If the preheater is operated lower then this value, the maximum allowable preheat temperature of 750 K might be exceeded at maximum power. The lower operating limit is defined by the lean blowout limit, varied from $\Phi_{total} = 0,35$ - $0,55$ depending on the air preheat temperature and the amount of injected pilot fuel.

Test operation

Constant operating and test conditions are essential to show the advantage of premixed pilot flames when compared to diffusion pilot flames. The emission level, the lean blowout limit and also the RMS pressure level are influenced if air mass flow rate and preheat temperature cannot be kept constant. Therefore, conditions have to be found where temporal fluctuations of operating parameters e.g. mass flow rate fluctuations, are minimized. In this study, the equivalence ratio was changed by varying the fuel mass flow rate while the air mass flow rate was kept constant. Tests at different air mass flow rates (200 kg/h, 225 kg/h, 250 kg/h) have shown that the smallest fluctuations can be achieved when the test are conducted with 200 kg/h main air mass flow rate and 530 K preheat air temperature (see Fig. 3.8). The fluctuation of Φ is shown and is caused by a combination of air mass and fuel mass flow rate fluctuations. Nevertheless, the comparability among the test results could only be guaranteed if the tests were conducted shortly after each other [9]. Four different operating parameters are able to influence the emission and the RMS pressure level: the natural gas composition, the preheat temperature of the main air mass flow rate and the mass flow rate of the main air and main fuel.

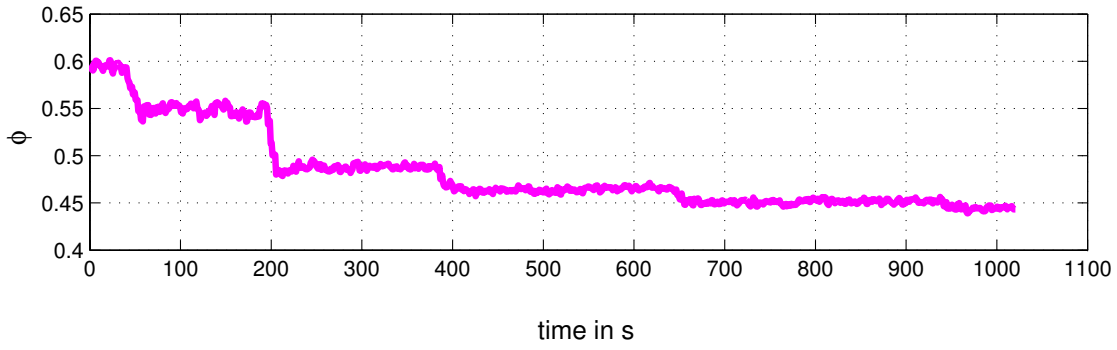

Figure 3.8: Fluctuation of Φ at 200 kg/h air mass flow rate and at different fuel mass flow rates. The air preheat temperature was constant at 530 K.

1. **Natural gas compositions:** The fluctuation of natural gas compositions, especially the methane fraction, was not investigated closely during the tests as the daily, monthly and annular methane fraction fluctuations do not differ significantly, as discussed in [9]. To further reduce the influence of methane fraction fluctuations on the test results, the test series should be conducted shortly after each other.

2. **Preheat temperature:** It could be shown in various tests that the influence of air preheat temperature fluctuations decrease with increasing averaged air preheat temperatures. The lowest relative deviation of approximately 2% was found at an air preheat temperature of 570 K that was also chosen for the tests under preheated conditions in this study. High preheat temperatures are especially desired for NO_x emission investigations to generate a comparable NO_x formation to real gas turbines. It is worth noting that the location for the preheat temperature measurement is approximately 1.2 m upstream of the combustor dump plane (see Fig. 5.1). Therefore, the set 570 K preheat temperature does not correspond with the air inlet temperature into the combustion chamber. Different experimental tests have shown that an averaged temperature difference of approximately 25 K between these two points has to be taken into account.

3. **Fuel and air mass flow rate:** While very low fuel mass flow rate fluctuations of 0.05 kg/h can be achieved, independent of the averaged fuel mass flow rate, the amplitude of main air mass flow rate fluctuations increase with increasing averaged air mass flow rate. The largest deviations were measured at 250 kg/h main air mass flow rate and were in the range of 5-10 kg/h. For this reason, the influence of premixed pilot flames on the main combustion was investigated at 200 kg/h air mass flow rate to keep the impact on the equivalence ratio low (see Fig. 3.8).

Moreover, the variation of other parameters e.g. cooling air for the combustion chamber and the exhaust mass flow rate through the emission analyzer, did not influence significantly the emission level. The emission level is influenced, as expected, when different pilot lance outlet geometries[2] were used. From their results it could be concluded that higher pilot fuel mass flow rates than 0.53 kg/h have to be chosen for the lean blowout extension tests (see section 6.2) to see the difference in NO_x emission with diffusion pilot flames and with premixed PFI-flames.

[2] conventional pilot lance and PFI-lance (see [9])

Chapter 4

Measurement principles

For the combustion tests described in this study, several sensors were installed within the test rig as shown in Fig. 4.1:

1. Laminar flow element from Meriam Instruments for air volume rate measurement.
2. Coriolis massmeter from Endress & Hauser, type PROline Promass 80 A for direct measurement of mass flow rate.
3. 1.5 mm K-type thermocouples from Newport OMEGA with a maximum temperature limit of approximately 1500 K.
4. $OH^{\star}$-photomultiplier (Hamamatsu H5784-03) equipped with a bandpass filter centered at 312 $\pm$2 nm to observe the qualitative behavior of the heat release rate fluctuation.
5. Exhaust analyze system (ABB, Advance Optima) for NO_x, CO_2, CO and O_2 measurement.
6. Watercooled 1/4“ condenser microphones (G.R.A.S.).

Note, the laminar flow element (LFE) is able to measure a volume flow rate of maximum 612 m^3/h and can be operated up to a gauge pressure of 10.3 bar. To get a corresponding air mass flow rate, the flow pressure and flow temperature is also measured inside of the tube. For fuel mass flow rate measurement, a coriolis massmeter with a maximum measurement range between $0.1 - 90$ kg/h was chosen. Thereby, the maximum gauge pressure limit is 160 bar. In the next sections, the measurement principle of each sensor will be discussed in detail.

4.1 Volume flow rate

The LFE principle for volume flow rate measurement used in this study is shown in Fig. 4.2 and is based on the pressure loss that can be measured at two different axial locations. To guarantee laminar flow conditions within LFE, it consists on a huge number of straight pipes with a diameter of ≈ 5 mm each where the flow is forced through. One of these straight pipes is equiped with two boreholes where pressure lines are mounted. Finally, the pressure difference between these location can be measured by pressure transducers that are directly connected with the pressure lines and the volume flow rate can be calculated by the Hagen-Poiseuille equation for laminar pipe flows [88]:

$$\dot{V} = \frac{\pi \cdot d^4}{128 \cdot \nu \cdot \rho \cdot l} \cdot \Delta p_{loss} \tag{4.1}$$

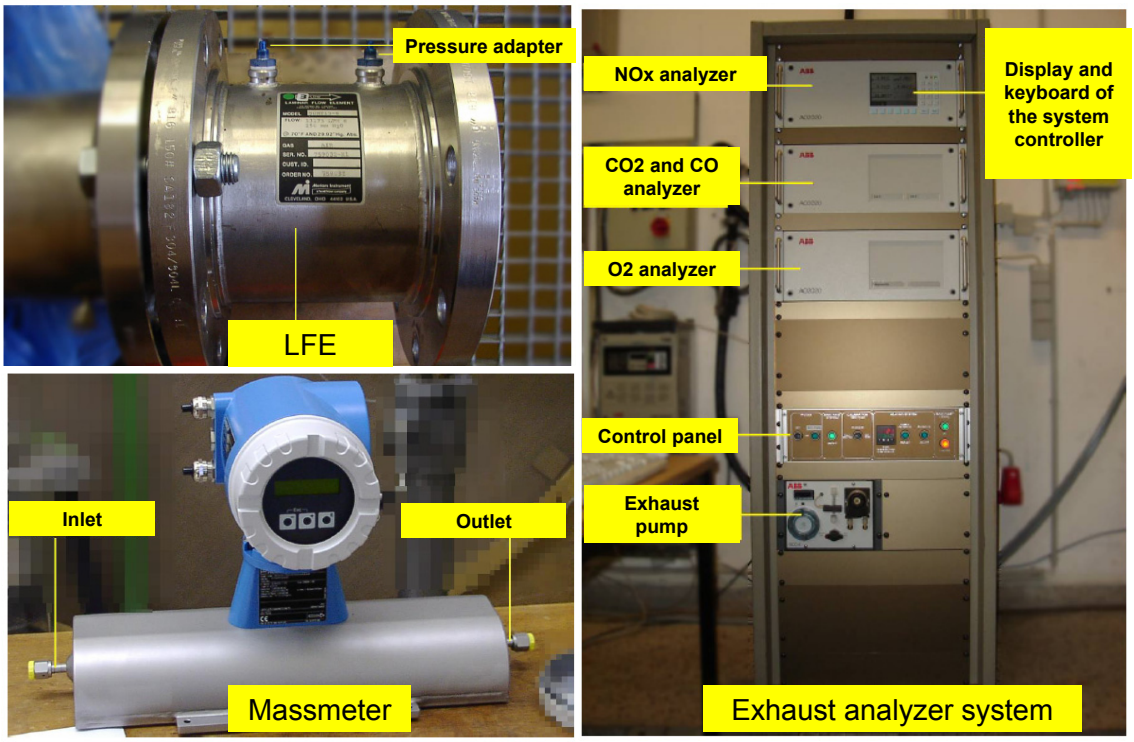

Figure 4.1: Photos of the **L**aminar **F**low **E**lement (LFE), the massmeter and the exhaust analyzer system.

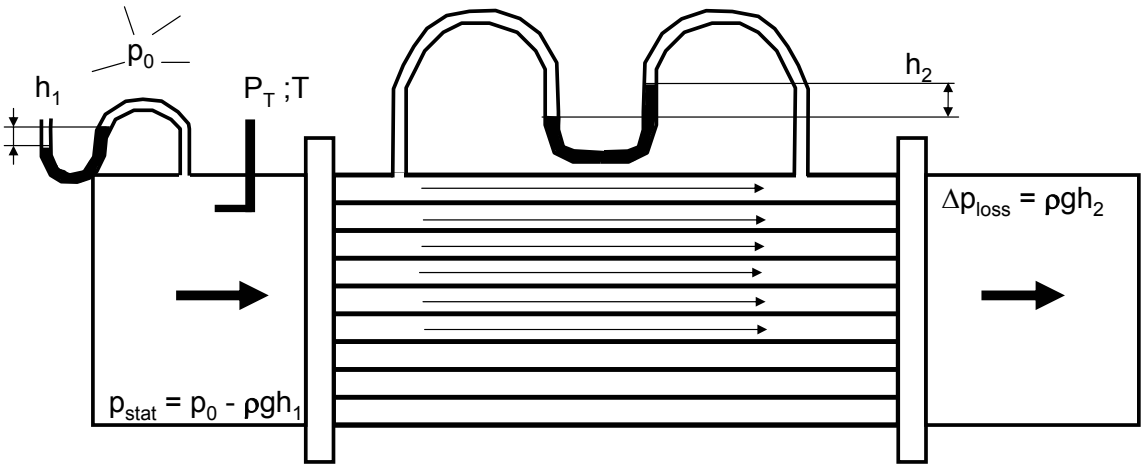

Figure 4.2: The measurement principle of the **L**aminar **F**low **E**lement (LFE).

where	d	tube diameter,
	ν	kinematic viscosity,
	Δp_{loss}	pressure loss along the tube,
	l	tube length..

Note, the required density of the flow can be derived from the measured pressure and temperature using the ideal gas law. Furthermore, it is postulated that the pressure loss Δp_i through

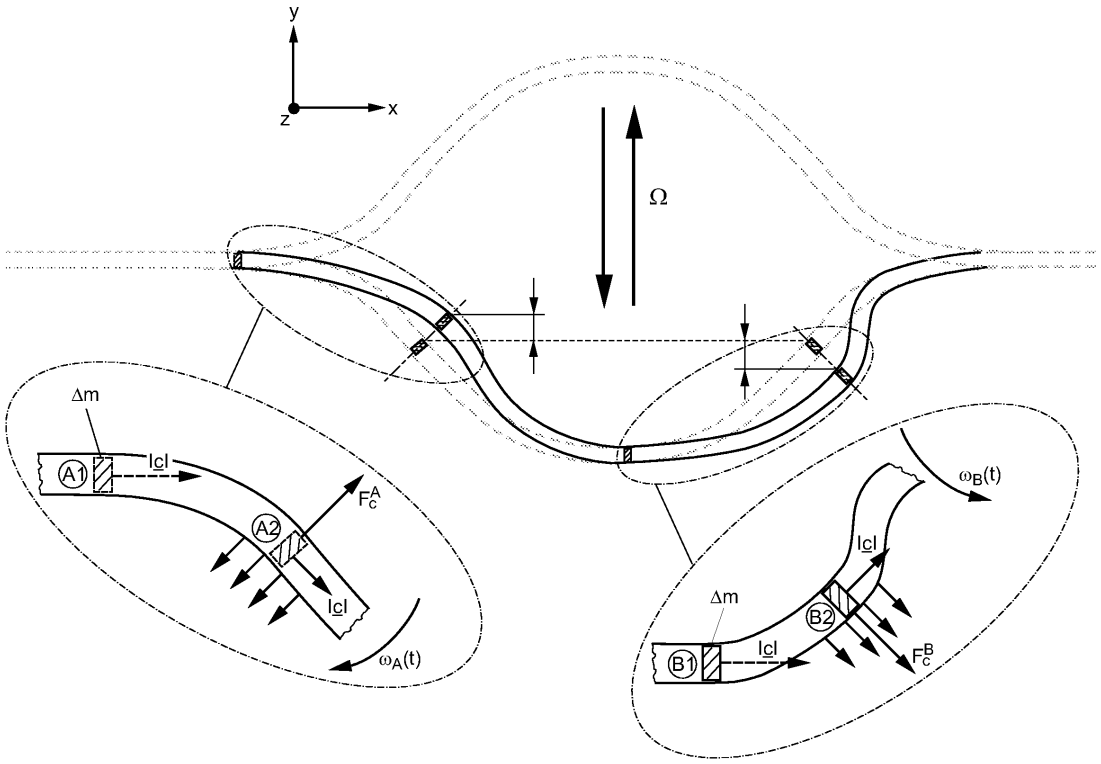

Figure 4.3: Coriolis massmeter principle.

one small, straight pipe is equal the pressure loss Δp_i through one pipe with the total cross section area of all small LFE pipes together.

4.2 Mass flow rate

The coriolis massmeter consists of a flexible tube that can be artificially, transversly excited at its resonance frequency Ω. If the oscillating tube has flow passing through it then coriolis forces bend the flexible tube ends in different directions and results a phaseshift between them that can be detected by electrodynamic sensors (see Fig. 4.3, position A2 and B2). It can be shown that the phaseshift between the two tube end location A2 and B2 will increase with increasing mass flow rate and is directly linked with increasing coriolis forces. The relationship between mass flow rate and coriolis forces can be expressed by the following equation 4.2,[38]:

$$\Delta \underline{F_c} = 2 \cdot \Delta m \cdot (\underline{\Omega}(t) \times \underline{c}) \tag{4.2}$$

with Δm mass,

$$\underline{\Omega(t)} = \begin{bmatrix} 0 \\ 0 \\ \omega(t) \end{bmatrix} \quad \text{angular velocity vector,}$$

$$\underline{c} = \begin{bmatrix} |\underline{c}| \cdot sin\phi \\ |\underline{c}| \cdot cos\phi \\ 0 \end{bmatrix} \quad \text{flow velocity vector..}$$

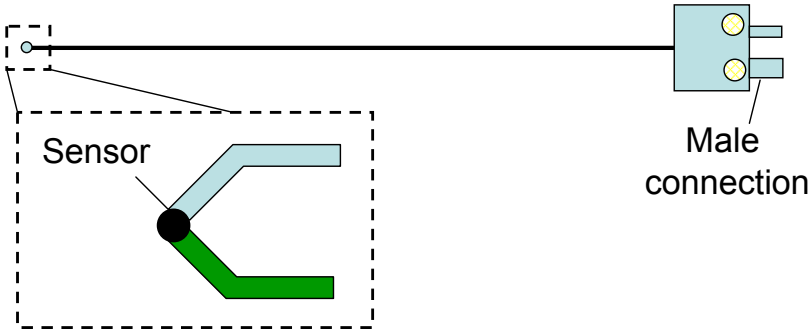

Figure 4.4: Sketch of thermocouple.

Δm can be replaced in equation 4.2 by the parameter massflow rate $\dot{m}$ as followed (equation 4.3):

$$\begin{aligned} \Delta m \cdot |\underline{c}| &= \Delta m \cdot \frac{\Delta s}{\Delta t} \\ &= \dot{m} \cdot \Delta s. \end{aligned} \tag{4.3}$$

According to the equation above, coriolis forces occur only if the tube oscillates ($\underline{\Omega(t)}$) and is flowing with a velocity ($\underline{c}$). This would also explain why both tube ends will oscillate symmetrically (no phaseshift) at flow velocities of $\underline{c} = \underline{0}$ (see Fig. 4.3, dashed lines). If the tube is flowing, coriolis forces occur and bend the tube ends in different directions as shown in Fig. 4.3, marked by continous lines. In case of position A2, the tube is bent in positive y-direction due to the coriolis force F_c^A that is pointed in the opposite direction to the tube movement. Against that, the tube end at the position B2 will be bent in the negative y-direction by the coriolis force F_c^A as it is pointed in the same direction as the tube movement. Therefore, the tube ends A2 and B2 will cross the sensors later or earlier when compared to the case at velocity $\underline{c} = \underline{0}$. The measured time difference results a phaseshift that is directly proportional to the mass flow rate through the tube [13].

4.3 Fluid temperature

Fluid temperature can be measured with different kinds of sensors; radiation thermometers and mechanical contact thermometers. The latter is the most preferable solution for combustion measurements as defined points within the combustion chamber can be monitored. In the case of the radiation thermometer, the sensor has no contact with the fluid and is only able to derive a temperature from the overall emitted fluid radiation. For this reason, mechanical contact thermometers e.g. thermocouple and resistance thermometer, are often used in combustion chambers due to their temperature range, durability and accuracy etc. In this study, several k-type thermocouples (seen in Fig. 4.4) with 1.5 mm diameter were used to monitor the temperature of the preheated air upstream and the exhaust temperatures 0.7 m and 1.48 m downstream of the burner exit. The sensor consists on two different materials that are welded together. If the temperatures at the sensor tip and the both ends differ, a voltage can be measured between the ends and is, referred to as the well-known as Seebeck-effect.

4.3.1 Seebeck effect

The discovery of this effect in 1821 can be traced back on the German scientist Thomas Johann Seebeck who showed this effect using a more simplified setup represented in Fig 4.5. He was able to measure a voltage between the rod ends when the temperatures at both ends were different. The reason for the potencial difference (measured in voltage) can be traced back to different oscillating electron velocities between the ends so that in total a greater number of electrons from the hot side can be moved to the cold side than in reverse. The process is referred as thermo-diffusion and leads to a potential difference that can be measured by a voltmeter. The increase of the potential difference $d\Phi$ and therefore the increase in voltage, U, is nearly linear with the temperature increase and results in the last term in equation 4.4, that can be split into a portion of the chemical potential and a portion of the Seebeck-term:

$$E = \underbrace{\frac{j}{\sigma}}_{\approx 0;\ \text{Portion by current flow}} + \underbrace{\frac{d\Phi}{dx}}_{\text{Portion by thermodiffusion}} \tag{4.4}$$

$$\text{with} \quad d\Phi = \underbrace{Q(T) \cdot \frac{dT}{dx}}_{\text{Seebeck-term}} - \underbrace{\frac{1}{e} \cdot \frac{d\mu}{dx}}_{\text{Chemical potential}}$$

j	Current density ($\frac{A}{m^2}$),
σ	Specific conductibility ($\frac{m}{\frac{V}{A} \cdot mm^2}$),
Φ	Electrical potential (V),
$Q(T)$	Seebeck coefficient ($\frac{V \cdot m}{K}$),
e	Elementary charge ($1.6 \cdot 10^{19}\ As$),
μ	Chemical potential ($V \cdot As \cdot m$).

E represents the electrical field strength that is related with the potential difference respectively with the voltage U by equation 4.5:

$$E = \frac{U}{s} \tag{4.5}$$

with s distance between two potential points.

The first term in equation 4.4 is equivalent to the well-known Ohm's law ($I = (1/R) \cdot U$) and can be neglected in this case as nearly no current I is able to flow in the present setup in Fig. 4.5 when the electrical circuit is open and no external voltage is applied. Only the latter is reponsible for an electrical field strength E; the so-called thermo diffusion voltage. Thereby, two terms, the chemical potential-term and the Seebeck-term, can compete with each other. While the proportion of the chemical potential increases lightly from the hot to the cold end, the proportion of the Seebeck-term decreases significantly in the same direction. Therefore, the electrical potential $d\Phi$ is mainly influenced by the Seebeck-term and not by the slightly temperature-dependent μ. The slight μ reduction with increasing temperature can be traced back on reduced quantum mechanics effects e.g. smaller wave lengths of the electrons (see [73]). The influence of the chemical potential on the thermo diffusion voltage can be completely suppressed if the voltage is measured at points with same temperatures. This is also more practicable and is used in today's thermocouples. Therefore, the Seebeck-term is the only source for thermo-diffusion voltage.

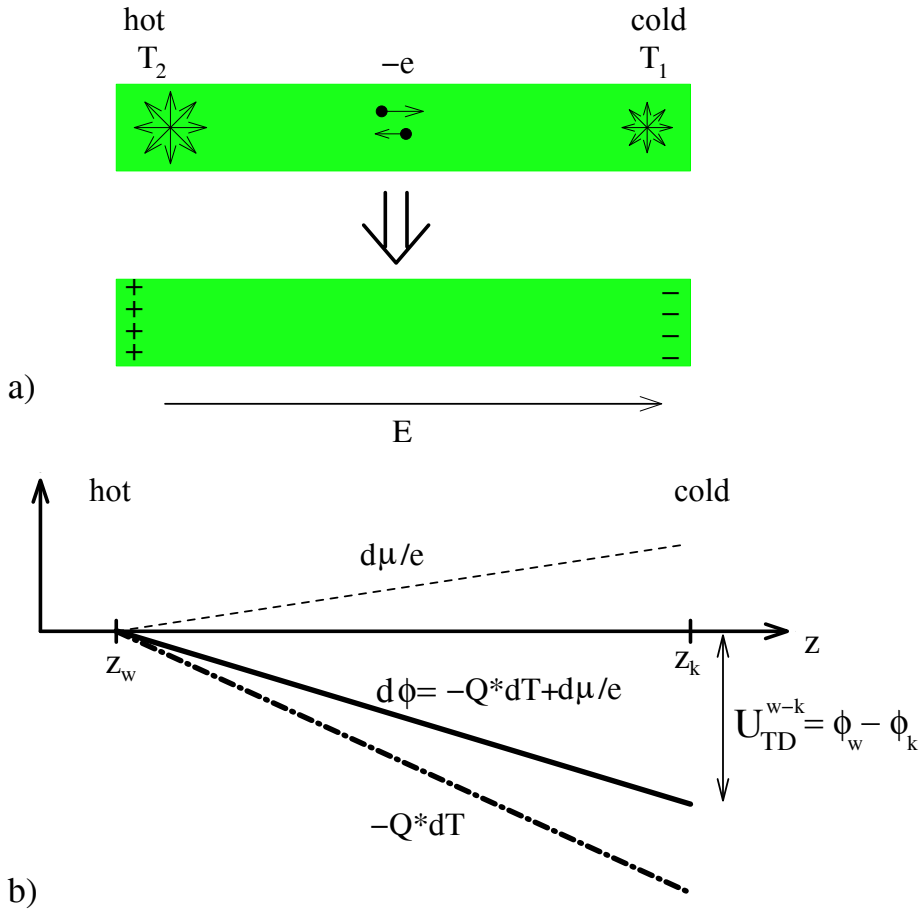

Figure 4.5: a) Diffusion of electrons from the hot side to the cold side.
b) Behavior of the electrical potential Φ (see [73]).

4.3.2 Example k-type thermocouple

The behavior of the temperature, the chemical potential term, μ/e, and the Seebeck-term, QdT, behavior at different k-type thermocouple location will be discussed in the following (see Fig. 4.6). It is assumed that the thermocouple consists on two different materials B and C that are welded at the position z_3 where also the highest temperature T_2 is defined. The connection between the thermocouple ends (positions z_2 and z_4) and the voltmeter V (positions z_1 and z_3) are realized by two lines consisting of material A. The decrease/increase of T_2 to T_1 should be linear.

Thermo diffusion voltage caused by chemical potential

According to temperature curve described in Fig. 4.6, the chemical potential, μ, at the position z_1 and z_5 remain equal even though μ significant differ between the location z_2-z_4. The variation in the voltage generated by μ is less dependent on the slight temperature dependence of μ but more by the different μ_i of the materials A, B and C if an electron gas model with $k_B T \ll \epsilon^F$ is assumed (equation 4.6).

$$\mu_i \approx \epsilon_i^F - \frac{\pi^2}{12} \cdot \frac{k_B^2 \cdot T^2}{\epsilon_i^F} \tag{4.6}$$

with ϵ_i^F Fermi energy for different materials i in (eV),

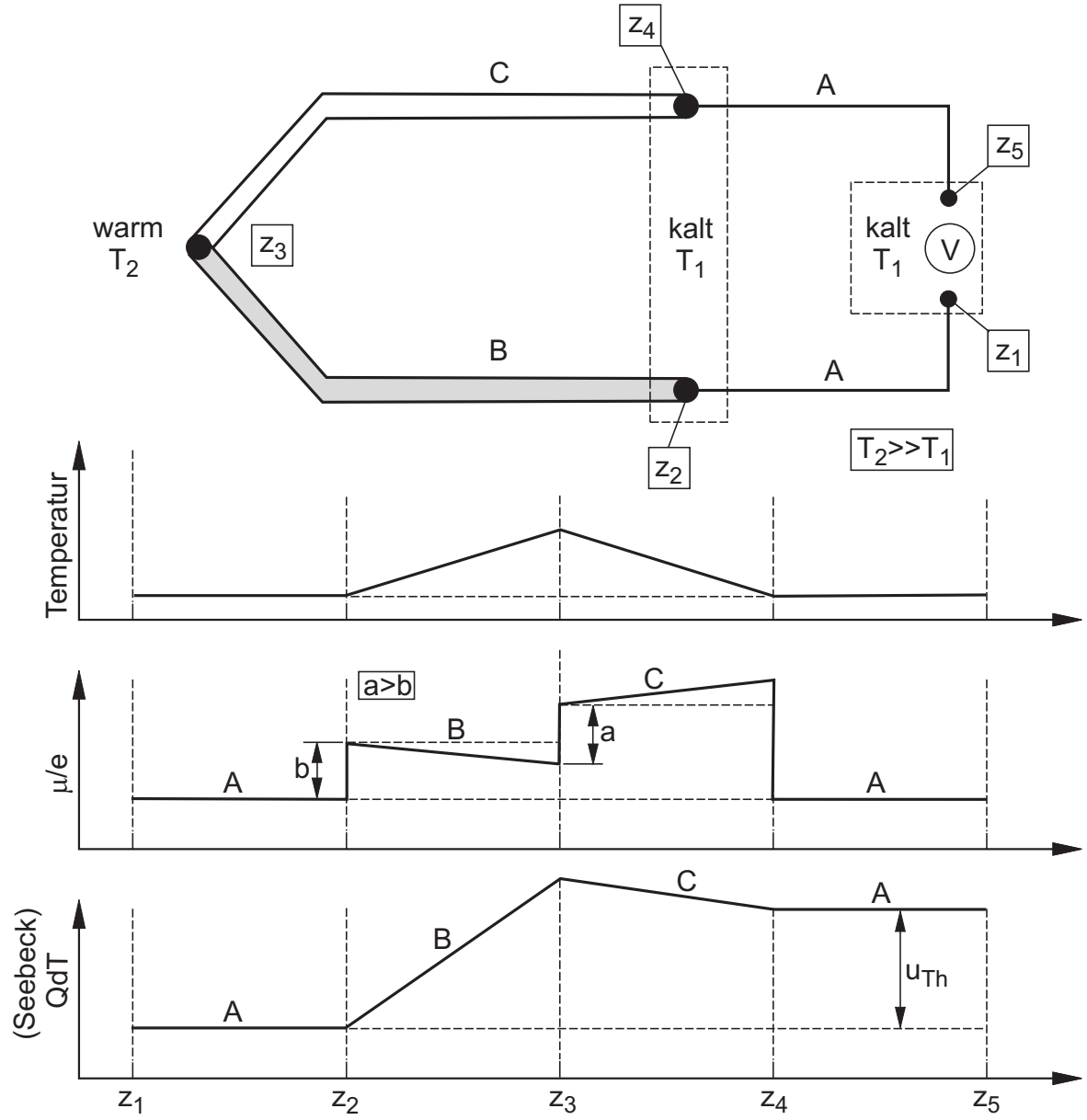

Figure 4.6: Principle of a k-type thermocouple.

k_B Boltzmann constant.

Thereby, the Fermi energy ϵ among the materials A, B and C is assumed to be $\epsilon_A^F < \epsilon_B^F < \epsilon_C^F$. In reality, the materials A, B and C can be replaced by e.g. Cu, $NiCr$ and Ni. Therefore, high voltage differences can be detected at positions where different materials are connected e.g. at position z_4. At that position, the voltage can be calculated with the following equation (4.7):

$$\begin{aligned} U_4(T) &= -\frac{d\mu}{e} \\ &= -(\frac{1}{e} \cdot (\epsilon_A^F - \epsilon_C^F) + \frac{\pi^2 \cdot k_B^2}{12e} \cdot (\frac{1}{\epsilon_A^F} - \frac{1}{\epsilon_C^F}) \cdot T^2). \end{aligned} \tag{4.7}$$

The temperature-dependent term in equation 4.7 is negligible as it is at least 4 to 5 orders of magnitudes smaller than the first term at ambient conditions. Based on this theoretical aspect,

the typical course of μ/e for a k-type thermocouple can be explained (compare Fig. 4.6). Between the position z_1 and z_2, the voltage is constant as the temperature and the material stay the same. The voltage increases at the position z_2, firstly, where the materials A and B are connected. But afterwards, it decreases slowly with increasing temperature to position z_3 and can be traced back to the temperature-dependent μ/e (see equation 4.6). The same reason leads to an increase of μ/e between the positions z_3 and z_4 when the temperature linear decrease. At position z_5, the same voltage level as in z_1 is achieved again that can be proved with the following equation (4.8):

$$\begin{aligned} U_{z_5}(T_5) - U_{z_1}(T_1) &= 0 \\ &= U_{z_4}(T_4) + U_{z_2}(T_2) + U_{z_3}(T_3) \\ &= \frac{1}{e}(\epsilon_A^F - \epsilon_C^F) + \frac{1}{e}(\epsilon_C^F - \epsilon_B^F) + \frac{1}{e}(\epsilon_B^F - \epsilon_A^F). \end{aligned} \tag{4.8}$$

The temperature-dependent portion of μ/e is zero as both positions z_5 and z_1 referenced to the same temperature.

Thermo-diffusion voltage caused by the Seebeck effect

In contrast, the thermo-diffusion voltage due to the Seebeck effect does not vanish at z_1 and z_5 as it can be seen in Fig. 4.6. While the voltage is still constant between z_1 and z_2, the Seebeck-term increases continuously with increasing temperature until position z_3. After this position, the voltage is decreased again to a lower temperature at position z_4. The voltage drop is much lower in this case because a material C with a much lower Seebeck coefficient Q_C is taken in praxis to maintain the voltage at z_4 respectively z_5 at a high level. If the sum of all voltage fraction is calculated in equation 4.9:

$$\begin{aligned} U_{z_2} &= -\frac{1}{e}(\mu_B(T_2) - \mu_A(T_2)) \\ U_{z_3-z_2} &= Q_B(T_3 - T_2) - \frac{1}{e}(\mu_B(T_3) - \mu_B(T_2)) \\ U_{z_3} &= -\frac{1}{e}(\mu_C(T_3) - \mu_B(T_3)) \\ U_{z_4-z_3} &= Q_C(T_2 - T_3) - \frac{1}{e}(\mu_C(T_2) - \mu_C(T_3)) \\ U_{z_4} &= -\frac{1}{e}(\mu_A(T_2) - \mu_C(T_2)) \end{aligned} \tag{4.9}$$

then the measured thermo-diffusion voltage at z_5 and z_1 is

$$\begin{aligned} U_{z5} - U_{z1} &= U_{z2} + U_{z3-z2} + U_{z3} + U_{z4-z3} + U_{z4} \\ U_{Thermo} &= (Q_B - Q_C) \cdot (T_3 - T_2). \end{aligned} \tag{4.10}$$

If the temperature will differ at z_4 and z_5 (z_1 and z_2) or cannot be kept constant then a voltage gradient due to the temperature depending μ has to be taken into account. Especially, thermocouples for flame temperature measurement should be extended by lines with same materials as it can be assumed that the temperature near the combustion test rig will vary. Furthermore, the temperature has to be measured at position z_1 and z_5 to compensate the effects of temperature depending μ.

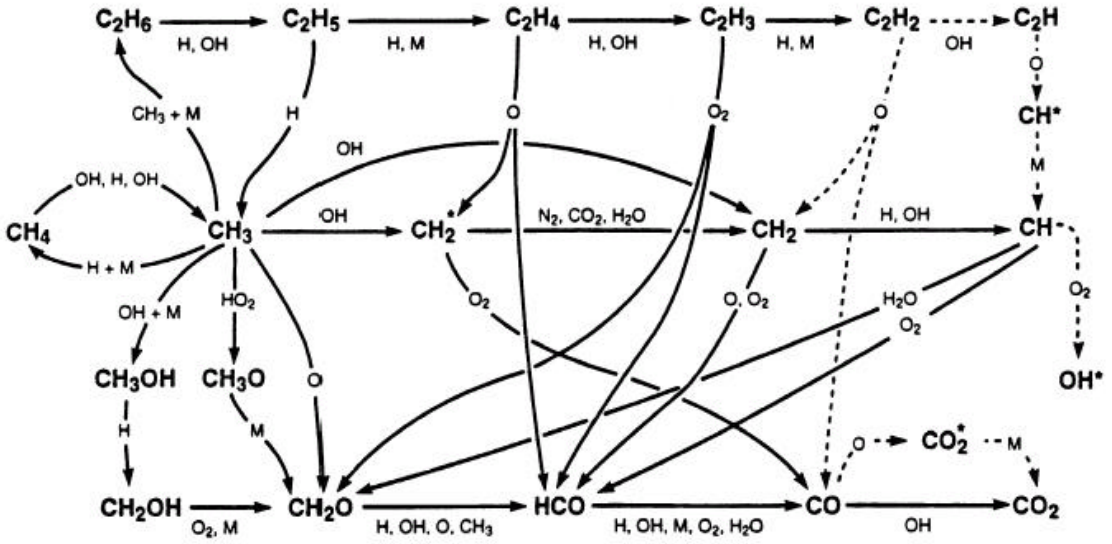

Figure 4.7: Reaction diagram for methane oxidation (Ref. [33]).

4.4 Reaction zone characteristic

The characteristic of a reaction zone, the position and size of the flame within the combustion chamber, can be detected by emitted photons from excited radicals like OH^*, CH^*, C_2^*, HCO^* that are generated during the chemical reaction. As the most excited radicals like OH^* and CH^* are generated quickly in the beginning of the ignition process and emit photons shortly after, the reaction zone of the combustion can be located with high precision (see [97]). The "number" of photons with a certain "wavelength band" is proportional to the concentration of radicals generated within the reaction zone. In this study, these photons with a certain wavelength were detected by an intensified charge-coupled device (ICCD) camera and a photomultiplier equipped with a bandpass filter centered at 312 ±2 nm.

4.4.1 Generation of excited OH^* radicals

During the ignition of the fuel/air mixture, the reactants do not transform by one chemical reaction into the products, instead the reaction takes place in small steps. Najm [33] has proposed the reaction diagram for a methane flame seen in Fig. 4.7, where the mechanism of OH^* generation can be extracted (equation 4.11).

$$CH + O_2 \rightharpoonup CO + OH^* \tag{4.11}$$

It can be concluded from this equation that excited OH^* radicals are directly generated by the reaction of CH and O_2. Most of them fall back into a ground electronic state (non-excited OH radical) after a typical lifespan of 10^{-5} s - 10^{-8} s and can emit photons. The process is also known as "chemiluminescence". They could be excited again by molecule collision and thermal excitation respectively but the concentration rate of OH^* radicals is small when compare to the rate of chemical reaction [26]. Another mechanism represents the artifical excitation by a laser beam e.g. used to detect existing OH^*-radicals within the exhaust [97]. Thereby, the concentration of OH^* within the exhaust is proportional to the number of photons (intensity) detected with the ICCD camera equipped with an OH-filter.

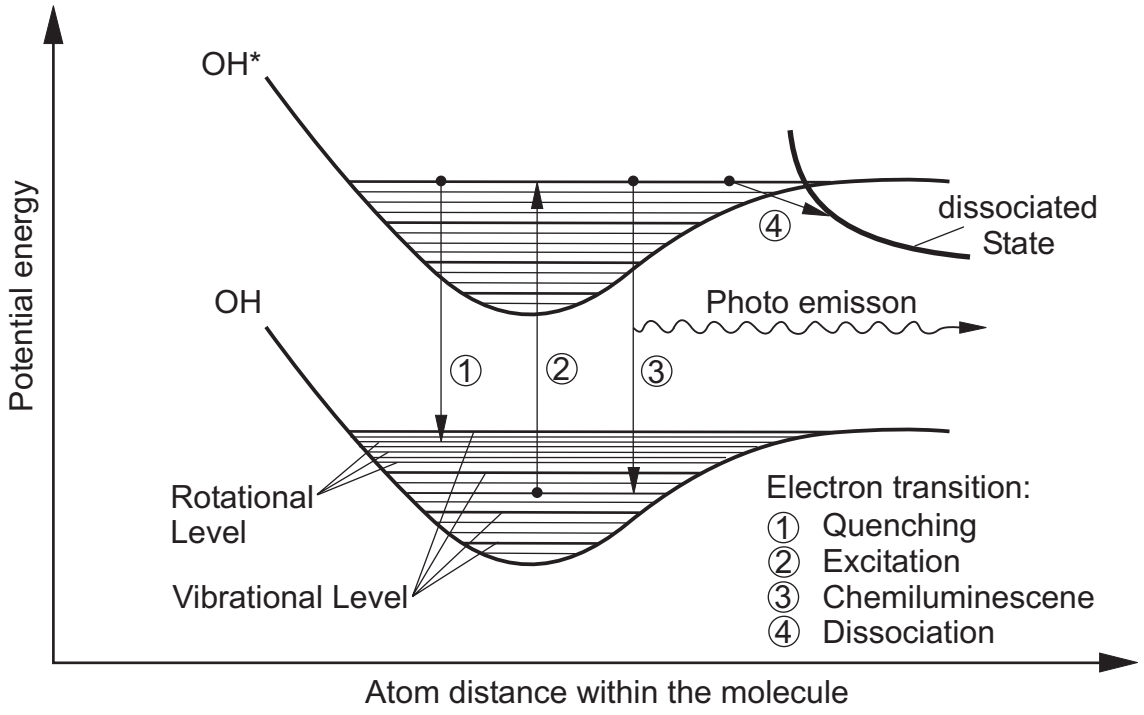

Figure 4.8: Energy level diagram of the OH radical.

4.4.2 Cause for the chemiluminescence

Chemiluminescence i.e. the emission of photons during the transition OH^* to OH occur only if OH^* is not affected by

- OH^* molecule collisions (quenching),
- OH^* dissociation shortly after generation.

The cases are also illustrated in Fig. 4.8 where the potential energy of OH versus the atom distance is shown. Depending on the case, OH^* can fall back into different energy levels that are referred as rotational and vibrational levels. To understand the meaning of these energy levels, the molecule structure will be shortly introduced. The electrons of the OH^*-radicals stay within the four different molecules orbitals: $1s\sigma$, $2s\sigma$, $2p\sigma$ and $2p\pi$. Thereby, the molecule orbital $1s\sigma$ belongs to the first shell located closer to the molecule center and was generated by merging O and H atom orbitals. The three other molecules orbitals belongs to the second shelf located further away from the molecule center. $s\sigma$, $p\sigma$ and $p\pi$ defines the shape of the orbitals. Each of the orbital can be occupied with only a certain number of electrons. While the $p\pi$ orbital can taken up 4 electrons, the other orbital of the OH radical can only take 2 of them. The number of electrons in each orbital is mentioned by a suffix and characterized an excited or non-excited radical. The difference of the ground electronic and the excited state of the OH radical can be seen in equation 4.12 (see [22]):

$$\begin{aligned} &\text{ground electronic state:} && (1s\sigma)^2(2s\sigma)^2(2p\sigma)^2(2p\pi)^3 \\ &\text{excited electronic state:} && (1s\sigma)^2(2s\sigma)^2(2p\sigma)^1(2p\pi)^4 \end{aligned} \tag{4.12}$$

Electron within the $p\pi$ orbital falls back into the $p\sigma$ orbital of the same shelf while it emits a photon. The wavelength of the photon is strongly dependent on the free energy E during the

electron transfer to the lower level (equation 4.13, [65]):

$$\nu = \frac{E}{h}. \tag{4.13}$$

If the electron falls to a lower energy level, then the total energy level of the OH^* molecule changes (Fig. 4.8). Thereby, the total energy level of the molecule is distributed on three different levels, the electronic potential, vibrational and rotational level, whereas every level can only absorb a discrete amount of energy. The electronic potential contains the energy of the moving electrons between the orbitals and also represents the majority of the total energy. Some proportion of energy can be saved within the vibrational level that represents the energy of the oscillation of the atoms within the molecules. The smallest amount of energy is saved within the rotational level and refers to the rotational movement of the molecules. Electrons of the excited OH^* radicals can be found on different vibrational and rotational levels that fall back to different energy levels in the ground state. Therefore, the emitted photon will also have a different energy and thus a different wavelength (see equation 4.13). Experimental tests have shown that the most photons with a wavelength of 306.4 nm are emitted when the electron of the excited "0" vibrational level falls back to the ground "0" vibrational level. All photons emitted under this condition belong to the (0,0) bands, independent of the rotational level. Photons can also be emitted when the electron of the excited OH^* falls back to another vibrational level of the ground state. These bands represents only 15 % of the total intensity and are emitted between wavelengths of 280 nm and 350 nm (except 306.4 nm). Further details concerning the transition probability on each of the vibrational level and the corresponding wavelengths are mentioned in [28].

4.5 Emissions

During the combustion process within the single burner test facility, the exhaust is composed of oxides of nitrogen (NO_x), carbon monoxide (CO), carbon dioxide (CO_2), unburned hydrocarbons (UHC), oxides of sulfur (SO_x), water vapor (H_2O), particulate matter (mainly carbon) and excess oxygen and nitrogen (see Table 4.1).

Table 4.1: Most relevant emissions produced by gas turbines.

Emission	**Formula**	**Density**[3]	**Effect**
–	–	**kg/m**^{3}	–
Carbon monoxide	CO	1.25	toxic
Oxides of Nitrogen	NO_x	$1.34 - 2.03$	toxic, precursor of chemical smog, depletion of ozone in stratosphere
Particulate matter (soot, smoke)	C		visible
Oxides of sulfur	SO_x	1.34	toxic, corrosive
Unburned hydrocarbons(UHC)	C_xH_y	–	toxic

[3] at 1 bar, 292 K

Carbon monoxide is able to block the capability of blood corpuscles to absorb oxygen and can cause death. It is mainly formed at low equivalence ratios where the oxidation is limited due to low combustion temperatures. At higher equivalence ratios, CO emissions can decline due to increase rate of oxidation at higher flame temperatures. If the flame temperature exceeds around 1800 K, CO_2 starts to dissociate into CO again and can formed significant concentrations. The concentration can be further reduced when the combustion takes place at higher combustion pressures. Low equivalence ratios and high pressures will accelerate the conversion of CO into CO_2 while the chemical dissociation of CO_2 into CO can be supressed at high equivalence ratios. Note, the formation of UHC is influenced by the same factors even though the reaction kinetics are different. High concentrations of UHC can be formed e.g. poor mixing and at extremely rich mixtures. It is toxic like CO and forms photochemical smog in combination with oxides of nitrogen. Particulate matter, also known as smoke or soot, might increase the danger of asthma or other respiratory diseases as studies by Seaton [91] have indicated. Soot is formed in considerable quantities when fuel pockets circulates in fuel-rich zones at high temperatures. Higher pressures also lead to increased concentration of soot and smoke and can be traced back on extented flamability limits. Therefore, the reaction between fuel and oxygen can be taken place at still richer mixture when compared at lower pressure and will increase the danger of soot formation. Oxides of sulfur are responsible for the formation of sulfuric acid in the atmosphere but has been significantly reduced in the last decades by using fuels without or low content of sulfur (natural gas). Other emissions like water vapor and carbon dioxide are responsible for global warming. While CO, NO_x, UHC and smoke concentration can be influenced significantly by flame temperature, residence time and power settings, water vapor and carbon dioxide are always formed and can only be reduced by increasing the engine thermal efficiency. Oxides of nitrogen ($NO + NO_2$) can cause photochemical smog at ground level, damage plant life and increase acid rain. NO_x leads to the formation of ozone in the troposphere (ground level to approximately 12 km) with the reaction mechanism shown in equation 4.14

$$\begin{aligned} NO_2 &= NO + O \\ O + O_2 &= O_3. \end{aligned} \tag{4.14}$$

At higher altitude than 12 km, NO_x is able to destroy the ozone via the reactions shown in equation 4.15 that reduces the capability of the stratospheric ozone layer to block ultraviolet radiation from the sun.

$$\begin{aligned} NO + O_3 &= NO_2 + O_2 \\ NO_2 + O &= NO + O_2. \end{aligned} \tag{4.15}$$

Four different mechanisms are responsible for the NO_x formation: Thermal NO_x, Prompt NO, Nitrous oxide mechanism (N_2O), and Fuel NO.

4.5.1 Mechanisms of NO_x formation

Thermal NO

Thermal NO is formed in considerable quantities at temperatures above 1800 K when atmospheric nitrogen can be oxidized according the (extended) Zeldovich mechanism (equation 4.16):

$$O_2 = 2O$$

$$\begin{aligned} N_2 + O &= NO + N \\ N + O_2 &= NO + O \\ N + OH &= NO + H \end{aligned} \tag{4.16}$$

The highest level of NO_x can be found on the fuel-lean side of stoichiometric even though the temperatures are lower when compared to the rich side of stoichiometric. The available oxygen at the rich side will be used to preferentially oxidate the fuel and not the nitrogen. Thermal NO_x formation is strongly influenced by flame temperature, pressure and combustor residence time [5, 55].

Prompt NO_x

Prompt NO is the predominant mechanism at lean conditions and can be characterized as a fast reaction between hydrocarbon radicals, oxygen and nitrogen. The presence of the mechanism was first shown experimentally in the Fenimore pioneer study with ethylene-air flames [25] and is therefore sometimes referred as "Fenimore NO_x". Considerable quantaties can be found at lower flame temperatures such as at lean conditions and at very fuel-rich conditions. The initiating reaction is shown in equation 4.17.

$$N_2 + CH = HCN + N \tag{4.17}$$

Under lean conditions, HCN can be oxidized further to prompt NO involving reaction partners CN and NCO while N reacts with OH to NO (equation 4.16, last line). From studies in [54, 55, 96] it can be derived that prompt NO_x formation is largely independent of pressure especially at low flame temperatures and low equivalence ratios Φ. The tests were conducted with either turbulent premixed methane-air flames using an uncooled perforated plate burner or with well-mixed, low temperature flames using a lean premixed burner. Leonard and Correa [55] have operated their burner at pressures from 1 to 10 atm whilst the inlet air temperature was varied between 300 K and 615 K. In tests described in [54, 96], the pressure was varied between 0.1 and 3.0 MPa and 0.1 and 0.7 MPa, respectively.

Fuel NO_x

Another source for NO_x emissions is formed by the oxidation of organically-bonded nitrogen in fuel also known as "Fuel NO_x". Thereby, the content of nitrogen in fuel can be varied between 0.06 percent (light distillate) and 2 percent (heavy distillate) so that fuel NO_x proportion of the total NO, especially at lean conditions, can also strongly vary [63]. While the natural gas contains little or no fuel-bonded nitrogen, other fuels like oil, coal or waste fuel may contain significant amounts.

Nitrous oxide mechanism

The basic reaction of the nitrous oxide mechanism is shown in equation 4.18. N_2O is formed by nitrogens and oxygen radicals and a stabilized molecule M, first. Afterwards, N_2O is oxidized to NO.

$$\begin{aligned} N_2 + O + M &= N_2O + M \\ N_2O + O &= NO + NO \end{aligned} \tag{4.18}$$

Small proportions of NO_x can be also formed by the reactions (equation 4.19, [67, 51]).

$$\begin{aligned} N_2O + H &= NO + NH \\ N_2O + CO &= NO + NCO \end{aligned} \tag{4.19}$$

It can be shown analytically in [67] that the major source of NO_x at low equivalence ratios ($\Phi = 0.5 - 0.6$) is formed by the nitrous oxide mechanism. The formation of "prompt NO_x" and "thermal NO_x" play a subsequent role under these conditions as the temperatures do not seem sufficiently high and the concentration of CH radicals might be too low to form considerable quantities of "prompt NO_x". Note, "fuel NO_x" was assumed to be zero in this study as methane was chosen. Furthermore, the mechanism seems to be largely independent of pressure near the lean blowout limit as pressurized tests with turbulent premixed flames have indicated [54, 55, 96].

4.5.2 Emission detection

In the following section, the measurement principles for detecting NO_x, CO and CO_2 and the principle for O_2 detection are described as these emissions could be analyzed by the emission analyzer system "Advance Optima 2000" used in this study [14].

NO_x and CO_x detection

Each molecule e.g. NO or CO is only able to absorb electromagnetic radiation within a specific narrow-wavelength band. NO absorbs electromagnetic radiation within the ultraviolet (UV) range while CO absorbs the radiation within the infra-red (IR) range. In general, the measurement is conducted with a lamp that emits electromagnetic waves with a defined intensity and wavelength (see Fig. 4.9), that the molecule of interest is able to absorb. One

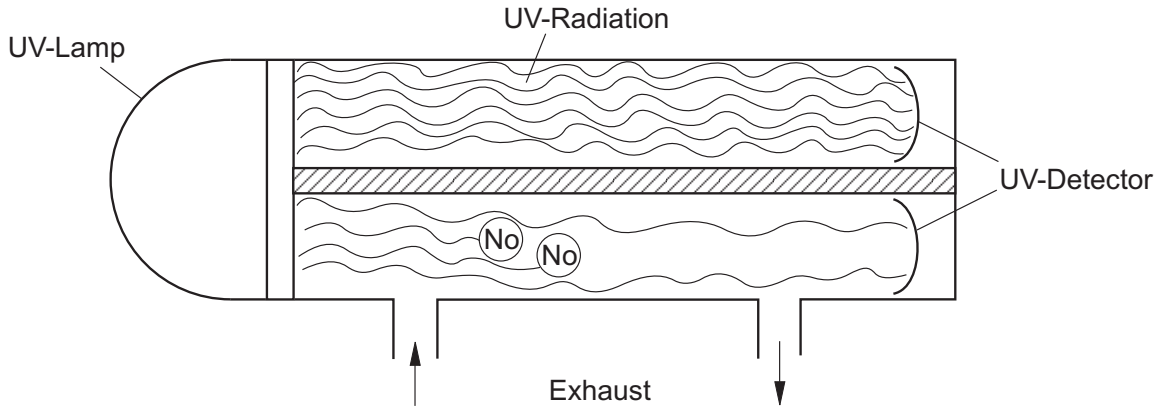

Figure 4.9: Optical measurement principle for NO_x emissions.

part of the radiation is sent through the exhaust gas where the intensity decreases depending on the concentration of the molecules of interest. The other part is led through a neutral gas where no absorption takes place. Afterwards, the intensity difference between both waves can be analyzed and represents a direct measurement for the molecule of interest concentration within the exhaust. The analysis for more-atomic molecules like NO_2 and CO_2 are similar but more complex as these molecule can absorbed radiation with different wavelengths.

O_2 detection

O_2 is one of the few molecules that shows paramagnetic behavior. For this reason, the concentration of O_2 molecules within the exhaust and therefore its partial pressure can be influenced by the magnetic field strength. In practice, the exhaust is led into a measurement chamber where a weak and a strong magnetic field are generated by magnets. Due to the paramagnetic behavior of O_2, most of the O_2 molecules will be attracted by the magnet with the strongest field so that the O_2 concentration will locally increase at that location. Thereby, a partial pressure gradient can be detected between the strong and the weak magnetic field. The difference of partial pressure between two points can be used to deflect a body. The deflection angle is direct proportional to the O_2 concentration within the exhaust.

4.5.3 Normalized NO_x emissions

In general, the measured NO_x emissions are mentioned under dry conditions and are normalized on 15 % O_2 to assess and to compare the achieved emissions level with other combustion systems or with emission limits. To transfer the measured NO_x emisions in this study, they were processed in two steps, convert from wet to dry conditions and based on 15 % O_2.
First step: The emissions within the exhaust volume are measured wet[1] by the emission analyzer system to increase the accuracy when compared to measurement under dry conditions. However, the concentration of NO_x emissions under dry conditions is more common to present as most governmental NO_x emission restriction were defined under these conditions. Fig. 4.10 shows the impact of water evaporation within the analyzer volume on the NO_x emission. The

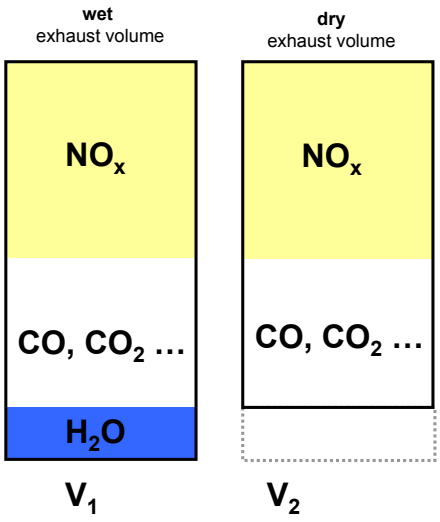

Figure 4.10: Exhaust volume at dry and wet conditions.

NO_x concentration with the unit ppmv (parts per million by volume) is based on the volume $V1$ for wet conditions, while the NO_x emissions at dry condition are based on the smaller volume $V2$. Even though the number of NO_x particles within both volumes are equal, the NO_x concentration in $V2$ is greater than in $V1$.

In a second step, the NO_x emissions were based on 15 % O_2 with the following equation 4.20,

[1] water evaporation is included within the exhaust volume

where the measured NO_x emissions and O_2 concentrations are referred to as $NO_{x,measured}$ and $O_{2,measured}$ while the ambient $O_{2,ambient}$ concentration was set on 20.9 %:

$$NO_{x,norm} = NO_{x,measured} \cdot \frac{O_{2,ambient} - 15\%}{O_{2,ambient} - O_{2,measured}} \tag{4.20}$$

4.6 Pressure fluctuations

A common principle for pressure fluctuation measurement is the use of a flexible surface that is able to oscillate in phase with pressure fluctuations. In practice, the amplitude and frequency of the flexible surface can be measured according to :

1. The inductive principle: The surface is connected with a current circuit so that its deflection induces a voltage in an adjacent located current circuit e.g. a coil. The voltage difference is directly proportional to the surface deflection and to the instant pressure level. Inductive pressure transducers should be used under constant temperature conditions otherwise the efforts required to compensate the temperature are high. Therefore, they are not suitable for combustion noise and combustion instability measurements even though they are robust and in-expensive.

2. The principle of resonance frequency measurement: A tensioned wire is forced to oscillate at its eigen-frequency by electro-magnetic excitation. If the pressure oscillations change the force of the tensioned wire, the eigen-frequency is influenced according to the following equation 4.21:

$$f_0 = \frac{1}{2} \cdot \sqrt{\frac{F}{m \cdot l}} \tag{4.21}$$

with f_0 Eigen-frequency,
F Tensioned force of the wire,
m Mass of the wire,
l Wire length.

Therefore, the change in eigen-frequency is directly proportional to the instantaneous pressure level.

3. The capacitance principle; discussed in detail in the following section as it is applied in condenser microphones used in this study.

The principle of the capacitance pressure measurement is illustrated in Fig 4.11 where one of the condenser plates represents the flexible surface that is deflected by a pressure change. If the distance between the condenser plates is changed according to equation 4.22 than the capacitance, C, is directly influenced so that a proportional relationship between the instant pressure level and capacitance exist.

$$C = \epsilon_0 \cdot \epsilon_r \cdot \frac{A}{d} \tag{4.22}$$

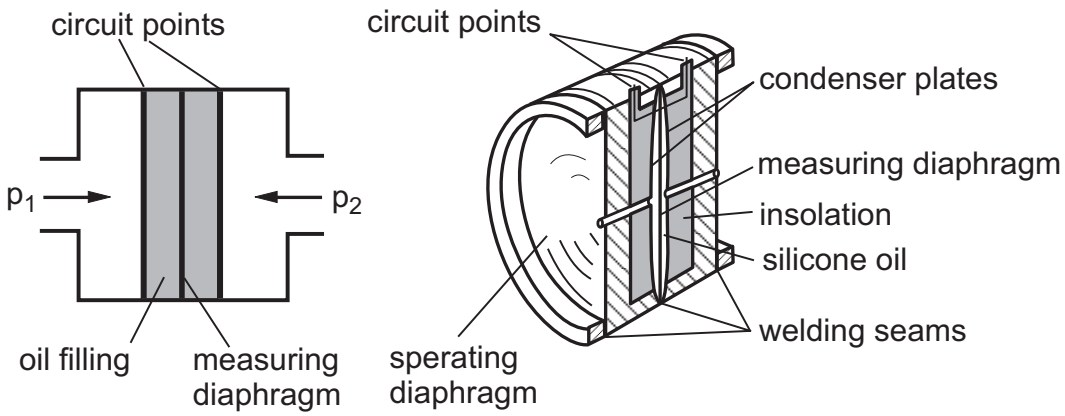

Figure 4.11: Pressure measurement according the capacitance principle.

with	C	Capacitance ($\frac{As}{V}$),
	ϵ_0	Electrical field constant ($\frac{As}{V \cdot m}$),
	ϵ_r	Dielectrical number ($-$),
	A	Condenser plate area,
	d	Condenser plate distance.

In practice, the capacitance change is realized by a deflected membrane that is located between two condenser plates. By using this configuration, the sensitivity and accuracy can be increased as the capacitance can be always measured between the deflected membrane and the condenser plate with the smallest distance. Capacitance pressure transducer can be also used in high temperature environments if a suitable cooling is available.

Evolution of pressure fluctuation with high amplitudes

Pressure fluctuations p' occur in non-reacting and reacting flows due to the presence of flow perturbations and can be generated by turbulence structures, by fluctuation in the mass flow rates etc. In reacting flows, p' can be further excited by the feedback process illustrated in Fig. 4.12, which will be discussed in more detail in this section. Lieuwen [59] summarized several instability-driving mechanisms e.g. vortex shedding, equivalence ratio oscillations, oscillatory atomization, that generate heat release fluctuations due to flow and/or mixture perturbations so that pressure waves (and density waves) can be propagated. They are reflected by the combustion chamber inner wall and propagate back to the combustor where flow and mixing perturbations can be further excited. The combustion system becomes unstable, first, when existing heat release fluctuations Q' occured in a phaseshift of less than 90° relative to p' and the acoustic energy is sufficient to exceed the dissipation losses (e.g. viscous dissipation, radiation of acoustic energy through the open end of the combustion chamber). The instability phenomenon was probably first observed by Higgins in 1777 when he generated “singing”

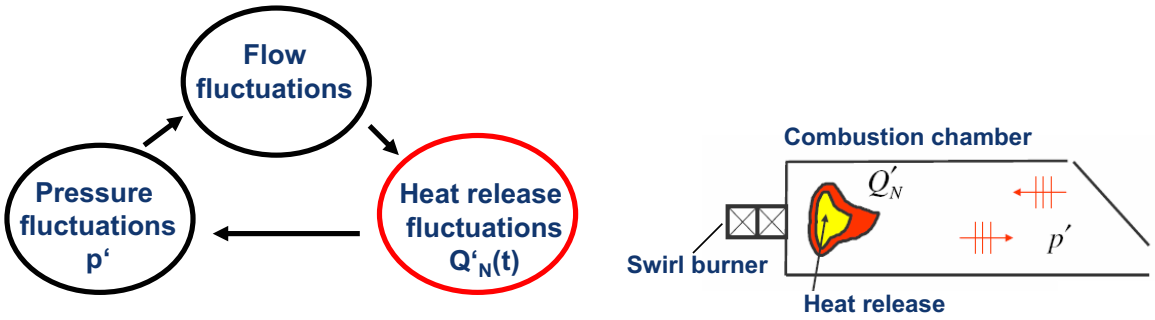

Figure 4.12: Simplified instability mechanism in reactive flows.

diffusion hydrogen flames within a tube. In the end of the 19th century, Rayleigh also observed this phenomenon and specified the conditions under which “singing flames” can only occured. Later in 1953, Putman et al. [76] derived an equation from Rayleigh statements that pressure fluctuations can only be excited by heat release fluctuations at specified phaseshifts and at acoustic energies that exceeds the dissipation losses (equation 2.1). Only at phaseshifts $0° - 90°$, pressure fluctuations are fed by the heat release fluctuations. The simplest device to generate thermo-acoustic instabilities represents the “Rijke tube” shown in Fig. 4.13. The

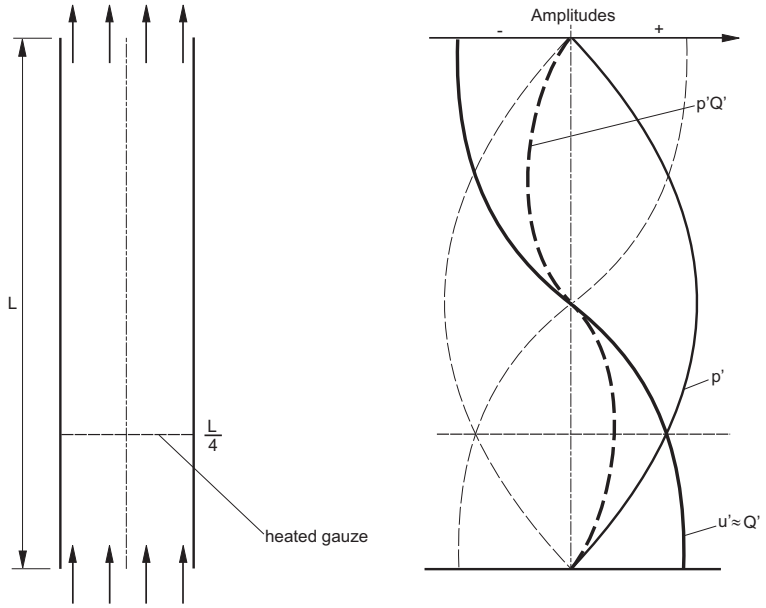

Figure 4.13: p' excitation principle within a “Rijke tube”.

tube with two open ends and a gauze at $L/4$ length was firstly mentioned in the middle of the 19th century by P.L. Rijke. Due to its simple setup, it is often chosen to explain thermo-acoustic instabilities. To simulate heat release fluctuations in a “Rijke” tube, the gauze has to be firstly heated up. Thereby, a convective flow due to the density difference is forced vertically through the gauze where small velocity fluctuations are continuously generated by small vortices, small detachments etc. The heat transfer between the gauze and the air flow is disturbed and the resulting temperature fluctuations themselve cause velocity fluctuation due

to the fluctuating expansion of air. Thereby, it is assumed that the time delay between both parameters, fluctuating air expansion and velocity fluctuation, can be neglected. To amplify existing pressure fluctuations, the phaseshift of the velocity fluctuation has to be nearly in phase with it. This condition can only be generated in the lower part of the "Rijke" tube as it can be seen in Fig. 4.13 where both parameters are nearly in phase. The best excitation of pressure fluctuations can be achieved when the gauze is located at $L/4$ of the tube.

Chapter 5

Test setup

The impact of different pilot injection locations on the proposed combustion region 3 mentioned in section 2 was investigated with the test rig setup shown in Fig. 5.1. To have full optical access to the premix flame front, a quartz glass combustion chamber was used, 0.3 m in height and 0.2 m in diameter. A 1.3 m tube extension (resonance tube) with the same diameter as the combustion chamber was mounted above the quartz glass. To record the amplitude of pressure oscillations, a water-cooled condenser microphone was mounted $y = -0.4$ m upstream of the burner outlet plane. A sample rate of 4096 Hz was set and a low-pass filter at half of the sample rate was used. The pilot fuel and the main fuel mass flow rates were measured using a coriolis massmeter, while the air mass flow was measured by a laminar flow element. All mass flows were set by metering valves that allowed a constant mass flow within a tolerance of less than 5 %. Several k-type thermocouples, with probe diameter 1.5 mm, were used to monitor the temperature of the preheated air upstream, the bottom exhaust temperature at $y = 0.7$ m, and the exit exhaust temperature at $y = 1.48$ m downstream of the combustor exit plane. The water-cooled emission probe, located 1.5 m downstream of the burner exit, consisted of a 0.3 m long tube with a diameter of 10 mm. In total, 14 boreholes were arranged on the emission probe so that 2 boreholes could be located on each of the 7 equal annular cross-sections of the exhaust duct. Thereby, the precision of the averaged emissions level could be increased as the emissions seen from each annular cross-section were equivalent. A heated flexible tube with a length of 12 m was used to lead the emissions into an analysis system, where NO and NO_2 were measured wet and CO, CO_2 and O_2 were measured dry. All emissions results presented in this study are based on 15 Vol% O_2. At a constant exhaust volume flow of 55 l/h, the emission needs approx. 40 seconds to travel from the emission probe to the analysis system. This time delay in the response of the emission recording was accounted for in the data evaluation. An OH^*-photomultiplier (Hamamatsu H5784-03) and an ICCD camera (Imager Intense of La Vision) equipped with a bandpass filter centered at 312 $\pm$2 nm were used to measure the fluctuation of the heat release rate and to visualize the flame front at unstable conditions. The ICCD camera was located 1.4 m in front of the combustion test rig center axis (see Fig. B.6) and a fiber optic cable connected to the photomultiplier was mounted very close to the quartz glass combustion chamber (0.1 m) and $y = 0.2$ m above the combustor dump. The swirl-stabilized combustor (swirl burner) seen in Fig. 3.1 was equipped with two pilot injection devices. In this study, they are referred to as "**P**ilot **F**lame **I**njector (PFI) lance" and "Pilot ring" in the following section (see Fig. 5.2). While the mixture through the PFI lance can be ignited by a spark, the mixture through the pilot ring could be only generated in the presence of the main combustion. The equipment for pilot flame generation, the components of the PFI and the electromagnetic shielding

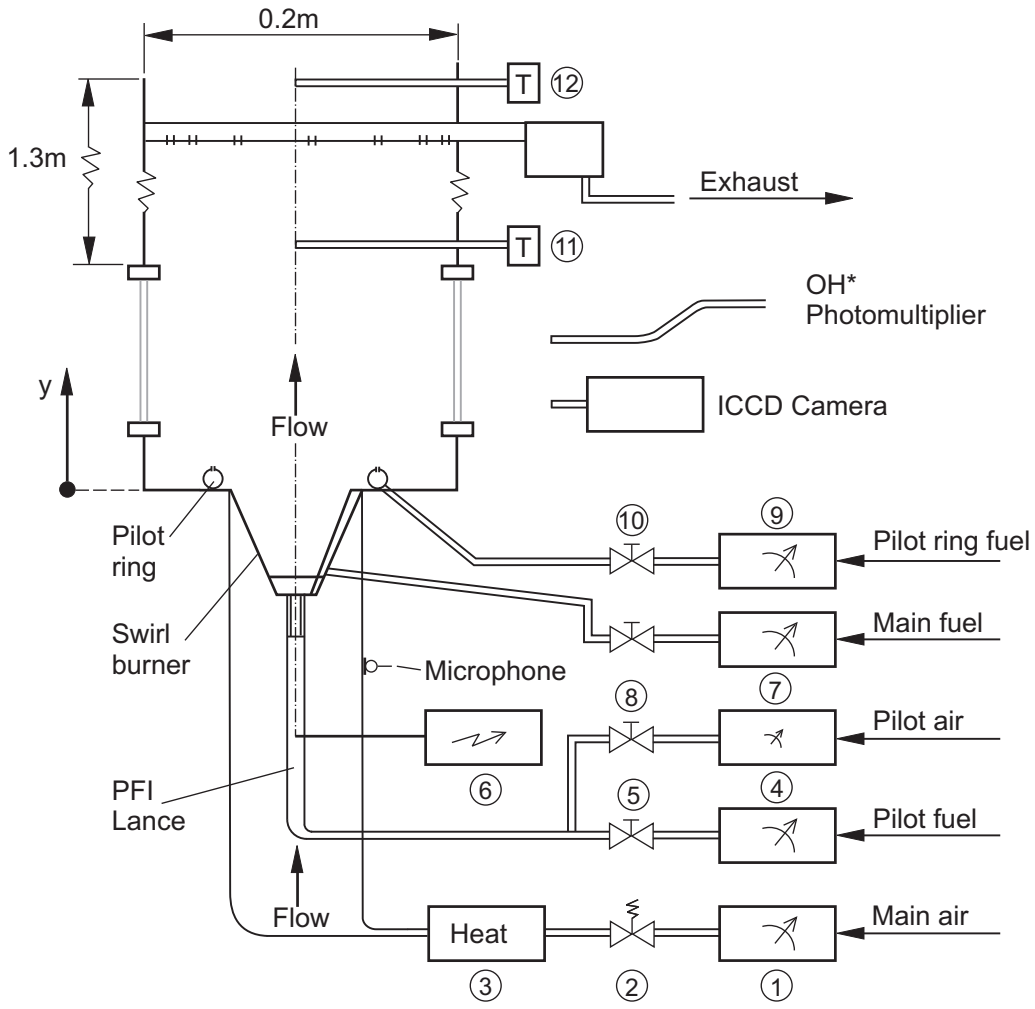

Figure 5.1: Testrig setup for the experimental investigation of instabilities and of the LBO limit. Components of the test rig: ①- Laminar Flow Element (LFE); ②- Pneumatic slide valve; ③- Air preheater; ④ + ⑦- Coriolis massmeter; ⑤ + ⑧ + ⑩- Needle valve; ⑥- High voltage ignition system; ⑨ Rotameter; ⑪ + ⑫- K-type thermocouple for bottom and exit exhaust temperature; ⑬- Condenser microphone.

measurement are discussed in more detail in the following section.

5.1 Pilot flame injector (PFI)

The principle of the continuous pilot flame generation is shown in Fig. 5.2 where the side view of the swirl burner equipped with the PFI is shown. The PFI exit plane with 17 mm in diameter is located $1-2$ cm above the apex of the swirl burner. Fuel and air were mixed approximately 1.5 m before being led into the 1.2 m long PFI-tube, so that a homogeneous mixture could be assumed at the PFI outlet. While the main part of the fuel/air mixture (bypass flow) is led through the annular gap between the ceramic tube ③ and the inner PFI tube, a small part is forced through a perforated plate into the ceramic tube. If the spark plug ① is activated, the mixture inside of the ceramic tube can be easily ignited as only low flow velocities exist. The ignited pocket of fuel/air mixture propagates further downstream

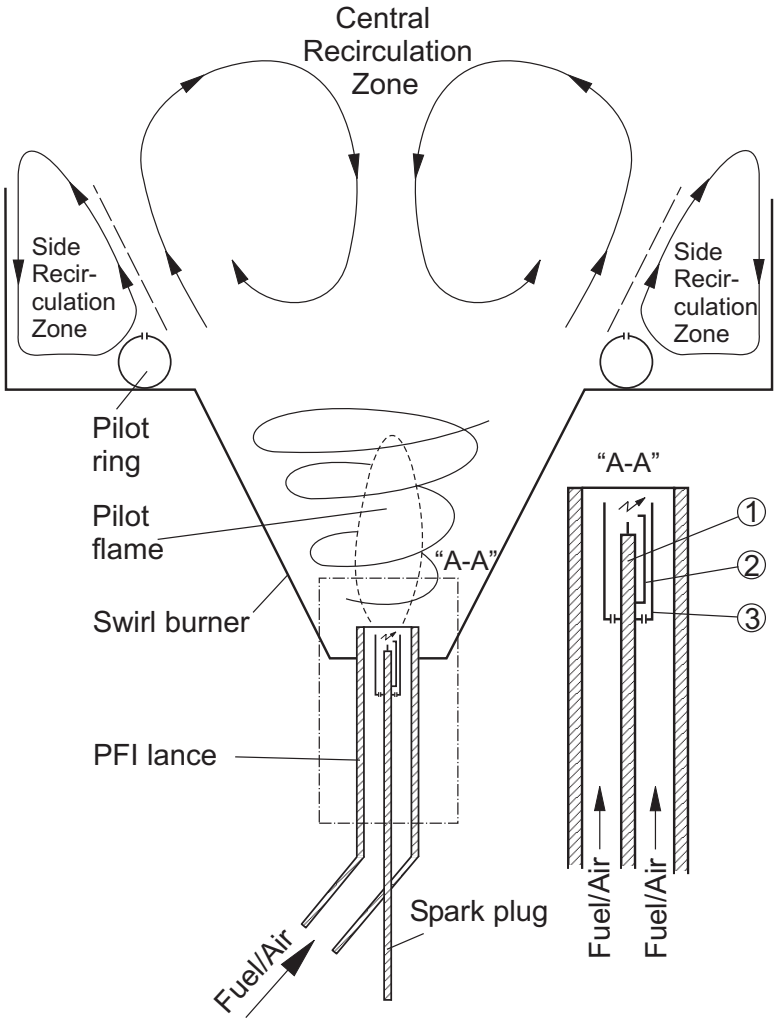

Figure 5.2: Location of the pilot injection: Pilot ring and Pilot-flame-Injector (PFI). The PFI-lance consists of: ① spark plug; ② the grounded electrode and ③ a ceramic tube with reduced diameter further upstream to reduce the velocity of the mixture. Moreover, the ceramic tube prevents a discharge into the PFI tube that could harm the measurement devices.

and then ignites parts of the bypass flow, so that a pulsed premix pilot flame can be anchored at the upper side of the ceramic tube. To prevent flashbacks into the PFI-tube, a fuel/air mixture mass flow rate of at least 3 kg/h has to be setup. The main components for spark generation are the spark plug and the high voltage generation device that are discussed in more detail in the following section.

5.1.1 Spark plug

The spark plug was made in-house as no commercial spark plug could fullfill the geometry requirements of 1.2 m length and 5 mm diameter. It consists of a ceramic tube with two 1.2 mm holes where two electrodes (made of iron wire) were drawn through. At both ends,

the hole openings for the grounded electrode were extended in the axial direction of around 35 mm, to increase the distance to the positive electrode and to prevent discharge at these positions (Fig. 5.2).

5.1.2 High voltage generation device

The high voltage generation device was designed in-house after several tests with different commercial devices failed to ignite the fuel/air mixture periodically. It is assumed that these devices interacted strongly with the in-house spark plug that is 1200 mm in length and is not equipped with optimized resistors. To circumvent this disadvantage, the in-house system was equipped with a frequency synthesizer (FS), the pulse generation unit ($MC1428B$), a switchdriver OPA, a fast relay ($MOS-FET$) and a spark coil (Fig. 5.3). The FS produces

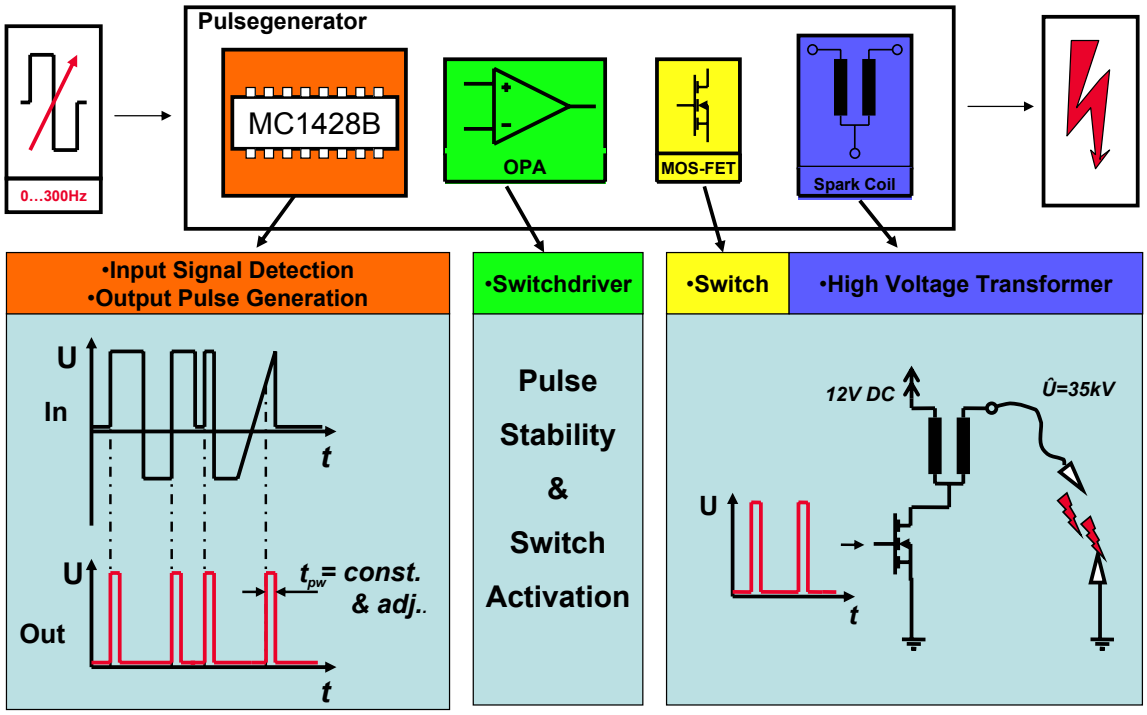

Figure 5.3: Principle of the high voltage generation.

a low volt-TTL-signal, while the pulse generation unit (PGU) and the switchdriver optimize, invert and amplify the signal before it is sent to the fast relay. Between FS and the PGU, an optoelectronic coupler (not shown in Fig. 5.3) is used to reduce the high voltage pulses between the low voltage - and the high voltage circuit. The fast relay is able to interrupt the prime circuit of the spark coil if a TTL-voltage signal is available. At each switch, a high current is passed temporarily through the primary coil that induces an approximately 30 kV voltage peak in the secondary coil [95].

5.1.3 Electromagnetic shielding concept

Preliminary tests with the spark plug and the ignition device showed a significant influence on the measurement equipment. Several causes are responsible for this behavior [95]:

1. **Galvanic coupling:** The meaning of Galvanic coupling is the direct connection (wire) of two different circuits that are influenced by each other. Interactions can happen if the AC voltage at the connection location does not match with the other one e.g. different resistances within each circuit.

2. **Inductive coupling:** This kind of coupling exist especially between two circuits that are located close together. If the current is oscillating then a voltage can be induced within the other one.

3. **Radiation coupling:** Radiation coupling occurs between two circuits if the distance between two electrical lines of each circuit exceeds the shortest emitted electro-magnetic wavelength. Under these conditions, a broad frequency band is emitted by the circuit, especially from high voltage circuit, that induces an AC voltage in the other circuit.

A shielding concept presented in Fig. 5.4 was applied on the high voltage circuit to suppress the coupling mechanisms. To disconnect completely the low and high voltage circuit from each other, the electrical power for the high voltage circuit is provided by a car battery. The disconnection between the frequency synthesizer and the pulse generator could be realized by an optoelectronic coupler. Moreover, the high voltage circuit was completely shielded by using grounded metal hoses and grounded metal boxes to reduce both the inductive coupling and the radiation coupling. To quantify the electromagnetic radiation with and without shielding,

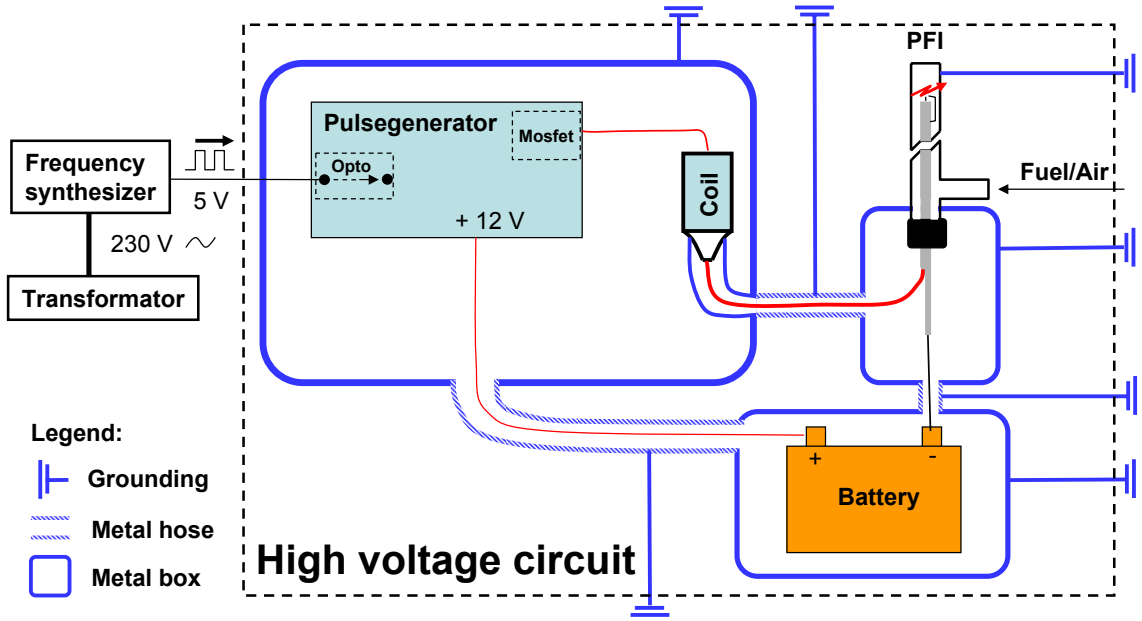

Figure 5.4: Shielding concept for electro-magnetic waves: The high voltage circuit is completely disconnected (no galvanic connections) by using a car battery and an optoelectronic coupler (Opto). Inductive coupling and radiation coupling could be reduced by using grounded metal hoses and grounded metal boxes.

a linear wire antenna, 0.1 m length and an oscilloscope (resolution: 50 ns, 20 MHz, DSO 3350 Krenz Electronics) was used. The antenna was located in front of the high voltage circuit in a distance of $\approx$ 0.5 m while the spark plug was operated with a spark frequency of 110 Hz. The test case with shielding was conducted with the setup presented in Fig. 5.4 while for the test without shielding, all grounded metal boxes and grounded metal hoses were

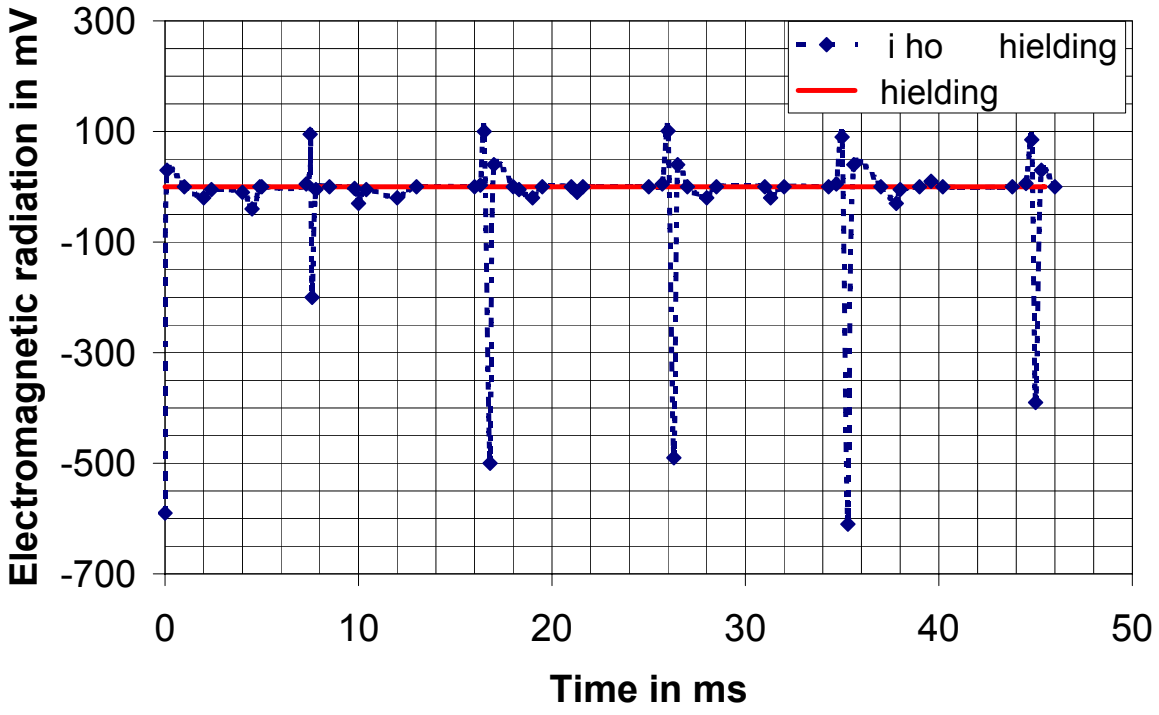

Figure 5.5: Radiation of the high voltage circuit and the spark with and without shielding (Ref. [95]).

removed. Before the tests were started, the oscilloscope was also protected by a grounded, finely woven fence that was positioned between the high voltage circuit and the oscilloscope. Preliminary tests at the department of high frequency technique (TU Berlin) have shown that the high voltage circuit emits electromagnetic waves within a frequency range of 0.001-20 MHz [95]. The frequencies with the highest amplitudes were located close to the 20 MHz limit. To detect frequencies at the higher level, the linear wire antenna with a 0.1 m length was designed for an optimal frequency of 1.5 MHz or for a 0.2 m wavelength to get a moderate sensitivity characteristic in both directions (from 1.5 MHz to 0.001 MHz and from 1.5 MHz to 20 MHz). The reduction of the radiation with shielding can be clearly seen in Fig. 5.5 when compared with the non-shielded case. Nevertheless, the disturbance of very sensitive devices e.g. the ICCD camera or the closed loop controller could not be completely suppressed by this shielding concept. However, the disturbance level was very low so that the devices could be operated without any problems. For future work, a further reduction of the disturbance could be achieved if the grounding for the metal hoses and metal boxes is improved, i.e. by increasing the diameter of the grounded wires and by increasing the number of the grounding positions. Moreover, the optoelectronic coupler should be replaced by a laser to increase the distance between the high voltage circuit and the low voltage circuit. Currently, it is integrated within the grounded metal box so that disturbances can be transmitted by inductive coupling into the frequency synthesizer.

5.1.4 Operating range

The operating range depends strongly on the PFI-outlet geometry, as it can be seen in Fig. 5.6, where the rich and lean blowout limit are presented for each investigated case. The tests were

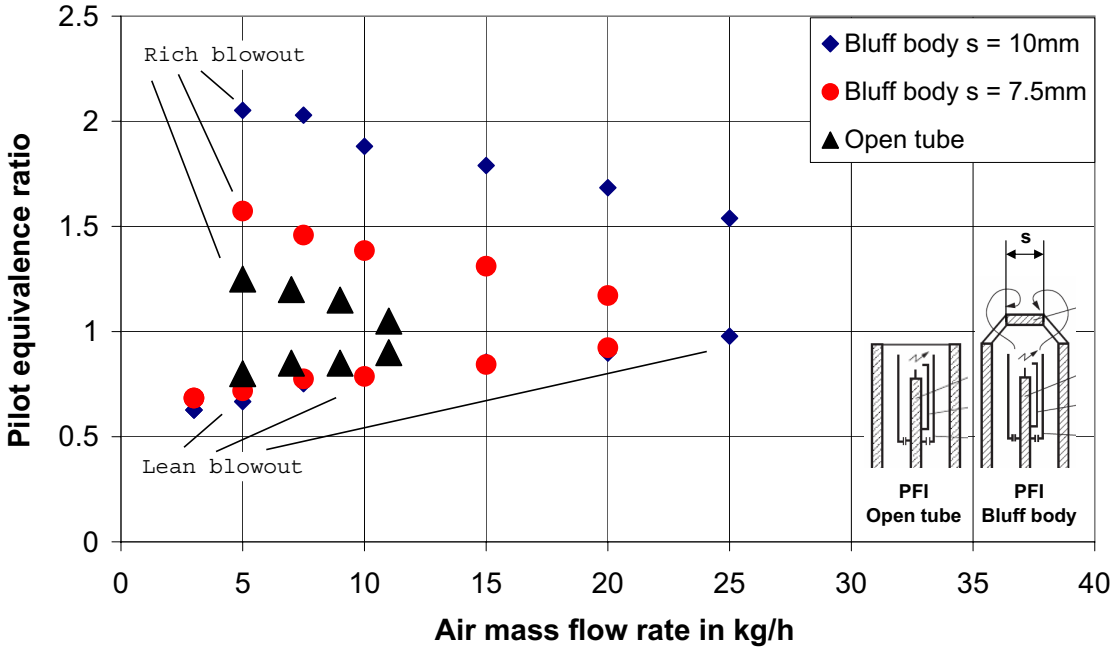

Figure 5.6: Rich and lean blowout limits of the PFI with different outlet geometries.

conducted at a constant spark frequency of 110 Hz under ambient conditions while the PFI outlet geometry and the pilot air mass flow rate were varied. The PFI with an open tube geometry is only able to periodically generate ignited pilot flames until approximately 11 kg/h pilot air mass flow rate. At higher pilot air mass flow rates, only the pilot mixture through the ceramic tube can be further ignited, but the pilot mixture through the annular gap is left unburnt the PFI. To reduce the spark frequency and to extend the PFI operating range, bluff bodies with different diameters 7.5 mm and 10 mm were mounted at the exit of the PFI tube. The bluff bodies were manufactured from alloy and feature three stiff but flexible wire legs each. The legs pushed outward against the inside wall of the PFI tube and allowed the bluff body to be positioned at various heights above the apex of the lance. Preliminary tests showed that the flame was steadiest and most symmetrical when the disc was positioned approximately 1 cm downstream of the PFI-tube. All of the tests described hereon use that distance accordingly. In contrast to the PFI lance with open tube, 110 Hz were set only at the very beginning of the tests when the pilot premixed flame has to be ignited. Afterwards, the spark plug frequency could be reduced to 5 Hz as the pilot flame could be anchored at the bluff body top. Different pilot air mass flow rates in the range from 3 kg/h to 30 kg/h were set while Φ_{Pilot} was varied between 0.5 and 3.0 for each mass flow rate. Pilot premix flames at $\Phi < 0.5$ or $\Phi > 3.0$ could only be generated at pilot air mass flow rates lower than 3 kg/h. In comparison to the PFI with open end, the operating range could be significant extended for both bluff body diameters, as it can be seen in Fig. 5.6. Obviously, the generated recirculation zone at the bluff body top improves the stabilization of the premixed pilot flame at higher air mass flow rates. While the operating range of the "bluff body $s = 7.5$ mm" is very small at 20 kg/h pilot air mass flow rate, the "bluff body $s = 10$ mm" case shows a $\Delta\Phi \approx 0.5$ even at $\dot{m}_{Pilot} = 25$ kg/h. The reason for the $\Delta\Phi$ difference can be found in an higher pilot rich blowout limit with the "bluff body $s = 10$ mm" case at pilot air mass flow rates higher than 3 kg/h , while the pilot lean blowout remains nearly similar in both cases. It should also be

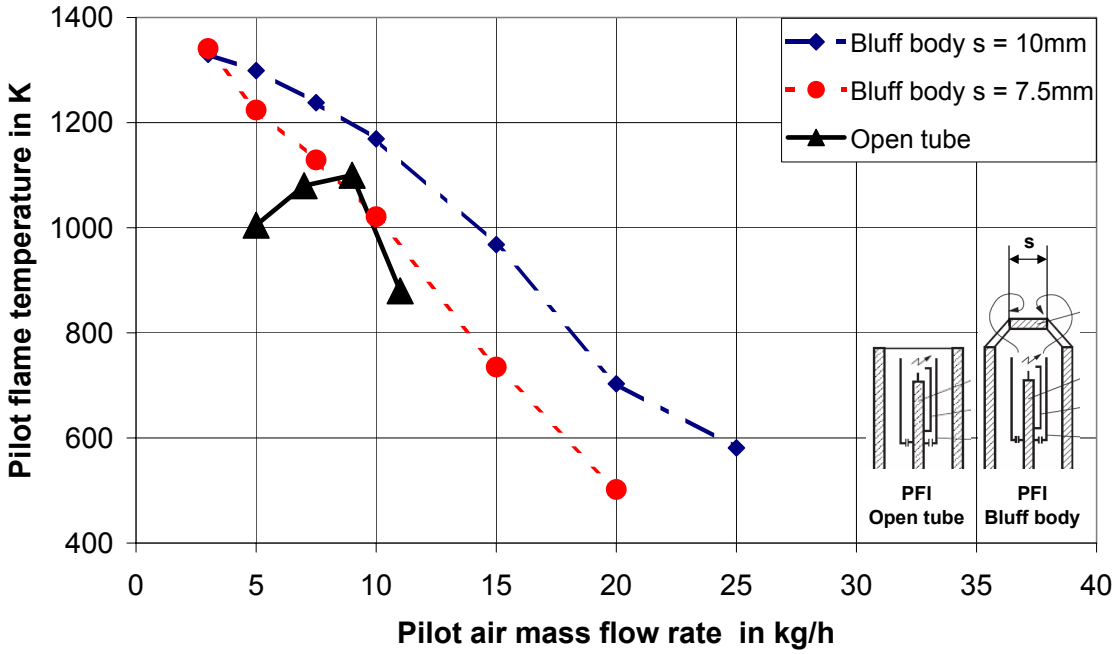

Figure 5.7: Averaged pilot flame temperatures for different PFI outlet geometries and at a constant $\Phi_{Pilot} = 1.1$.

noted that no rich blowout limit was reached for either the bluff bodies at the air mass flow rate of 3 kg/h. Furthermore, pilot flames could be generated up to 23 kg/h for the "bluff body $s = 7.5$ mm" and up to 28 kg/h for the "bluff body $s = 10$ mm" but were not plotted into the diagram as the lean and rich blowout limits could not be identified anymore. The average flame temperature of the pilot premix flame was recorded for different pilot air mass flow rates. A thermocouple k-type with a diameter of 1.5 mm was located approximately 0.14 m downstream of the PFI outlet. All operating points are recorded at $\Phi_{Pilot} = 1.1$ that represent the best ignition condition for the fuel/air mixture. It can be seen in Fig. 5.7 that the flame temperature continuously decreases with increased pilot air mass flow rates for both bluff body diameters. The curve of the "bluff body $s = 10$ mm" case decreases moderately and achieves the lowest temperature of ≈ 600 K for an pilot air mass flow rate of 25 kg/h while this temperature level is achieved already at $\dot{m}_{Pilot} = 17$ kg/h for the "bluff body $s = 7.5$ mm" case. Note, the highest measured temperature of 1300 K is relatively low compared with the adiabatic flame temperature at the same $\Phi_{Pilot} = 1.1$ and might indicate incomplete combustion. The PFI operation is limited by the flame temperature and by the pilot mass flow rates. While averaged flame temperatures lower than the self-ignition temperature of 870 K might not able to sustain efficiently the main premix flame, high pilot air mass flow rates might disturb the vortex breakdown and could destabilize it. In preliminary tests it was observed that the main premixed flame can be sustained very efficient when the premixed pilot flame is operated between $7.5 - 15$ kg/h pilot air at $\Phi_{Pilot} = 1.1$. It can be summarized that the best operating conditions for open tube PFI can be found at 7.5 kg/h pilot air mass flow rate and 110 Hz spark frequency. These conditions were also set for the "rich mixture (RM)" boundary control (section 6.3). The operating range can be varied under these conditions between $\Phi_{Pilot} = 0.8 - 1.2$ and the averaged flame temperature is nearly 1100 K for $\Phi = 1.1$. The best operating range for the bluff body geometries could be detected between 5 kg/h and 15 kg/h for the "bluff body $s = 10$ mm" case. Therefore, this configuration was used for the

"lean mixture" boundary control as compact pilot premix flames with a sufficient averaged flame temperature of ≈ 1200 K could be guaranteed.

5.2 Pilot ring (PR)

The pilot ring with a 110 mm diameter consists of a stainless steel tube that was mounted on the combustor dump (see Fig. 5.2). The 6 mm diameter tube was equipped with nine equidistant distributed boreholes, each of 1 mm diameter. All boreholes are directed in the axial direction respectively in direction of the coordinate y defined in Fig. 5.1, so that the pilot ring mass flow can be injected well into the shear layer of the two recirculation zones.

Chapter 6

Experimental results

The experimental results of different control concepts for the combustion region 3 mentioned in section 2 are presented in the following chapter. Several parameter definitions will be described in section 6.1 while the results of the "lean mixture (LM)" and "rich mixture (RM)" boundary extension of region 3 are presented in sections 6.2-6.4.

6.1 Parameter definitions

The combustion behavior within the region 3 (see section 2) has been characterized by different parameters in this study, especially the boundaries of this region have to be precisely defined before its range can be evaluated with and without control methods. While at leaner mixtures, the flame front can often be characterized by a lift-off flame front that leads to inefficient combustion. The flame front at richer mixtures can change to an oscillating flame with higher amplitude of pressure oscillations. Based on these assumptions, the following parameters can be derived for the boundaries definitions:

1. **"Lean mixture (LM)" boundary:**
   The "LM" boundary can be specified at Φ_{Total} for each case where the CO emissions first exceed the 1 ppm level and is referred as $\Phi^*_{CO<1}$.

2. **"Rich mixture (RM)" boundary**
   The "RM" boundary is defined at Φ_{Total} when a dominant peak of the fundamental frequency exceeds the background noise level measured at $\Phi^*_{CO<1}$ by the factor of 2.

Both boundaries are presented in two example charts shown in Fig. 6.1 for the cases baseline (without pilot injection) and for the diffusion pilot (pilot fuel injection). According to the definition above, the "LM" boundary (left chart in Fig. 6.1) for the baseline case can be defined at $\Phi_{Total} \approx 0.46$, for the diffusion pilot at $\Phi_{Total} \approx 0.45$. At leaner Φ_{Total}, the CO emissions exceed the 1 ppm limit. Even though the "LM" boundary of the diffusion pilot can be defined at a leaner mixture, the NO_x emissions are significantly higher. To visualize the "RM" boundary, the pulsation level for both cases are represented in Fig. 6.1 (right chart). The pulsation level increases rapidly and exceeds the background noise by a factor of two at 2 % (Baseline) and 3 % (Diffusion pilot) of the normalized Φ_{Total}. The parameters used in the example charts and in this study are summarized further below:

1. **Definition of $\Phi^*_{CO<1}$:**
   $\Phi^*_{CO<1}$ represents the "LM" boundary of region 3 and was defined at Φ_{Total} where the

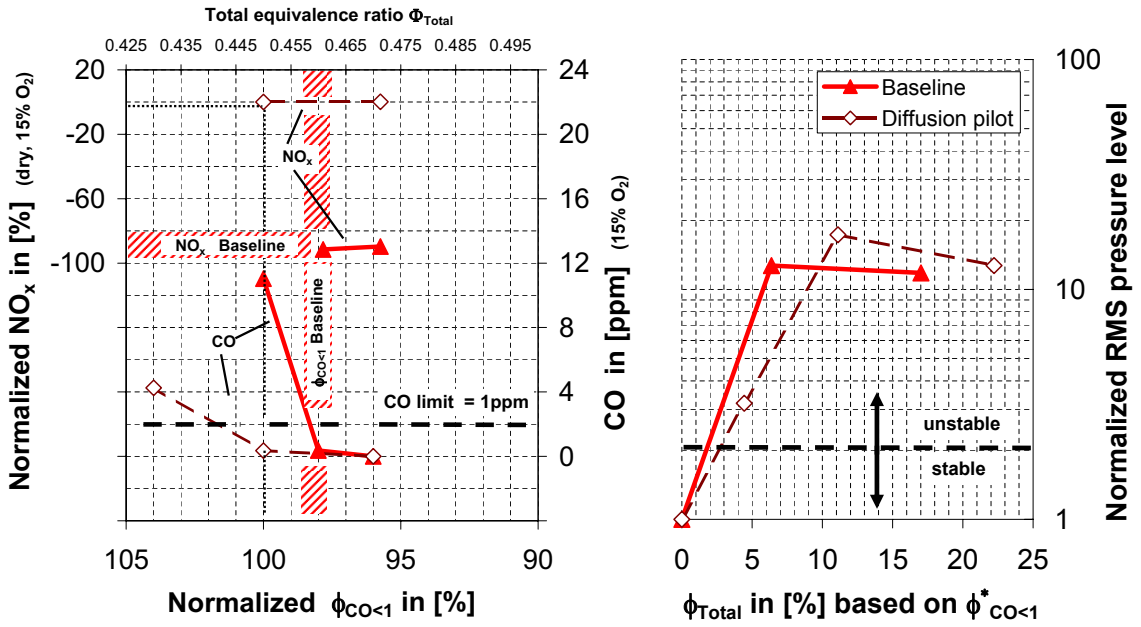

Figure 6.1: Example chart for the boundary definition of region 3. The lean mixture boundary (left chart) is achieved at Φ_{Total} where the CO emissions exceed the 1 ppm limit. The rich mixture boundary (right chart) is defined at Φ_{Total} where the pulsation level exceeds the background noise level by the factor of 2. The tests were conducted at 550 K preheat temperature and with a 200 mm combustor tube.

combustion efficiency of the main combustion starts to decrease. A good indicator for it is the CO emissions that rapidly increase during inefficient combustion. Therefore, the limit was set at the corresponding Φ_{Total} where the CO emissions first exceed the 1 ppm level and is referred as $\Phi^*_{CO<1}$.

2. **Definition of normalized $\Phi_{CO<1}$:**
   Normalized $\Phi_{CO<1}$ represents a normalized Φ_{Total} based on an operating point of the diffusion pilot case where CO emission first exceed the 1 ppm limit:

$$\Phi_{CO<1} = 100\% + (1 - (\frac{\Phi_{Total}}{\Phi^*_{diff,CO<1}}) \cdot 100\%). \tag{6.1}$$

   The suffix "diff" in $\Phi^*_{diff,CO<1}$ refers to diffusion pilot. The definition was introduced to easily quantify the "LM" boundary extension behavior of the proposed premixed pilot when compared to the conventional diffusion pilot. Fig. 6.1, left chart, presents an example where the "LM" boundary of the diffusion pilot is defined at 100 % while the baseline case is less effective and achieves $98 - 99$ % of the diffusion pilot boundary.

3. **Definition of Ω_{Range} respectively Φ_{Total} in [%] based on $\Phi^*_{CO<1}$:**
   To quantify the range of region 3 for each case, each operating point Φ_{Total} was first normalized on its own "LM" boundary $\Phi^*_{CO<1}$, e.g. Φ_{Total} of the baseline case was based on $\Phi^*_{base,CO<1}$, Φ_{Total} of the diffusion pilot was based on $\Phi^*_{diff,CO<1}$ etc. The parameter is referred to as Ω_{Range} and allows the expression of the "RM" boundary in % of the "LM" boundary for each case:

$$\Omega_{Range} = (\frac{\Phi_{Total}}{\Phi^*_{CO<1}} - 1) \cdot 100\% \tag{6.2}$$

Fig. 6.1, right chart, presents an example where both cases show only a small stable region in % of the "LM" boundary $\Phi^*_{CO<1}$.

4. **Normalized Root Mean Square (RMS) pressure level:**
The level of pressure fluctuations are expressed by the RMS pressure level that was normalized on the pulsation level at $\Phi^*_{CO<1}$.

5. **Normalized NO_x emissions:**
The NO_x emissions were normalized on a NO_x value that was measured at the following conditions:(1) at activated diffusion pilot and (2) at Φ_{Total} where CO emissions firstly exceed the 1 ppmv limit (e.g. Fig. 6.1, left). The percentage of the normalized NO_x emissions is defined according the following formula:

$$NO_{x,norm} = \frac{100\% \cdot NO_{x,meas}}{NO_{x,norm}} - 100\% \tag{6.3}$$

Currently, the diffusion pilot case represents the state of the art injection method for local extinction and instability control and can be used as a reference control method to validate the NO_x emissions of the proposed premixed injection cases in this study.

6.2 Control concepts for the "lean mixture (LM)" boundary

Different control concepts for the "Lean Mixture (LM)" boundary were proposed in this study to extend the operating range (region 3, Fig. 2.1) to leaner operating points. In general, the flammability limits of hydrocarbon-air mixtures can be influenced by the inlet pressure and the inlet preheat temperature. While the upper flammable limit or rich limit is strongly influenced by the pressure, the lean limit is less pressure-dependent within the range from 10 kPa to 5000 kPa. An increase in temperature will also widen the flammability limits but with reduced impact when compared to pressure increase. In Fig. 6.2, the lean limits of the EV-10 burner for different boundary conditions are shown and confirm the influence of the preheat temperature [3]. The tests were conducted at two different mass flow rates (200 kg/h, 300 kg/h), different preheat temperatures (373 K, 523 K) and two different combustion tube lengths. The 500 mm tube length is referred in the figure as "no tube" and the 1400 mm tube length as "tube". Note, the thermal power on the vertical axis is calculated from the sum of the combustion heat release. It is proportional to the fuel flow rate and the thermal energy of the combustion air and depends on the preheating temperature and the air mass flow rate. It can be concluded that Φ_{LBO} decreases with increasing preheat temperature and increases with increasing flow velocity (proportional to the air mass flow rate). It is interesting to note that similar conclusions can be drawn from experiments with buff-body flame holders [10]. The parameter inlet temperature and flow velocity were varied between 300 K and 600 K and 10 m/s and 100 m/s, respectively to investigate closer the effect on the lean limit. For the tests, a homogeneous mixture of gaseous propane and air was chosen. Depending on the inlet temperature, the lean limit occurs at equivalence ratios from 0.36 to 0.60 measured at velocity of 50 m/s and a ratio of the flameholder cross-sectional area to that of the pipe of 0.25. For the EV-10 burner, the lean limits are found to be in the range of $\Phi_{Total} = 0.39$ and $\Phi_{Total} = 0.47$. Note, the limits represents the real flame blowouts so that operating points shortly before these points are already completely insufficient in terms of combustion efficiency and can be characterized by high formation of CO. At the tests with

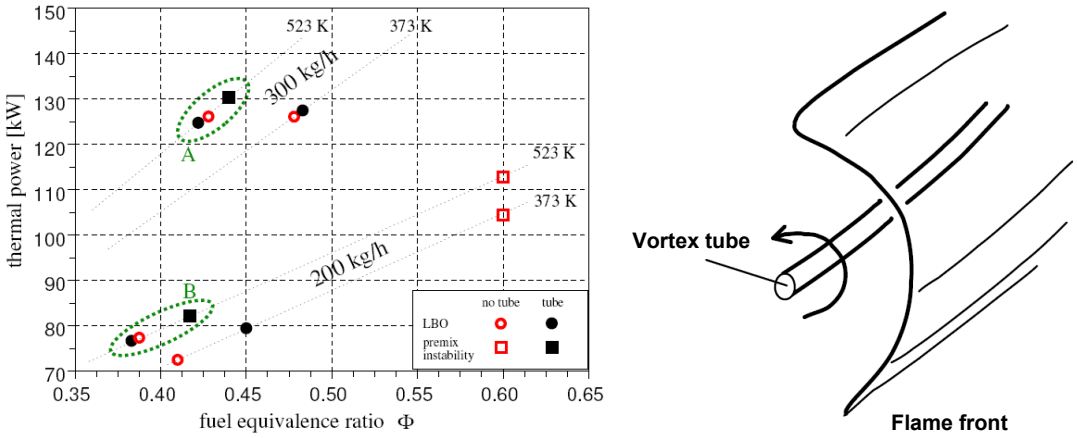

Figure 6.2: Lean limits of the EV-10 burner for different mass flow rates and preheat temperatures (left). Quenched local flame fronts might occur near vortex tubes with high strain rates according to [8].

the EV-10, CO concentrations within the exhaust could be measured up to several thousend ppmv shortly before lean blowout occured. This is also the reason why the leanest operating point with less than 1 ppmv CO emissions is located at much higher equivalence ratios as e.g. in Fig. 6.4 and Fig. 6.5 are shown. In other premixed combustion systems, typical lean limits correspond to an equivalence ratio of around 0.5 [53, 47, 92]. The cause for flame blowout might be found in an insufficient heat release rate within the combustion zone that is not able to heat up the fresh mixture to the required reaction temperature. To prevent such an event and to extend the operating range without efficiency losses, a high radical pool at the lower stagnation point of the central recirculation zone, shown in Fig. 5.2, has to be guaranteed [34]. Pilot flames are especially suitable to compensate for the low concentration of radicals in that region when Φ_{Total} is decreased. Thereby, local quenched flame fronts, responsible for inefficient combustion, might be prevented. These regions were identified in [21] by a OH^* laser-induced fluorescence (OH^*-LIF) measurement technique when the OH^* concentration was measured within the flame front of a EV-10 swirl burner. Thereby, local quenched flame fronts were defined if no OH^* radical signal was detected. It is assumed in [20] that the chemical reaction within these regions is suppressed by so-called vortex tubes with high strain rates (see Fig. 6.2, right sketch).

Different combustion tube outlet diameters of 65 mm and of 200 mm were chosen to evaluate the control concepts with and without low-frequency pulsation (delayed flame lift-off) at the lean blowout that can be also detected in real gas turbines. Note, these pulsations are not generated by an interaction between heat release rate fluctuation and pressure fluctuation but by combustable mixture kernels that ignite spontaneously at hot walls or in hot temperature regions. Thereby, low-frequency pulsations of $1 - 5$ Hz with high amplitudes and increasing CO emissions can be measured, as in the case of the "65 mm". The observed flame fronts are visualized for different combustion conditions in Fig. 6.3 where the RMS pressure level versus Φ_{Total} is shown. It is interesting to note that both observed flame front structures near lean blowout for the tube diameters "65 mm" and "200 mm" show reduced p'. While reduced p' for the "200 mm" case might be traced back to a local heat release rate that is not sufficient for p' excitations, the time delays for the "65 mm" case seems to be completely

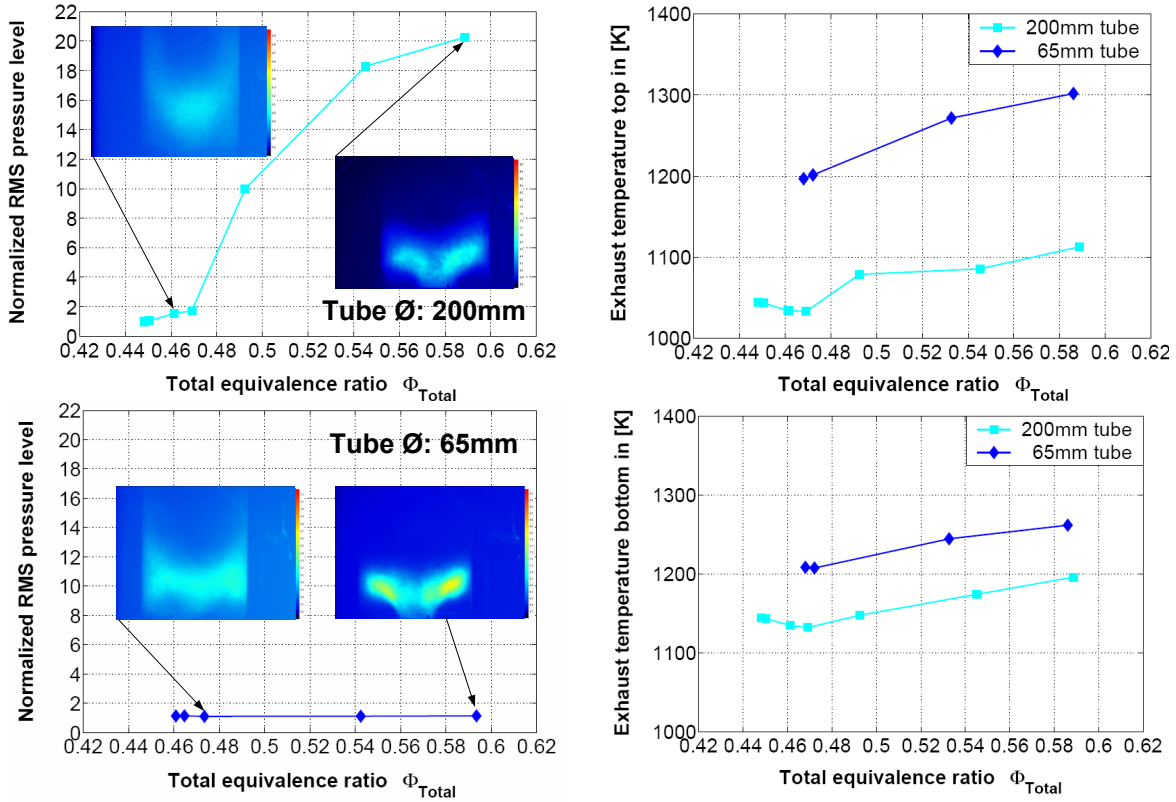

Figure 6.3: Observed flame front structures for a 65 mm and for a 200 mm tube outlet diameter.

out of the range of the critical frequency of the combustion system (see explanation model in section 6.3.4). It is not fully understood why different flame front structures occur near LBO when different tube outlet diameters are chosen. One possible explanation could be a higher residence time of hot gases within the combustion chamber and would also explain the higher exhaust temperatures for the "65 mm" case shown in Fig. 6.3. The exhaust temperatures were measured at a distance from the burner exit plane of roughly 500 mm and 1300 mm and are referred to as "exhaust temperature bottom" and "exhaust temperature top". An increased mass flow rate of hot gases into the primary zone could be another parameter that is able to shorten the time delay between fuel injection and ignition and to suppress the typical flame structure near lean blowout shown by the "200 mm" case. To prove this assumption, further tests are necessary e.g. a visualization of the flowfield for both tube diameters using e.g. the PIV (Particle Image Velocimetry) measurement technique in a water tunnel.

6.2.1 Test cases

A parametric study has been conducted to find out the most efficient premixed pilot configuration for achieving the leanest operating point without efficiency losses and an increase in NO_x emissions. The pilot mass flow rates through the PFI lance and the pilot ring were varied while the main air mass flow rate was kept constant at 200 kg/h. Moreover, the tests were done at main air preheat temperatures of 300 K and 550 K and the combustion tube outlet diameter was set at 65 mm and at 200 mm. In table 6.1, only the most efficient cases are summarized while other investigated cases are shifted into the Appendix A. To identify the cases, a code was given where the first two numbers represent the PFI-air and PFI-fuel in

kg/h and the last two numbers represent the pilot ring air and fuel in kg/h. The same code was applied for the baseline case “1 0 0 0” and for the diffusion pilot cases “0 0.48 0 0” and “0 0.96 0 0”. The baseline case could not be operated without a small amount of cooling N_2 through the PFI lance otherwise the integrated spark plug would have been damaged by the heat radiation produced by the main flame. The spark plug was only activated during the tests with premixed pilot injection and was operated at a constant frequency of 110 Hz. The

Table 6.1: Most efficient premixed pilot configurations for achieving the leanest operating point (“lean mixture” boundary) described in section 2.

Cases	**Temp.**[1]	**Diam.**[2]	**PFI air**	**PFI fuel**	**PR air**	**PR fuel**
−−	**K**	**mm**	**kg/h**	**kg/h**	**kg/h**	**kg/h**
“PFI-cold”	300	200	7.5	0.48	−−	−−
“PFI-hot”	550	200	15	0.96	−−	−−
“PFI-Ring”	550	65	10	0.65	0	0.96

emissions were recorded first when the emission concentration of CO, NO_x did not vary more than 0.2 ppm within 5 min. The procedure was chosen as the main flame is prone to lift-off at the “LM” boundary and might disturb significantly the equilibrium between the heat release of the combustion and the heat transfer at the inner wall. Thereby, the material temperature of the burner and the radical concentration near the lower stagnation point decreases due to the lift-off flame.

6.2.2 Delayed flame lift-off

By using the conventional diffusion pilot or the premixed pilot, the “LM” boundary could be successfully shifted to lower equivalence ratios without efficiency losses when compared to the baseline case (Fig. 6.4). It also corresponds with a delayed main flame lift-off and defines the “LM” boundary. The premixed pilots, referred as “PFI-cold” (7.5 0.48 0 0) and “PFI-hot”

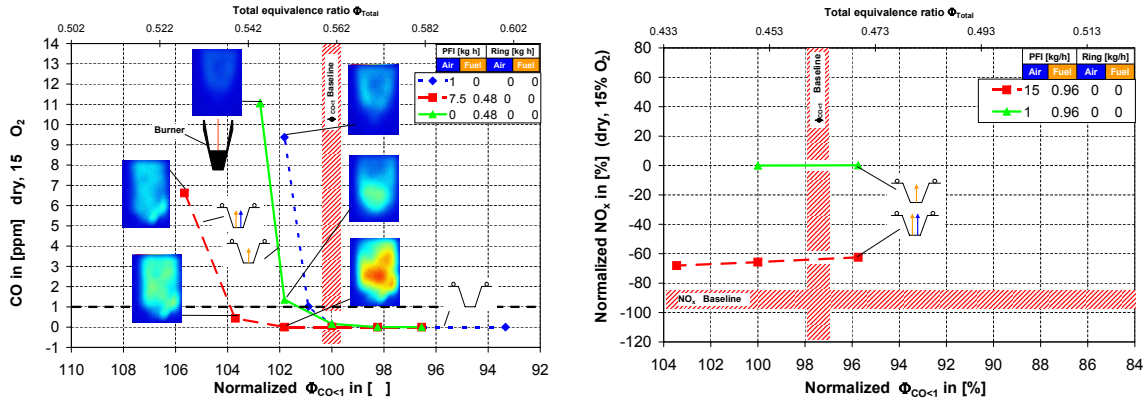

Figure 6.4: Delayed lift-off flames for a 200 mm tube diameter test set up at main air temperatures of 300 K (left) and 550 K (right).

(15 0.96 0 0) are able to delay the main flame lift-off more efficiently than the diffusion pilot.

[1] Preheat temperature
[2] Tube diameter

Moreover, the NO_x emission held at an acceptably low level as it can be seen for the preheated test case shown in Fig. 6.4, right chart. The NO_x emissions of the "PFI-cold", the diffusion pilot (1 0.48 0 0) and the baseline (1 0 0 0) for the 300 K non-preheated test case were not plotted as they kept of an extremely low level at approximately 1 ppm. The question arises why the PFI flame is so effective. To answer the question, OH^* images were taken at 102 % normalized $\Phi_{CO<1}$ and at a total equivalence ratio of 0.55 (Fig. 6.4, left chart). A lift-off main flame could be detected for the baseline and the diffusion pilot that corresponds to the typical flame front of region 2 (compare Fig. 2.1). The highest OH^* density was detected for the premixed pilot case that is also characterized by the smallest distance between the flame front and combustor dump. This seems to be the reason why the flame lift-off for premixed pilot could be prevented more effectively when compared to the diffusion pilot. For preheat temperature of 550 K (Fig. 6.4, right), the LM boundary of the premixed pilot case could be shifted up to 4 % when compared to diffusion pilot case. The NO_x emissions kept at nearly the same level at -70 % of the diffusion case. The CO emissions, O_2, and the exhaust temperature at different operating conditions are presented in appendix A and show a typical behavior at decreasing Φ_{Total}. Other premixed pilot configurations, but ineffective in terms of delaying the flame lift-off process are discussed in the appendix A.

6.2.3 Delayed low-frequency pulsation

For the "65 mm" tube diameter, the typical low-frequency pulsations that occur shortly before the lean limit, could be delayed by using the premixed pilot, case "10 0.64 0 0". The NO_x emissions could be kept at a similar level like the baseline case (Fig. 6.5). The pilot diffusion case "0 0.64 0 0" produces much higher NO_x emissions but it is able to delay the low-frequency pulsations to much leaner mixtures when compared to the preheated tests with the "200 mm" tube diameter (see Fig. 6.4). A similar delay could be achieved with the "10 0.64 0 0.96" case when 0.96 kg/h fuel is additionally injected through the pilot ring. However, the injection technique does not allow to reduce NO_x emissions. Other configurations of pilot and ring injection were tested but the advantages of this kind of fuel partition could not be confirmed when compared to the conventional diffusion pilot. The results of the parametric study are discussed in the Appendix A.

6.2.4 Conclusions

The efficiency of the premixed pilot (pilot mixture injection through the PFI-lance) for extending the operating range to leaner mixtures is strongly influenced by the location of the flame front center at the "65 mm" and "200 mm" test case. The control concept was most efficient at the "200 mm" test case and only moderately efficient for the "65 mm" when compared to the diffusion pilot (pilot fuel injection only). One viable explanation for the better results at the "200 mm" case might be the higher momentum jet of the premixed pilot that is able to provide the main flame with additional radicals further downstream of the combustor dump. For the "65 mm" case, the main flame is located closer to the combustor dump, where a higher momentum jet of the premixed pilot is not required. Instead of this, the higher jet momentum might destabilize the lower stagnation point of the central recirculation zone and the danger of local extinction increases.

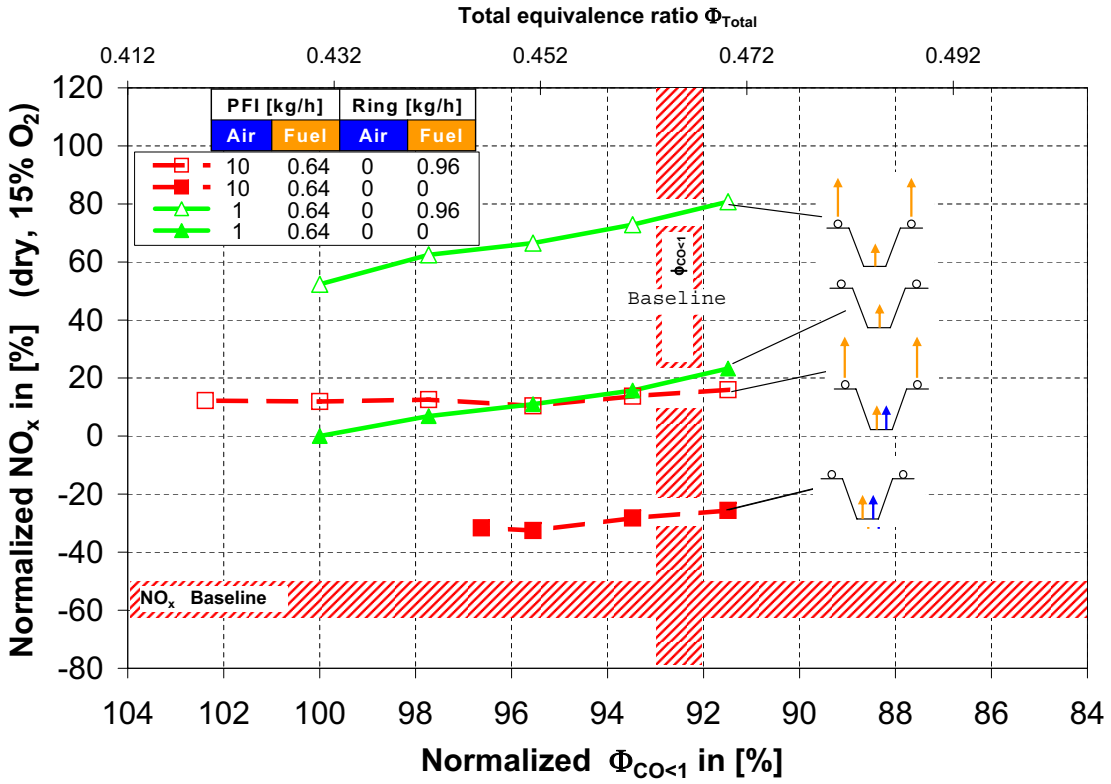

Figure 6.5: Delaying of low-frequency pulsations at a main air temperature of 550 K and for a 65 mm tube diameter test set up.

6.3 Control concepts for the "rich mixture (RM)" boundary

Three different premixed pilot injection methods were chosen to control the "RM" boundary of region 3 (see Fig. 2.1), that is characterized by a rapid increase of pressure pulsation amplitudes:

1. pilot injection through the PFI lance (premixed pilot) only,
2. pilot injection through the ring (premixed ring) only,
3. combined pilot injection through the PFI lance and ring.

The premixed pilot affects the entire heat release distribution within the combustion chamber so that the prevention of p' excitation can be mainly traced back to a change of the time delay between injection and ignition of the premixed mixture. The time delay can be influenced in two different ways; either the time delay is controlled passively or actively by the use of premixed pilot flames. In the case of the passive method, the premixed pilot flames are used to preserve an existing well-distributed main flame front in axial direction to a richer mixture that could be observed near the lean limit and corresponds with reduced p' and with a broad-band time delay range. For the active method, the main flame front location at already unstable operating points are controlled by the use of premixed pilot flames and corresponds directly with a change of the time delays. The results of the most efficient cases are discussed in the following section.

6.3.1 Test cases

Six different test cases (shown in table 6.2) were selected to show the essential impact of pilot premixed injection on the RMS pressure level and on the NO_x emissions. Other test cases are listed and discussed in Appendix C.
For the pilot injection cases "PFI-300K" and "PFI-550K", the pilot mass flow was only injected

Table 6.2: Investigated cases for delaying the "rich mixture" boundary at 550 K preheat temperature and at a tube diameter of 200 mm.

Cases	**Preheat temp.**	**PFI air**	**PFI fuel**	**PR air**	**PR fuel**
−−	**K**	**kg/h**	**kg/h**	**kg/h**	**kg/h**
"PFI-300K"	300	7.5	0.48	−−	−−
"PFI-550K"	550	7.5	0.48	−−	−−
"Baseline"	550	1.0	0.00	0	0.00
"Premixed ring"	550	1.0	0.00	15	0.96
"Diffusion ring"	550	1.0	0.00	0	0.96
"Air ring"	550	1.0	0.00	15	0.00

through the pilot lance (combustor apex) while the spark plug was off. The pilot ring was not installed in these tests. The PFI lance remained within the combustor for the ring injection tests only, but was not used. While the pilot injection tests were conducted at two different preheat temperatures 300 K and 550 K, a constant preheat temperature of 550 K was set for the ring injection and the combined injection test cases. The condenser microphone for measuring the pressure fluctuations was mounted 40 cm upstream of the combustor dump for all test cases (compare Fig. 5.1).

6.3.2 Active control of the time delay using the PFI flame

Preliminary tests were performed to prove the capability of the premixed pilot (using the PFI lance, section 5.1) to suppress instabilities by changing the heat release distribution within the combustion chamber and the time delay between injection and ignition of the mixture. Intensive tests with the premixed pilot have shown that its effectiveness is strongly limited and could be only detected at two different test conditions that will be presented in the following section. All RMS pressure levels were normalized by the background noise of the baseline case "baseline-550K" at $\Phi_{Total} = 0.45$. The test conditions of the results presented in this section are shown in table 6.2.

Overall dynamic stability with PFI-flames

The instabilities shown for the cases "PFI-300K" and "PFI-550K" in Fig. 6.6 were completely suppressed by the presence of the premixed pilot flame. The PFI changed the heat release distribution within the flame front as shown in Fig. 6.6 and thus affected the dynamic stability. The results are consistent with the investigation in [68].

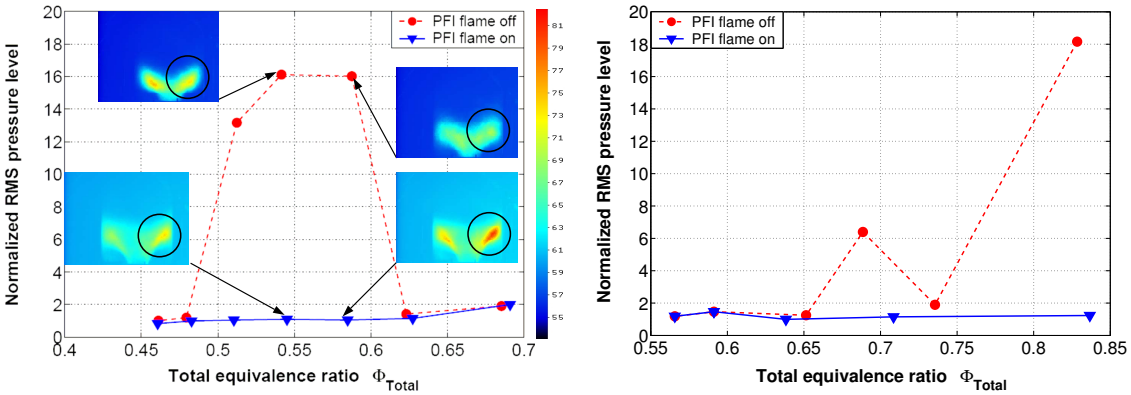

Figure 6.6: Left: RMS pressure level for the case "PFI-550K" with and without PFI flame. Right: RMS pressure level for the case "PFI-300K" with and without PFI flame. All RMS values are normalized on the background noise of the baseline case at $\Phi_{Total} = 0.45$. The PFI was equipped for both cases with a 10 mm bluff body at the outlet (see Fig. 5.6).

Response behavior for PFI flame on/off conditions

The response behavior for the PFI flame on/off conditions were investigated at selected unstable operating points of the preheated ("PFI-550K") - and of the non-preheated ("PFI-300K") case. Note, the pilot fuel/air mixture was continously injected through the PFI (no valve) while the spark plug was activated with a frequency of 110 Hz in case of "PFI flame on" conditions. The results are presented in Fig. 6.7 and Fig. 6.8. During the first 12 seconds,

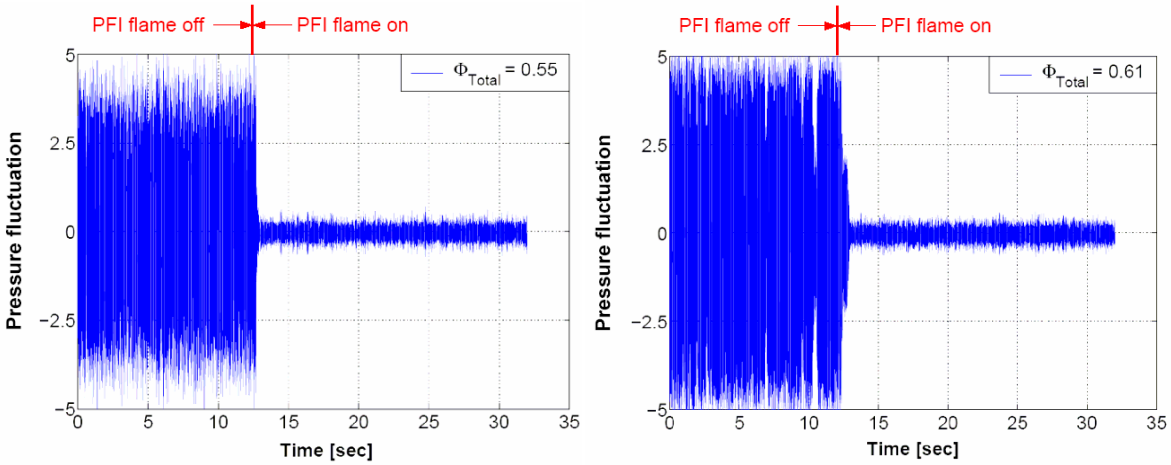

Figure 6.7: Timesignal of the pressure fluctuations for the case "PFI-550K" at $\Phi_{Total} = 0.55$ and 0.61 with and without PFI flame. The frequency of the PFI flame was 110 Hz.

the PFI spark was off for the "PFI-550K" and only a small amount of premixed fuel was injected (without PFI flame). This was not enough to suppress the instabilities. A periodic PFI flame was generated by the PFI spark and the instability was completely suppressed. Instabilities at $\Phi_{Total} = 0.66$ for non-preheated air were suppressed when the spark plug was activated as it can be seen in Fig. 6.8. Within the first 12 seconds, a PFI flame was generated by the activated spark plug and the RMS pressure level could be kept at a very low level.

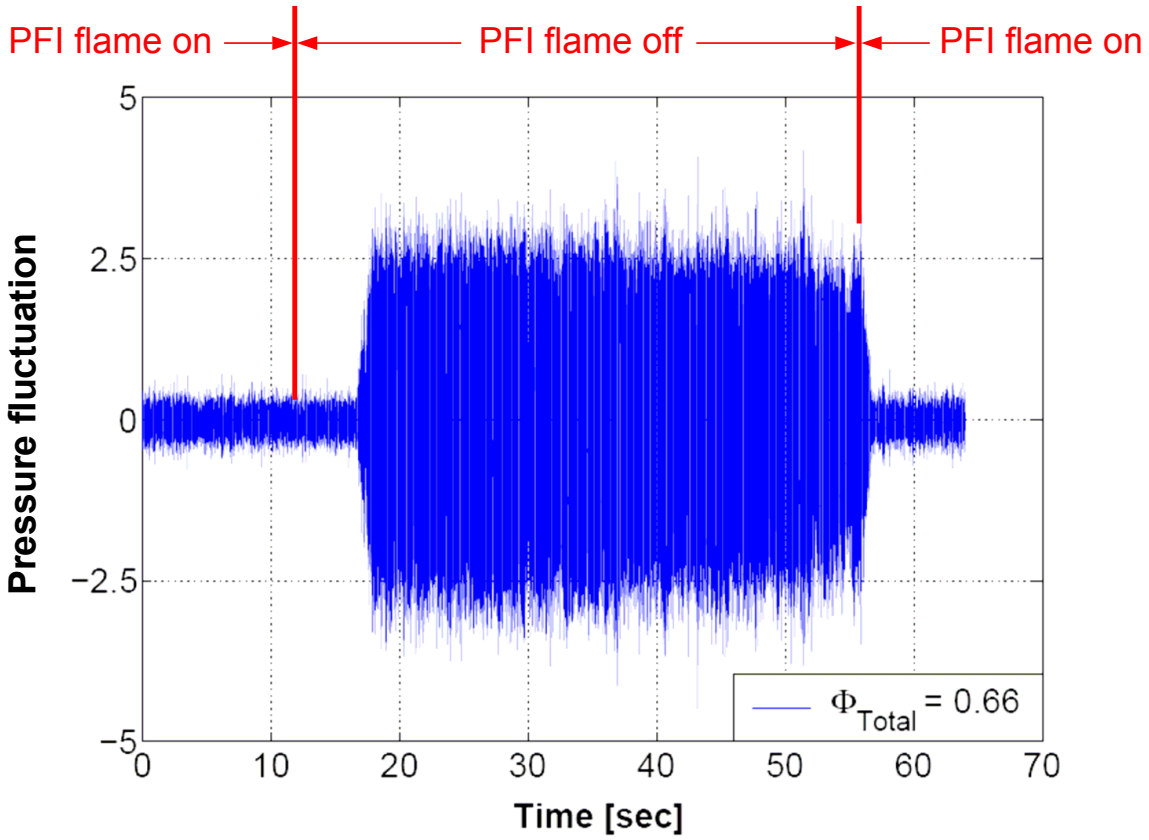

Figure 6.8: Timesignal of the pressure fluctuations for the case "PFI-300K" with and without PFI flame at $\Phi_{Total} = 0.66$. The frequency of the PFI flame was 110 Hz.

Even though the spark plug was switched off after 12 seconds, the combustion remained in a stable mode for approximately 6 seconds before becoming unstable. After 56 seconds, the spark plug was activated again and the instability was instantly suppressed. The time delay of several seconds between the switching off of the spark and the initiation of instabilities could be related to the fact that the flame front was stabilized inside of the combustor even though the PFI flame was already off.

Emissions

The impact of the instabilities on the emission behavior is shown in Fig. 6.9 where the NO_x emissions were recorded at different operating conditions and plotted versus the total equivalence ratio (Φ_{Total}). The curve referred to as "PFI flame off" corresponds to "PFI-550K" as described in section 6.3.1. Furthermore, the cases with activated PFI flame are referred to as "PFI flame" in the following. With an activated PFI flame, NO_x emissions were reduced when compared to the unstable baseline case. This is in agreement with Paschereit and Gutmark [72] who showed that unstable premixed combustion may increase NO_x emissions. It is interesting to note that the NO_x emissions between the "PFI flame" and the "PFI flame off" case are similar in stable regions ($\Phi_{Total} > 0.6$, compare Fig. 6.6) while the emissions significantly differ within the unstable region ($0.5 < \Phi_{Total} < 0.6$). Therefore, higher NO_x emissions are mainly generated by flame temperature peaks (induced by fuel/air ratio oscillation) during thermo-acoustic instabilities and not by the PFI flame itself. Only at $\Phi_{Total} < 0.5$ are the NO_x

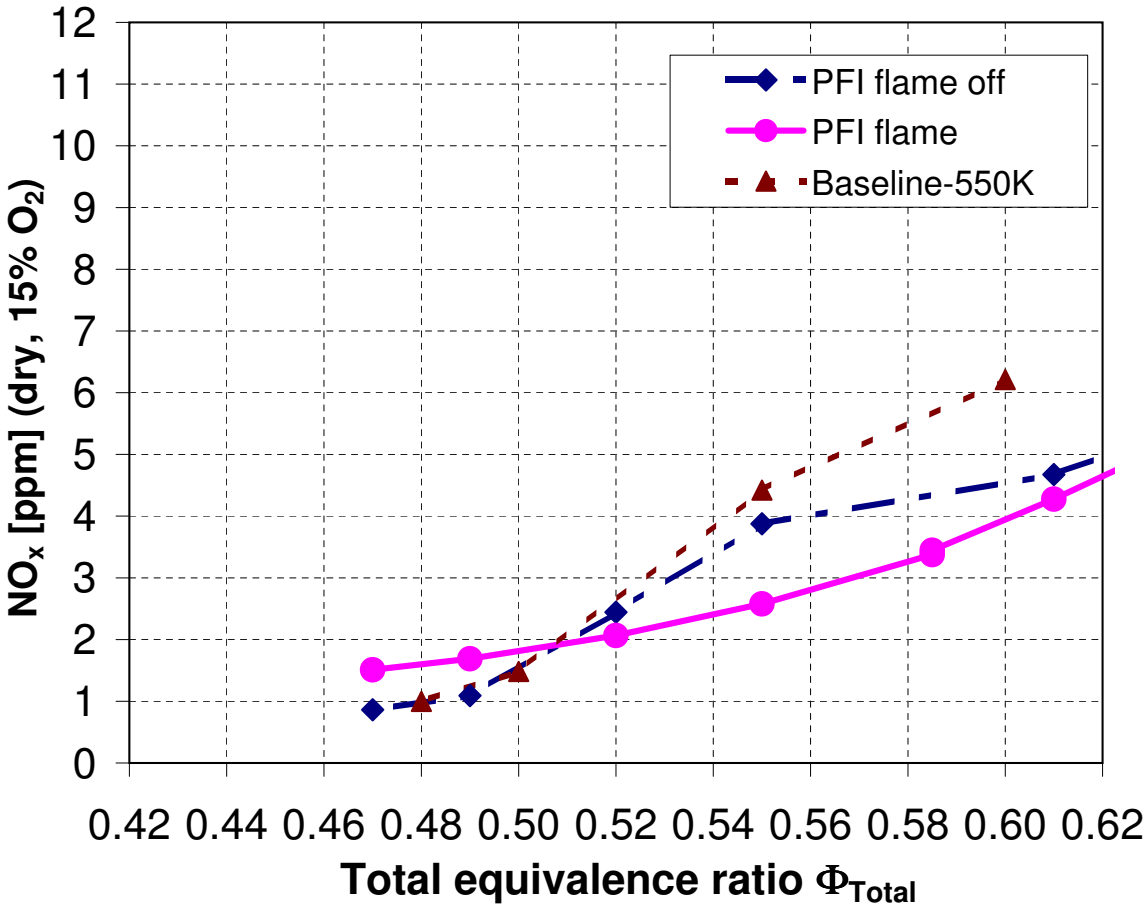

Figure 6.9: NO_x emission for the case "baseline-550K" and for the case "PFI-550K" with and without PFI flame. Note, the pilot ring was not installed in these tests.

emissions of the "PFI flame" case are slightly higher when compared to the "baseline-550K" and the "PFI flame off" cases which indicates higher flame temperatures near the stagnation point of the central recirculation zone.

6.3.3 Passive control of the time delay using the premixed ring

After having shown that the active controlled pilot (PFI) could significantly reduce pressure pulsation and emissions, it was of further interest to investigate a premixed pilot located closer to the outer shear layer. A pilot ring was installed at the burner dump plane (Fig. 5.1 and Fig. 5.2), where fuel or a fuel/air mixture could be injected directly into the shear layer. The main goal of this pilot injection location is to preserve the distributed heat release rate within the combustion chamber observed near the lean limit that seems to be less sensitive for instabilities. A detailed overview of the parameters setup used for this test and the definition of the cases can be found in section 6.3.1.

Pulsation and emission behavior

In Fig. 6.10, the normalized RMS pressure level versus Φ_{Total} for different injected mass flows through the pilot ring are presented. The data are normalized on the RMS pressure level of the baseline case ("Baseline") at $\Phi_{Total} = 0.47$. Using the premixed pilot ("Premixed ring"),

the starting p' excitation at $\Phi_{Total} > 0.47$ of the baseline case could be significantly delayed up to $\Phi_{Total} > 0.54$. Injecting the same amount of fuel through the pilot ring but without 15 kg/h air mass flow rate did not improve the dynamic stability up to a higher Φ_{Total} as it can be seen at the case "Diffusion ring". As expected, the NO_x emissions were also significantly higher in operating points with instabilities when compared to the "Premixed ring" case (Fig. 6.10) and indicates high flame temperature peaks caused by insufficient mixing of main fuel and main air. It is interesting to note, that NO_x emissions of the "Baseline" and the "Premixed ring" do not differ in operating points where both configurations are stable, thus, the pilot ring mixture seems not to influence the NO_x formation.

Mean flame heat release

To visualize the impact of the different injection configurations on the heat release distribution and the time delay, the averaged flame heat release was recorded with the ICCD camera and selected pictures of the "Air ring" and the "Premixed ring" are plotted in Fig. 6.10 while pictures of the other configurations are presented in Appendix E. The pictures allow both the axial flame position to be located and the flame thickness to be estimated, characterized by the spreading of the OH^*-chemiluminescence (see also section 6.3.4, Fig. 6.13). A greater spreading of the OH^*-chemiluminescence is also linked with a high variance of the convective time delay distribution. Increasing its value is also a method to reduce the pulsation amplitude of a combustion system as shown by Scarinci [86]. In this study, the pulsation level also correlates very well with the heat release distribution within the combustion chamber as the averaged OH^* images at two different operating points in Fig. 6.10 show. While the "Air ring" and "Premixed ring" case show a well distributed heat release rate near the lean limit ($\Phi_{Total} = 0.47$) and low pressure pulsations in both cases, the pulsation level increase with a more compact heat release rate at $\Phi_{Total} \approx 0.55$. Both parameters, the flame center location further downstream and the spreading of the heat release seem to affect the time delay and thus the amplitude of the pressure pulsations. The "Premixed ring" case presents high values of both parameters over a much wider equivalence ratio range (up to $\Phi_{Total} = 0.55$) than the three other cases. Thus, this case shows a positive impact on the two parameters relevant for the stability of the system.

6.3.4 Damping mechanisms

At all presented instability supression methods, the time delay between the injection and ignition of the main premixed (ignition time delay) has been changed to interrupt possible periodic flow structures that can feed existing pressure pulsations with a characteristic time of the combustor unstable mode. Either the time delay was changed by activating the PFI flame in case of "PFI-300K" and "PFI-550K" (Fig. 6.6) or the time delay of combustion conditions with reduced p' was preserved by activating the "premixed ring" (Fig. 6.10). The effect of different ignition time delays when applying the supression methods are illustrated in Fig. 6.11 and are marked by a representative arrow for each case. Note, there are numerous time delays for each case in practice so that the arrow length can only correspond with an averaged time delay. While the main combustion typically takes place shortly above the combustor dump in case of "Baseline" and is characterized by a compact and attached flame front, the main combustion takes also place within the cone when the PFI flame is switched on. Thus change the time delay, τ, so that e.g. $\tau_B > \tau_P$ can be assumed relative to one injection location. For the "Premixed ring" case, τ_R might be higher than τ_B relative to one injection location as the

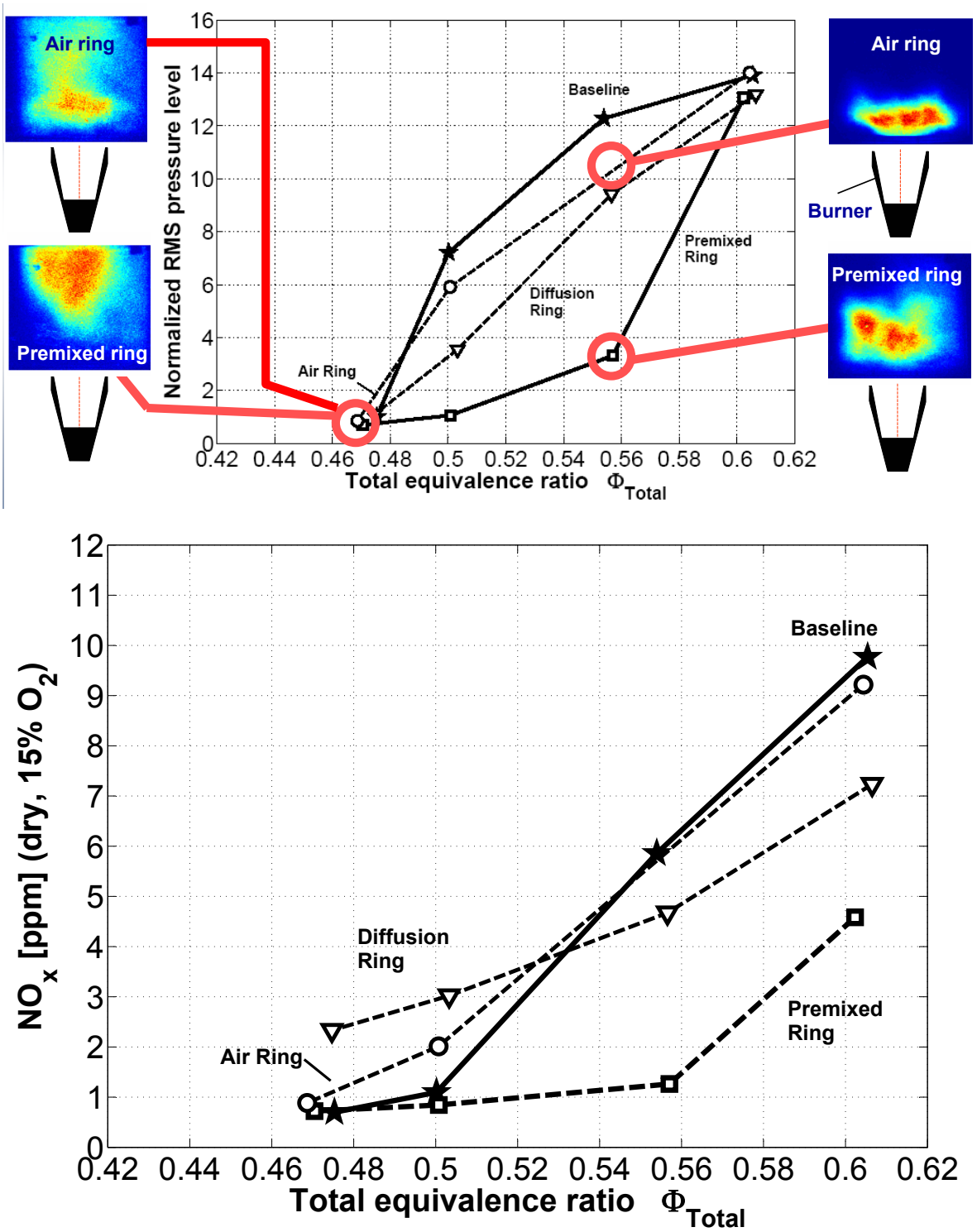

Figure 6.10: **Upper image:** Influence of the pilot ring flames (Air ring and premixed ring) on the normalized RMS pressure level. All RMS values were normalized on the background noise of the baseline case "Baseline" at $\Phi_{Total} = 0.45$. **Lower image:** NO_x emission for different pilot ring injection cases.

main flame is slightly lifted-off and more distributed within the combustion chamber. The degree of the heat release distribution within the combustion chamber is the major parameter

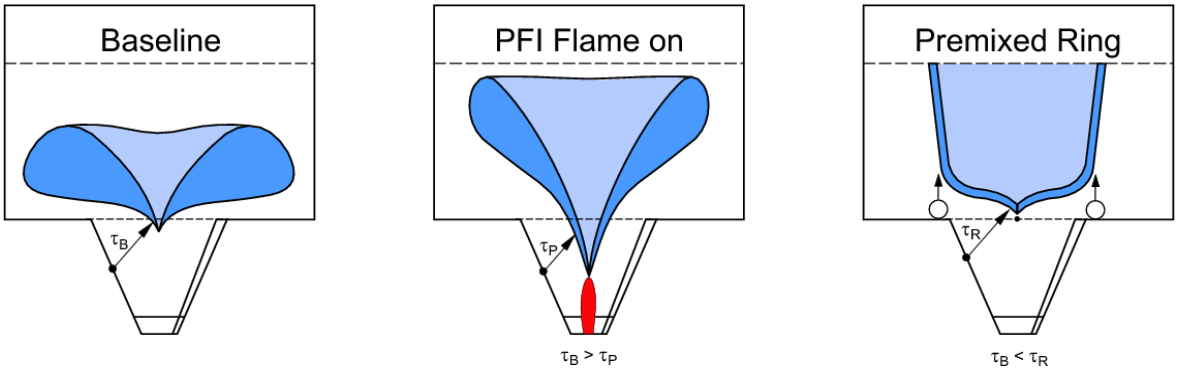

Figure 6.11: Different methods to change time delay between injection and ignition of the main premixed combustion.

to predict the amplitude of the pulsation level. The assumption can be derived from the pulsation level and the corresponding OH^* images for a defined main equivalence ratio Φ_{Main} seen in Fig. 6.12. Thereby, Φ_{Main} is defined as (6.4):

$$\Phi_{Main} \approx \frac{\dot{m}_{Main,fuel}}{\dot{m}_{Main,Air} \cdot FAR_{Stoic}} \tag{6.4}$$

with Φ_{Main} Main equivalence ratio,
$\dot{m}_{Main,fuel}$ Main fuel mass flow rate,
$\dot{m}_{Main,Air}$ Main air mass flow rate and
FAR_{Stoic} Fuel air ratio at stoichiometric conditions.

The amplitude of the pressure oscillations is strongly dependend on the spreading of the heat release distribution within the combustion chamber. While the compact flame front of the "Diffusion pilot" case shows the highest pressure level relative to the "Baseline", the pressure level continuously decreases with the spreading of the heat release rate in axial direction as shown by the "Air ring" and "Premixed ring" cases. Based on the experimental results, it can be concluded that the amplitude of p' can be directly controlled by the spreading of the heat release rate within the combustion chamber even though the critical frequency of the combustion system is hit. To explain the relationship between the critical time delay and the local heat release rate, two operating points of the "Premixed ring" case are shown in Fig. 6.13. In both cases, the time signal of the pressure fluctuations, the averaged heat release within the combustion chamber expressed by OH^* and the local heat release rate are shown. Note, local heat release rate along x-coordinate shown in Fig. 6.13 represents only a qualitative distribution while the color chart of the OH^* image base on different minimum and maximum value to visualize better the flame front. The exact numbers and the OH^* images base on the same min/max values can be seen in the appendix E, Fig. E.2 and Fig. E.3. At $\Phi_{Total} = 0.55$, the moderate p' can be traced back to a reduced local heat release rate due to the well distributed flame front within the combustion chamber. Even though the critical time delay is hit in this case, marked by a dashed line in the upper image of Fig. 6.13, the local heat release rate does not seem sufficient to increase the amplitude of p' further. However, if the averaged heat release rate is increased and limited on a smaller volume, as in case of $\Phi_{Total} = 0.6$, the local heat release rate increases near the critical time delay and leads to an oscillating main flame, as described in section 2. Similar conclusions can be drawn

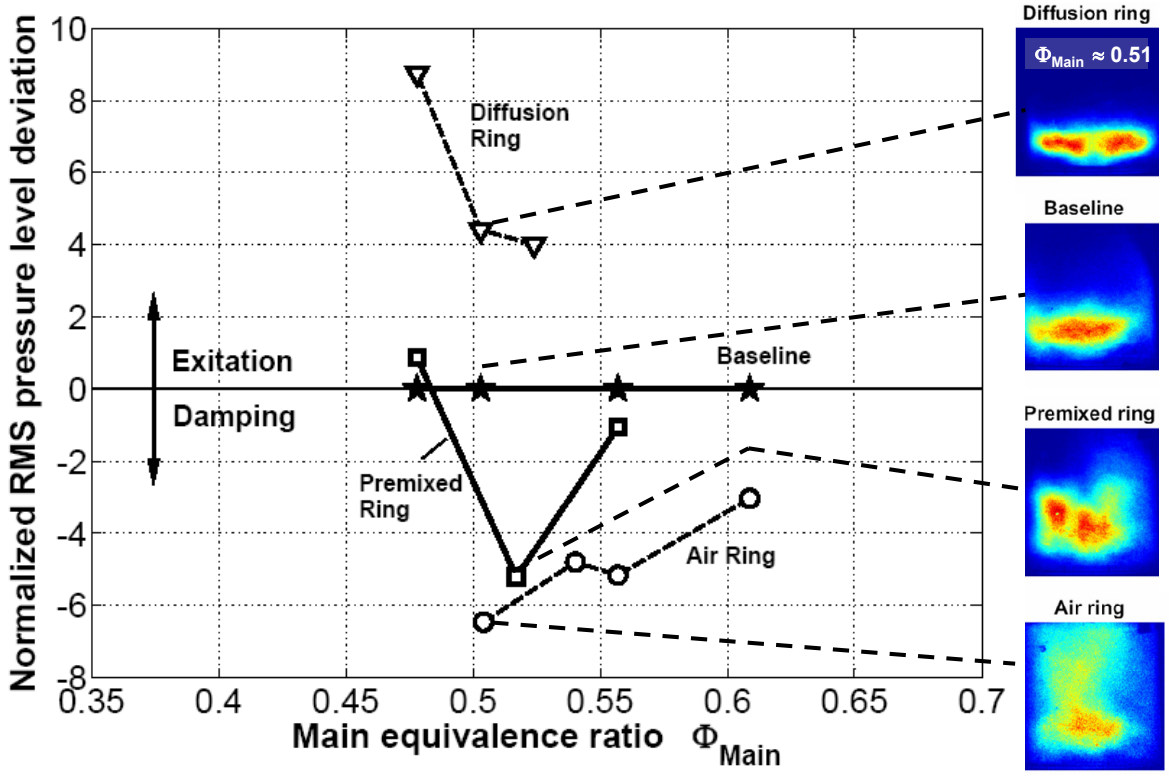

Figure 6.12: Impact of different pilot ring injection cases on the pulsation level. The damping effect of pressure oscillations increases with the spreading of the heat release rate.

from the "Baseline", the "Diffusion ring" and the "Air ring" case (see appendix E, Fig. E.3 – E.5). The resulting high p' amplitudes are mainly fed by the axially forward and backwards flapping flame front that indicates a high temporal variation of the time delay between the injection and ignition of the mixture. It is assumed that the flapping flame front can also be suppressed for these conditions if the momentum of the jet through the premixed ring is increased by a higher pilot mass flow rate. A high jet momentum in the axial direction might shift the ignition of the mixture further downstream and increases the spreading of the flame in axial direction again that seems to be linked with reduced p'.

6.4 Applied avoidance strategy to a swirl-stabilized combustor

One of the main requirement for applying the avoidance strategy to swirl-stabilized combustors is a low pulsation level near lean blowout. To extend the very narrow operating range with low pulsations, different control methods with PFI flames only and premixed ring injection only were successfully tested in sections 6.2 and 6.3. However, the premixed ring injection is the only tested control method in this study that fullfill the fail-safe requirement for gas turbine, so far. Instead, PFI flames sustained by a conventional spark plug with 110 Hz operating frequency are not fail-safe as the spark plug rapidely erode. Even though the spark plug could be theoretically replaced by a laser ignition device (section 2.3) with significant higher service life, the advantages of PFI flames for suppressing instabilities are strongly limited on selected operating conditions. Therefore, the methods are divided into two groups: methods for academic applications and for industrial applications.
To clearly show the potential of the avoidance strategy, the results are presented by different

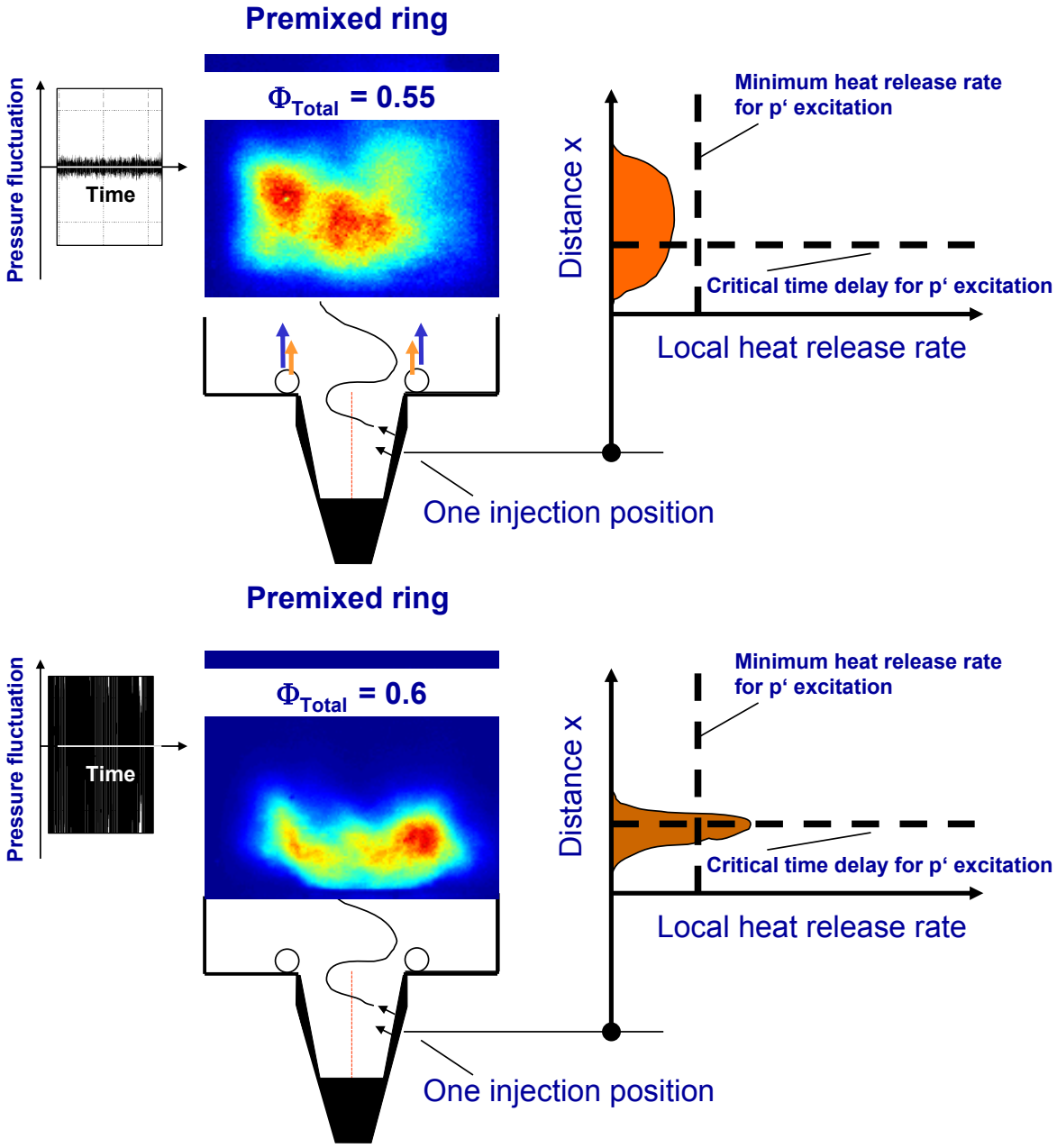

Figure 6.13: Local heat release distribution at different operating points. The distance between the flame front and the combustor dump was enlarged for the presentation to visualize the premixed ring injection. In reality, the flame front was much closer located at the combustor dump ($1 - 3$ cm).

normalized parameters as defined in section 6.1.

6.4.1 Academical application

For academic applications, the use of the PFI flame for the “LM” and the “RM” boundary extension is the most efficient method as the results compared with the baseline case in Fig. 6.14 clearly show. Note, the “LM” boundary is defined at 0 % of the x-axis and the “RM” boundary corresponds with the percentage of Φ_{total} based on $\Phi_{CO<1}$ where the normalized

RMS pressure level exceeds a factor of 2. While the combustor at baseline condition can

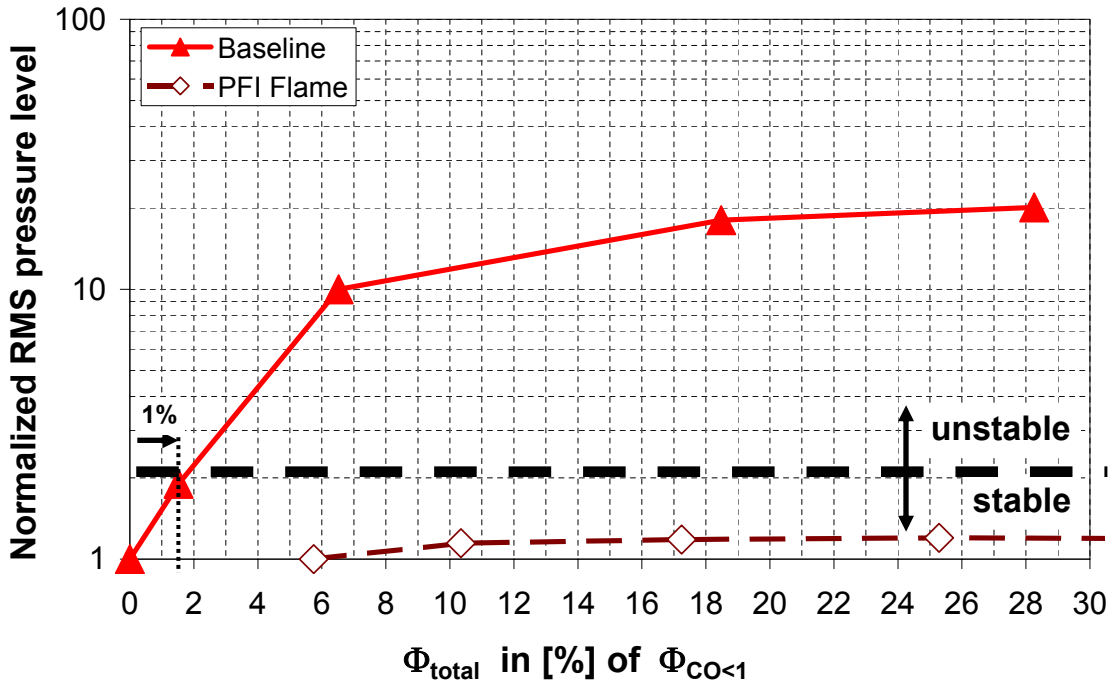

Figure 6.14: Applied avoidance strategy on swirl-stabilized combustors using the PFI flame as a control method. The image shows results for a preheat temperature of 550 K.

be only operated within a tiny Φ_{Total} range of 1 % without local extinction or instabilities, the use of the PFI flame significantly extends the operating range by up to nearly 30 %. However, the effectiveness of this method in terms of reduced p' can be only guaranteed if the unstable flame front of the main combustion is located shortly above the combustor dump before the premixed pilot mass flow rate is ignited by the spark. It might be difficult under gas turbine conditions to realize these conditions where even higher inlet temperature and higher inlet pressure level can be assumed. To prevent a flame front inside of the combustor cone at premixed pilot mixture injection, Φ_{Pilot} and the amount of the pilot mass flow rate could be adapted. Moreover, the time delay change using the premixed pilot flame does not guarantee reduced p' as previous tests have shown. It is assumed that either other acoustic modes of the system are excited by the presence of the premixed pilot flames or the time delay is only slightly changed so that the critical time delay keeps present. Therefore, the use of PFI flames seem not to be suitable for p' reduction in gas turbines. Instead, PFI flames have the potential to extend the "LM" boundary extension without efficiency losses and becomes attractive for gas turbine application if the conventional spark plug is replaced e.g. by a more durable one or by the laser ignition device.

6.4.2 Industrial application

The avoidance strategy can be also successfully applied with the use of the premixed ring injection that represents another control method for instability supression (Fig. 6.15). Stable combustion with low pressure pulsations and high combustion efficiency could be achieved at baseline condition only within a 2 % $\Phi_{CO<1}$ range. In the case of the applied avoidance strategy, the operating range could be significantly extended to richer mixtures, i.e. 13 % of

$\Phi_{CO<1}$. The "LM" boundary could not be extended with this method. Tests with combined diffusion pilot (PFI lance) and premixed ring (Pilot ring) showed the options of "LM" boundary extension but the damping impact on p' oscillation is reduced and the NO_x formation is increased (appendix B, Fig. C.4 (c)). To improve the "LM" boundary extension behavior with

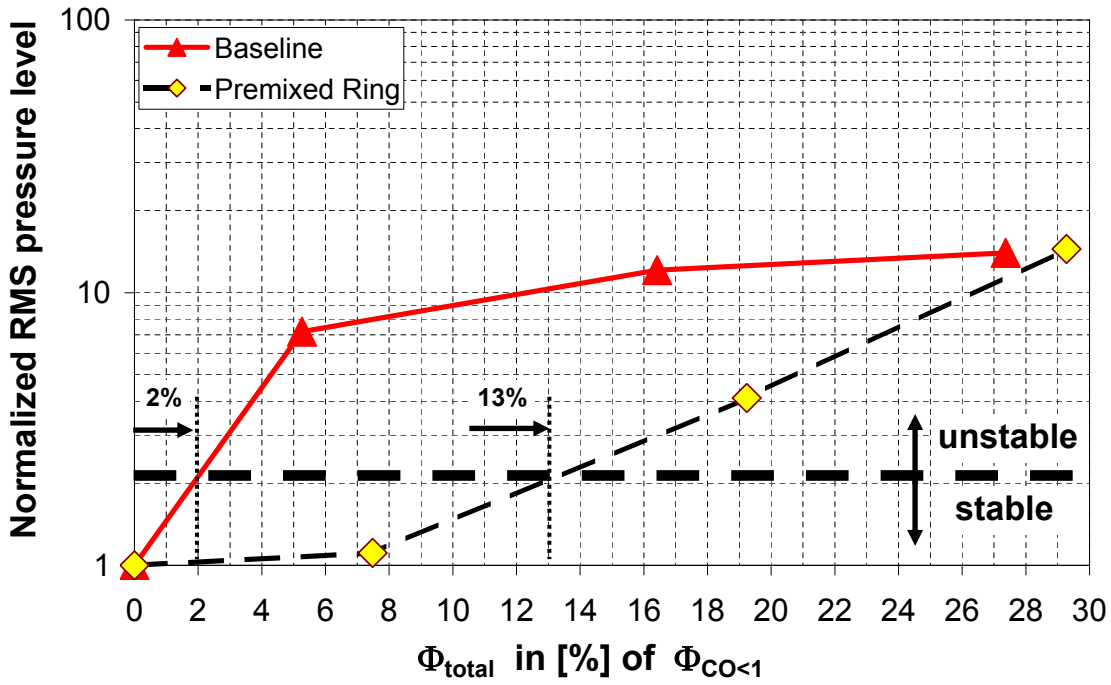

Figure 6.15: Applied avoidance strategy on swirl-stabilized combustors using the premixed ring injection as a control method. The image shows results for a preheat temperature of 550 K.

the premixed ring injection method, a pulsed laser should be directed at the lower stagnation point of the central recirculation zone to prevent local extinction (see Fig. 2.12).
One main advantage of the premixed ring when compared to the PFI flame is the fact, that the mechanism for reduced p' seems to be independent of the operating point. The mechanism is based on a broad-band time delay range due to a well distributed heat release rate in axial direction of the combustion chamber and is preserved by the premixed ring. Especially near the lean blowout limit, a spreading of the flame front can be already detected without using the premixed ring as studies with different burners have shown (see table 2.1, section 2.1). To prevent pressure pulsations with high amplitudes at these kind of burners, the main flame could be further operated at lean conditions (constant Φ_{Main}) while Φ_{Total} is varied by the fuel injection through premixed ring.

Chapter 7

Summary and conclusions

In this study, a strategy for emissions and instability prevention has been proposed for industrial swirl-stabilized combustors that is able to generate a specific flame structure with a broad-band time delay range and with high dynamic stability. To extend the operating range with this kind of flame structure (region 3 in Fig. 2.1), the premixed pilot, with its reduced NO_x formation, has been proposed as a fail-safe and simple control method. Different pilot locations within the combustion chamber were chosen to study the impact of pilot injection/flames on the lean mixture ("LM") and rich mixture ("RM") side of region 3 in terms of the stability and NO_x formation. The pilot flame injector (PFI) represents one premixed pilot injection that was located in the center of the swirl burner cone. Moreover, the premixed pilot could be ignited by an embedded spark plug inside of the PFI so that the main flame, especially near the lean limit, can be provided with additional radicals at its lower stagnation point in the central recirculation zone. A second pilot injection was located at the combustor dump to inject the pilot fuel/air mixture axially into the shear layer between the central and side recirculation zones. It could be shown for different main air preheat temperatures and with an activated PFI flame (at 110 Hz spark frequency) that the premixed pilot is the most efficient control method in extending the "LM" boundary of region 3 to leaner mixtures without CO emission increase. In the meantime, the NO_x emissions keep at similar levels to the baseline case. The control method becomes attractive for gas turbine applications if the conventional spark plug is replaced by a more durable one or by a laser ignition device. The efficiency of laser spark plugs has already been demonstrated under atmospheric conditions in [64] where different ignition devices were proposed to ignite a swirl-stabilized kerosine mixture. Moreover, tests with the PFI flame also indicate a direct control of instabilities so that high amplitude p' oscillations could be suppressed. The cause for p' suppression was traced back to a time delay change between injection and ignition of the main mixture when the main flame can be also detected within the burner cone at activated PFI flame. The method might be limited to academic applications as the suppressing effect could only be proved for very specific combustion conditions. At all other conditions, the premixed pilot flame didn't show an impact on the pressure oscillation levels. In contrast, the pilot ring injection seems to be more effective in preventing pressure pulsations, as tests in this study have shown. It could be deduced that the degree of the heat release distribution within the combustion chamber in axial direction can be increased by the premixed ring and correlates with decreasing pressure oscillation level. Compact flames seem to be more susceptible to instabilities when compared to flame fronts with a more distributed heat release rate and a broad-band time delay range. Moreover, the high momentum jet of the premixed ring mixture might stabilize the broad-band time delay distribution within the main flame so that the typical axial "flapping" of the

main flame can be suppressed.

To better understand the impact of the premixed ring, further tests with a new pilot ring geometry are recommended. Currently, the pilot ring geometry is not well adapted to the combustor geometry and might disturb the swirling flow at the combustor dump. To prevent flow perturbations, the pilot ring geometry should be integrated within a new burner flange. Several parameters seem to affect the spreading of the flame front in axial direction at premixed ring injection conditions, so far:

1. the momentum jet of the premixed ring and
2. the angle of the injected premixed ring mixture into the shear layer

To better evaluate the impact of the momentum jet and its angle on the spreading, further tests with different fuel injector geometries of the premixed ring are recommended. Moreover, the flow with and without premixed ring injection should be more closely investigated by PIV (Particle Image Velocimetry) measurements within a water channel (non reactive) and an combustion chamber (reactive) to better estimate the impact of the premixed ring injection on the swirl number and on the recirculation zones.

Appendix A

Impact of pilot injection configurations on the "LM" boundary

The impact of the pilot injection location on the "LM" boundary was assessed by the NO_x emission level, the CO level, the O_2 concentration and the exhaust temperature within the combustion chamber. The tests were conducted at constant 200 kg/h main air mass flow rate, 550 K preheat temperature and with a combustion tube of 200 mm diameter. Two different combustion chamber outlet diameter of 65 mm and 200 mm were chosen to achieve different lean blowout scenarios that could also occur in real gas turbines. While for the 65 mm outlet diameter case, the lean blowout process is started with low-frequency pulsations, the LBO for 200 mm outlet diameter case is introduced by a lift-off flame. The investigated cases are summarized in tables A.1 and A.2. For the 200 mm tube diameter cases, the periodical

Table A.1: List of test cases that show reduced impact on the "LM" boundary using a combustion tube with 200 mm outlet diameter.

Pilot air kg/h	**Pilot fuel kg/h**	**Ring air kg/h**	**Ring fuel kg/h**
1	0.00	0	0.00
1	0.96	0	0.00
15	0.96	0	0.00
15	0.96	5	0.32
15	0.96	13	0.84

ignited pilot mixture at the combustor apex (PFI flame, see Fig. 5.1) is able to prevent local extinctions very efficiently with only moderate NO_x emission formation (Fig. 6.4). Tests with additional pilot ring injection were also done with the 200 mm tube diameter configuration, but with less success to shift the "LM" boundary to lower equivalence ratios without a further increase in CO emission (Fig. A.4). The O_2 concentration, the exhaust temperature and the CO level didn't change significantly when compared to cases without additional pilot ring injection (see Fig. A.6, A.10). In contrast, combustion tests with the 65 mm tube identifies the pilot fuel injection as the most efficient method for LM boundary extension (see Fig. A.1). To improve the effect of the pilot premixed injection for this configuration, a combined injection through the PFI and the pilot ring was proposed. Even though the setup is more complex than that of the pilot fuel injection, a significant increase of the NO_x emissions could not be

Table A.2: List of test cases that show reduced impact on the "LM" boundary using a combustion tube with 65 mm outlet diameter.

Pilot air kg/h	**Pilot fuel kg/h**	**Ring air kg/h**	**Ring fuel kg/h**
1	0.00	0	0.00
1	0.64	0	0.00
1	0.64	0	0.32
1	0.64	0	0.50
1	0.64	0	0.96
10	0.64	0	0.00
10	0.64	0	0.32
10	0.68	0	0.32
10	0.64	0	0.50
10	0.64	0	0.96
14	0.98	0	0.00

prevented (Fig. A.2). In the following, the NO_x emissions, the CO, the O_2 and the exhaust temperature will be discussed for the 65 mm tube diameter cases.

NO_x emissions

All NO_x emissions were normalized according the definition mentioned in section 6.1. Based on the two basic configurations shown in Fig. A.1 for a 65 mm tube, the pilot injection at the combustor apex was kept constant for the presented test cases in Fig. A.2 while the pilot ring conditions were varied in the pilot fuel and pilot air mass flow rates. The left column shows the test results for a constant pilot fuel mass flow rate through the PFI lance, the right column for a constant pilot mixture through the PFI. In general, it can be derived from the results that an increase of the pilot ring mass flow rate is able to extend the "LM" boundary. But, the NO_x emissions could not be kept on similar level as the baseline case. In the most cases (case a, case b and case c), either the pilot ring injection method is inefficient or the NO_x emissions exceed the level of the diffusion PFI case ("1 0.64 0 0"). Only, case d) with a combined premixed PFI and diffusion ring injection seems to be more effective for "LM" boundary extension when compared to the diffusion PFI case. But, the improvement is compensate by a slightly higher NO_x emission level.

It was further of interest to investigate the impact of the diffusion and premixed ring injection only on the "LM" boundary extension. The results for the diffusion ring case are shown in Fig. A.3 and indicates only a weak impact while the premixed ring case ($\Phi_{Pilot} = 1.1$) was completely inefficient to extend the "LM" boundary (compare Fig. 6.10).

CO emissions and O_2 concentration

The CO emission and the O_2 concentration near the "LM" boundary for the discussed cases in Fig. A.2-A.4 increase to leaner mixture as it was expected before. It has to be noticed that the O_2 concentration for the 65 mm tube diameter case is in all investigated operating points

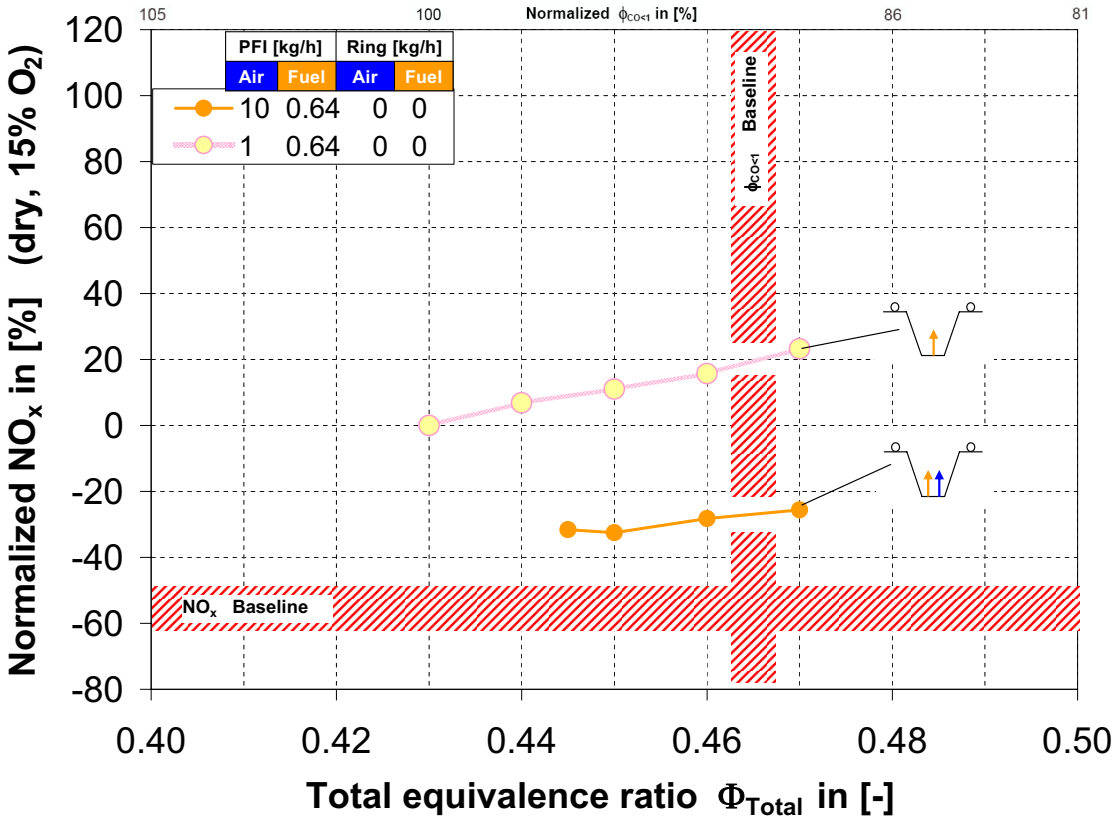

Figure A.1: NO_x emission behavior at different pilot mass flow rates through the PFI, w/o pilot ring injection. For the tests, a combustion tube with a 65 mm outlet diameter was chosen and the air preheat temperature was set on 550 K.

lower ($\Delta O_2 \approx 1$ Vol%) when compared to the 200 mm tube diameter case. The lower O_2 concentration might be traced back on a fully reaction of the fuel with the overplus of oxygen. The assumption could not be confirmed so far as an analyze device for UHC concentration was not available until the end of this study.

Exhaust temperatures at two different positions within the combustion chamber

The exhaust temperature was measured at two different positions within the combustion tube as it was illustrated in Fig. 5.1. The position closer located to the combustion dump is reffered as “bottom”, the position further downstream is reffered as “top” in the following.

A typical temperature behavior at different operating points can be seen in all investigated cases (A.7-A.10). The exhaust temperature decreases to leaner mixture, the temperature at the “top” position is slightly lower and the temperature level at one thermocouple location is for all cases similar. For the 200 mm tube diameter in Fig. A.10 was indicated a decrease of the “top” temperature to richer mixture that is not physical. It is assumed that starting instabilities with increased pressure fluctuation level lead to a backflow of cold air into the upper region of the combustion tube that reduces significantly the exhaust temperature. Sim-

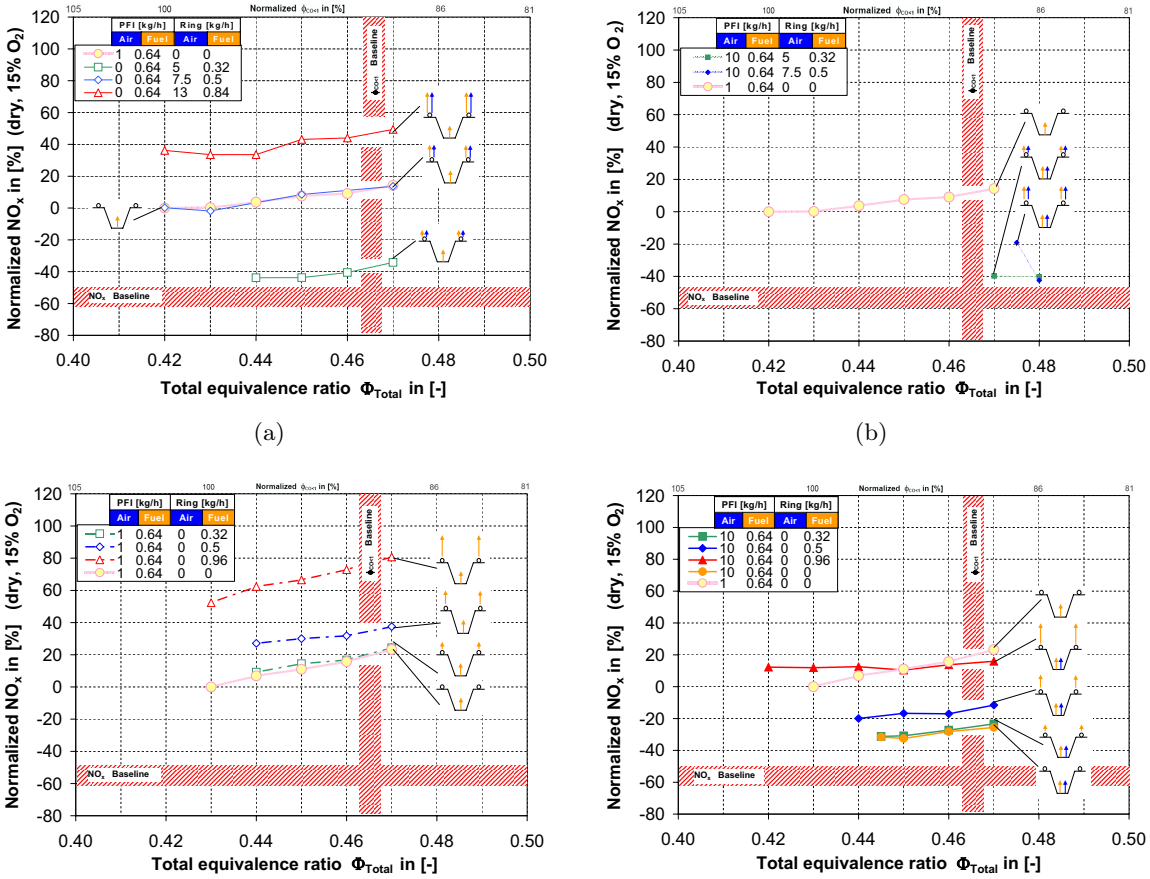

Figure A.2: The NO_x emission behavior were investigated at the combined use of the PFI lance and the pilot ring. For the tests, a combustion tube with a 65 mm outlet diameter was chosen and the air preheat temperature was set on 550 K for a main air mass flow rate of 200 kg/h.

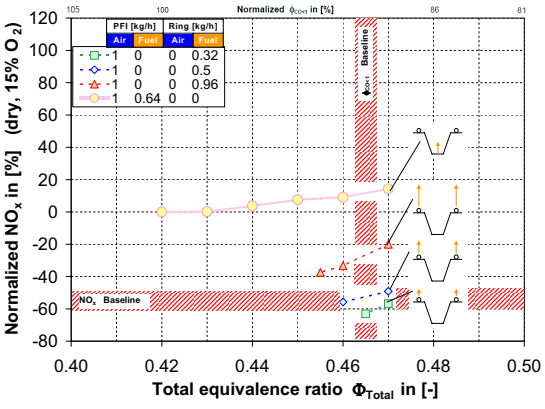

Figure A.3: NO_x Emission formation at specific conditions: Pilot ring injection only, 65 mm tube diameter, air preheat temperature of 550 K. The "LM" boundary could not be further extended under this conditions.

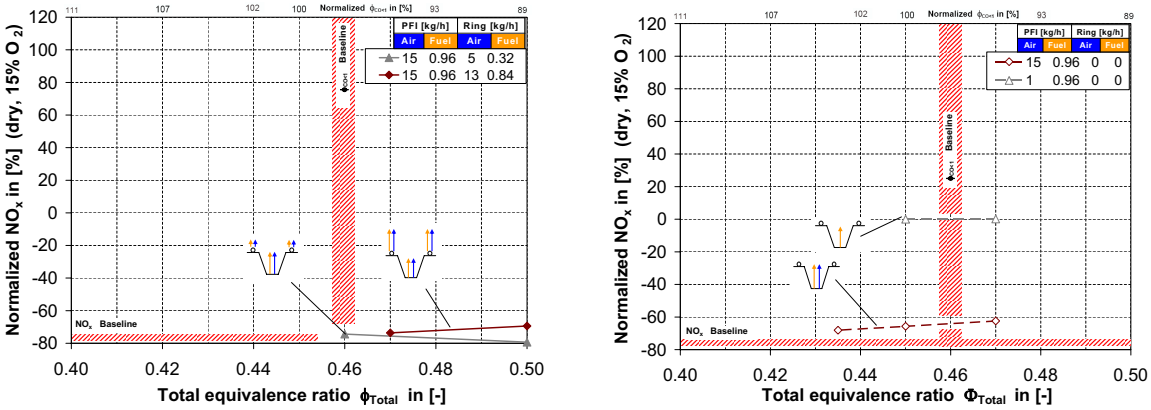

(a) (b)

Figure A.4: NO_x emission behavior at pilot injection (PFI) with and without ring injection: NO_x emissions, 200 mm tube, 550 K.

ilar effects could be seen in [9].

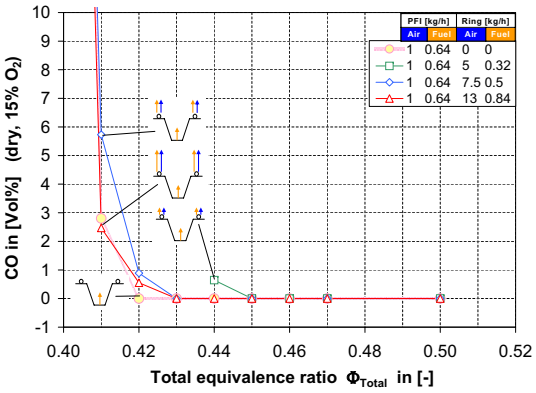

(a) 65 mm tube

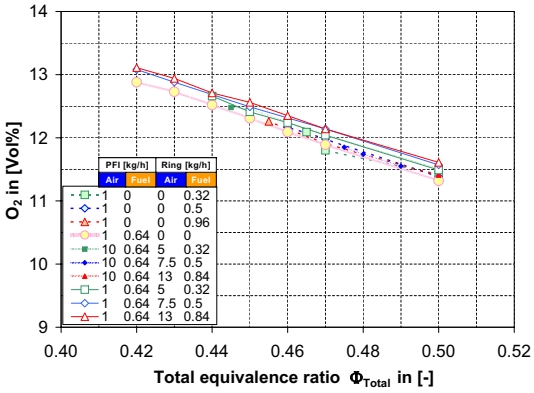

(b) 65 mm tube

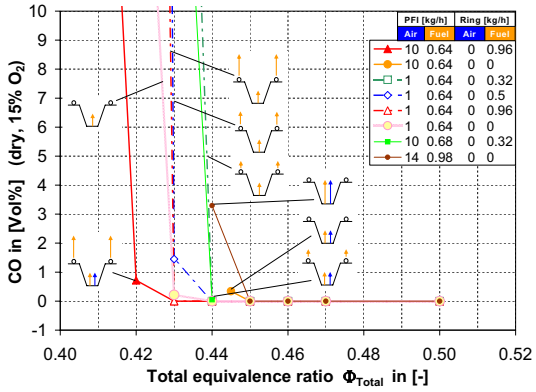

(c) 65 mm tube

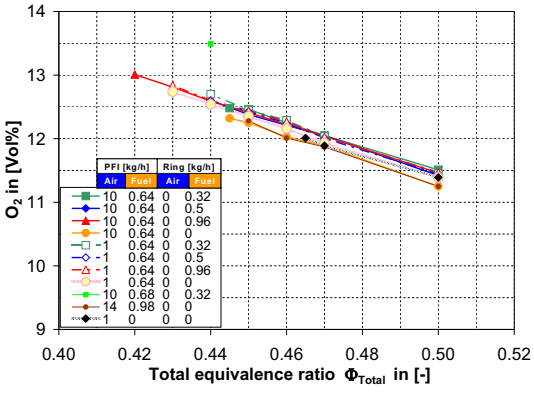

(d) 65 mm tube

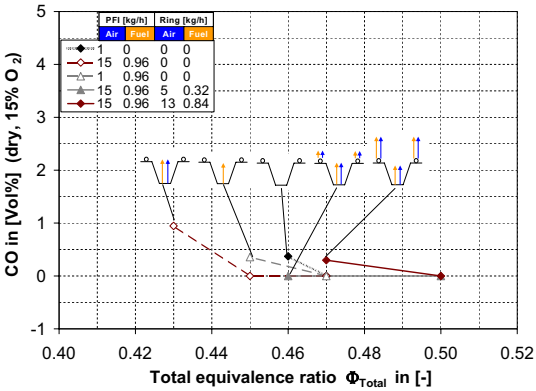

(e) 200 mm tube

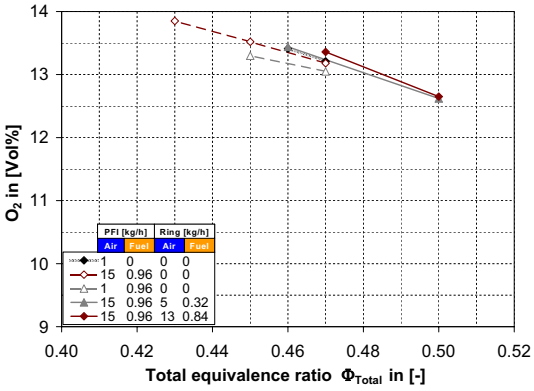

(f) 200 mm tube

Figure A.5: CO Emissions and O_2 concentration versus Φ_{Total} for the 65 mm and 200 mm tube outlet diameter test cases with a preheat temperature of 550 K.

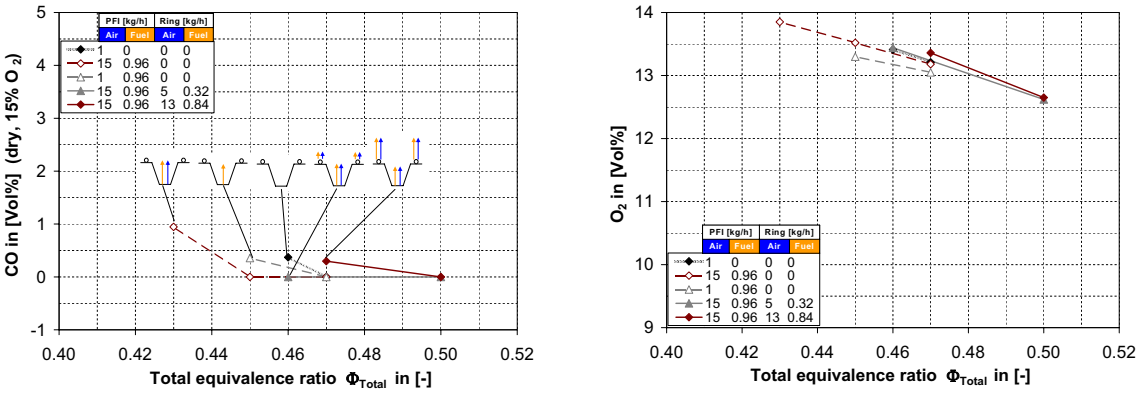

(a) (b)

Figure A.6: *CO* Emissions and O_2 concentration versus Φ_{Total} for the 200 mm tube outlet diameter test cases with a preheat temperature of 550 K.

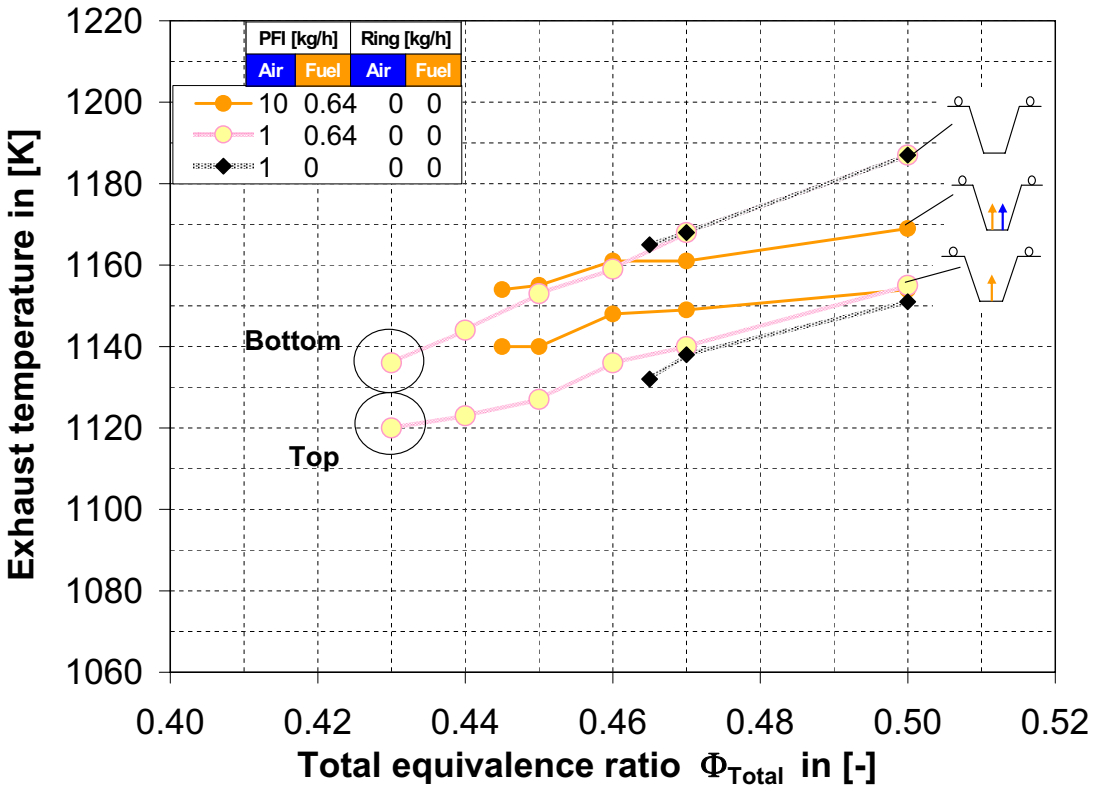

Figure A.7: Exhaust temperature behavior without ring injection. For the tests was used a combustion tube with an outlet diameter of 65 mm; the preheat temperature was set on 550 K and the main air mass flow rate on 200 kg/h.

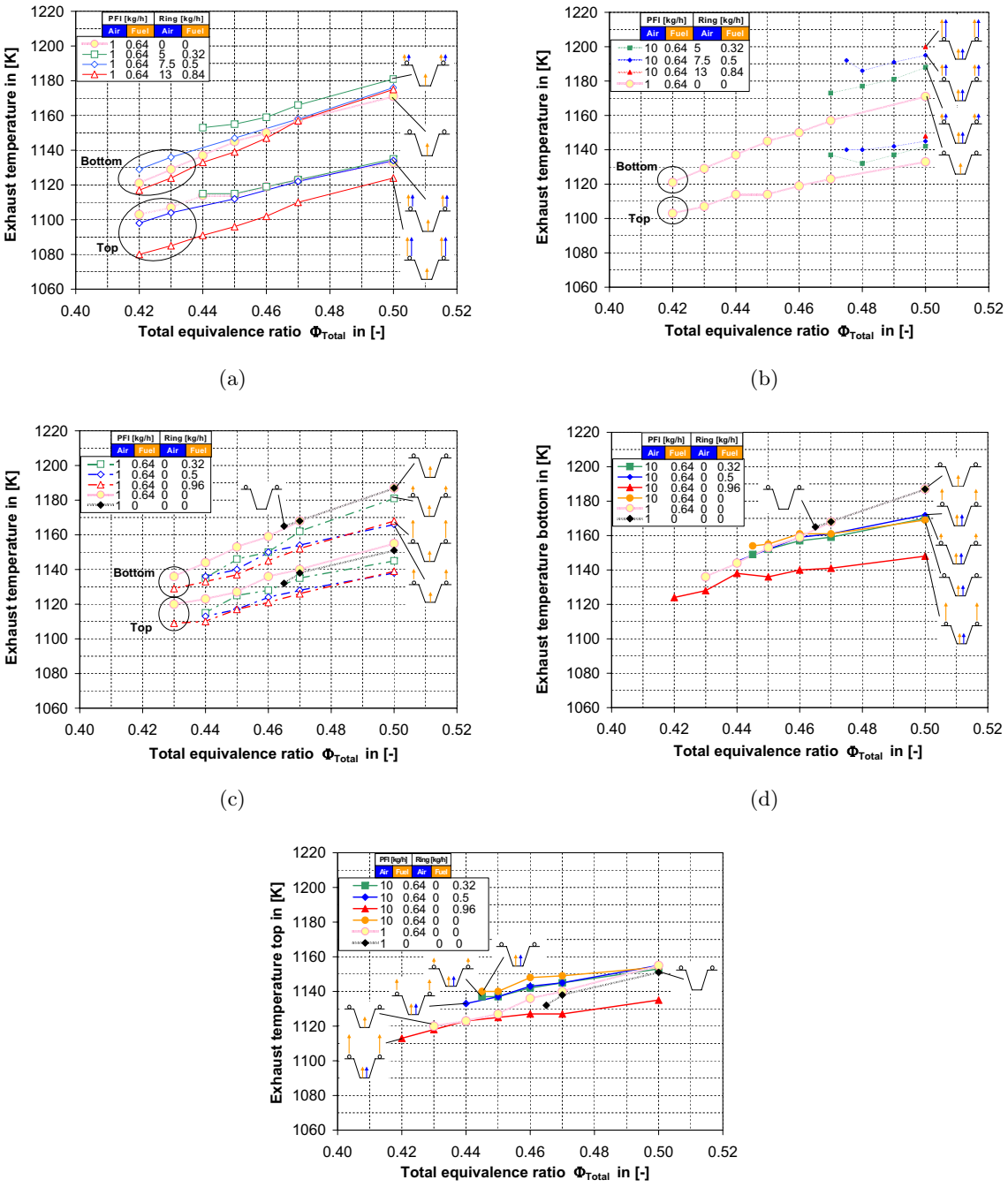

Figure A.8: Exhaust temperature behavior at combined PFI and ring injection for different operating points and different location behind the combustor dump. At all tests, the outlet diameter of the combustion tube was 65 mm while the air preheat temperature was kept constant at 550 K for a main air mass flow rate of 200 kg/h.

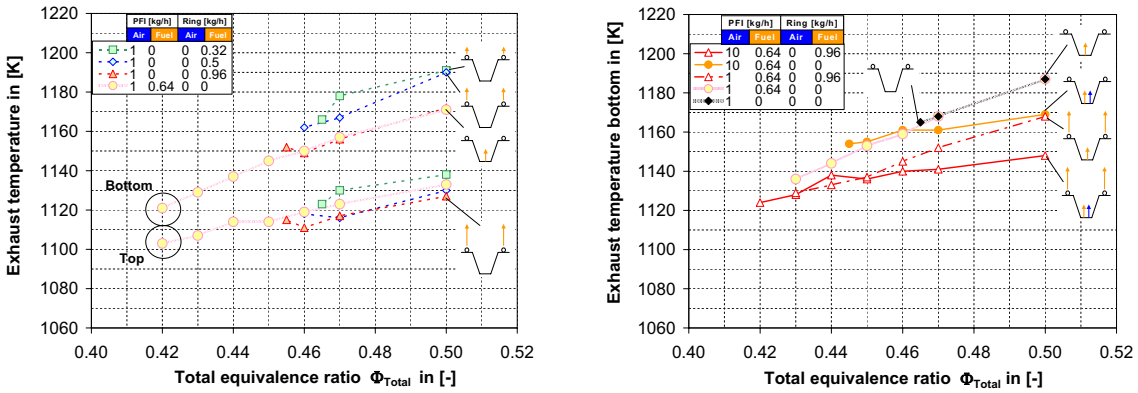

(a) (b)

Figure A.9: Exhaust temperature behavior at different operating points and different location behind the combustor dump. At all tests, the outlet diameter of the combustion tube was 65 mm while the air preheat temperature was kept constant at 550 K.

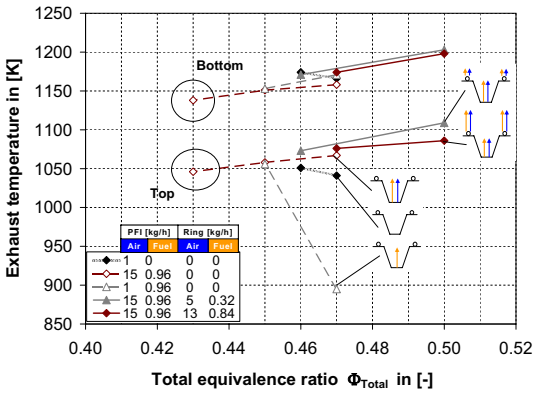

(a)

Figure A.10: Exhaust temperature behavior at different operating points and different location behind the combustor dump. At all tests, the outlet diameter of the combustion tube was 200 mm while the air preheat temperature was kept constant at 550 K.

Appendix B

Basic behavior of the burner at different operating conditions

The basic behavior of the premixed combustion was closer investigated in this study to figure out operating conditions where the avoidance strategy with the proposed pilot injection methods can be successfully applied. For this reason, stability maps of the swirl burner investigated at different outlet tube diameters and parameters indicating unstable conditions (Rayleigh index) are closer discussed in the following.

Stability map

A stability map of the swirl-stabilized combustor shown in Fig. B.1 was generated with the combustor tube of 200 mm diameter while a preheat temperature of 550 K was set. Stable and unstable[1] combustion conditions were marked with blanc and filled red circles. Different main air mass flow rates between 200 kg/h and 250 kg/h were set while different pilot injection mass flows through the pilot lance (combustor apex) were chosen. For the pilot injection was chosen 0.33-0.7 kg/h pilot fuel mass flow rate that was only injected into the combustion chamber or was mixtured before injection with pilot air mass flow rates 7.5 kg/h or 10 kg/h. The pilot ring was not installed above the combustor dump. The detailed setup has been summarized in table D.1. Independent of the main air mass flow rate (and the amount of pilot mass flow rate through the pilot lance), stable conditions could be only achieved within a small Φ_{Total}-band shortly before lean blowout occurs. Similar results could be shown in works [27, 53, 45] and were discussed in section 2.1. In Fig. B.2, the RMS pressure level and the emissions are visualized for the case at 200 kg/h without pilot injection to investigate the combustion behavior near LBO closer. A combined decrease of the RMS pressure level and the NO_x emissions could be detected so that the level of both parameters are very low shortly before LBO occurs. The normalized RMS pressure level is factor 16 reduced at $\Phi_{Total} = 0.6$ when compared near LBO at $\Phi_{Total} = 0.47$. Therefore, a tiny operating range at $0.46 < \Phi_{Total} < 0.48$ exists where the NO_x emission due to low flame temperatures are also reduced while the CO emissions still keep on low level. To extend this operating range in both direction, to leaner and richer mixture, the LBO has to be extended and the pulsation level increase has to be suppressed or delayed by suitable control methods (see section 6.2, 6.3.2 and 6.3.3).

Selected RMS pressure levels of different test cases described in table 6.2 are presented

[1] definition see 6.1

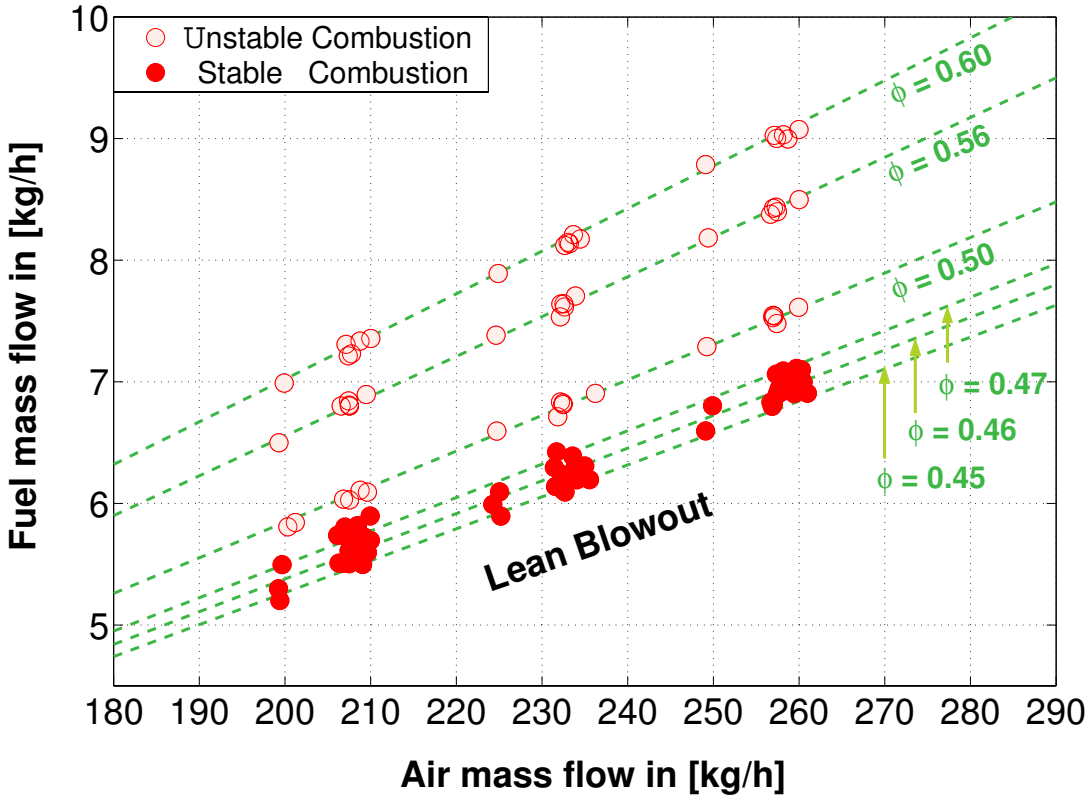

Figure B.1: Stability map of the swirl burner EV-10 tested under atmospheric conditions. The tests were conducted with a combustion outlet diameter of 200 mm.

in Fig. B.3 and were compared with the baseline case "Baseline-550K" and the case "PFI-550K-65mm". While "Baseline-550K" was conducted without any pilot injection and with the 200 mm combustor tube configuration, the tests with "PFI-550K-65mm" were done with the same amount of pilot injection as the "PFI-550K" case, but with an combustor tube outlet diameter of 65 mm. It can be shown, that the RMS pressure level of the "Baseline-550K" and the "PFI-550K" do not differ significantly. A rapid increase of the pressure pulsation can be detected in both case at $\Phi_{Total} = 0.47$ while the maxima deviate in the range of 15 % at $\Phi_{Total} = 0.6$. Also for the case "PFI-300K", unstable conditions with high RMS pressure level could be observed at $\Phi_{Total} > 0.67$ even though the RMS pressure level was significantly reduced at $\Phi_{Total} = 0.73$. The reduced amplitudes of pressure oscillation were caused by stable combustion with a duration of 3-5 s between short periods of unstable conditions. Φ_{Total}-values higher than 0.83 were not set as the exhaust temperature would exceed the maximum temperature of 1450 K for the k-type thermocouples.
The RMS pressure level of the case "PFI-550K-65mm" seen in Fig. B.3 remained low within the whole investigated operating range and increased slightly only close to the LBO, independent of the preheat temperature. At those points, low frequency pressure oscillations at 1-5 Hz could be detected. Further details are mentioned in section 6.2.

Table B.1: Investigated operating points for the stability map at 550 K preheat temperature and at a tube diameter of 200 mm. For the pilot injection cases, the pilot mass flow were only injected through the pilot lance (combustor apex) while the spark plug was off. The pilot ring was not installed in these tests.

$\dot{m}_{Main,Air}$ **in kg/h**	$\dot{m}_{Pilot,Air}$ **in kg/h**	$\dot{m}_{Pilot,Fuel}$ **in kg/h**	Φ_{Pilot}
200	––	––	––
225	––	––	––
250	––	––	––
200	––	0.33	––
200	––	0.44	––
200	––	0.53	––
200	7.5	0.33	0.7
200	7.5	0.44	1.0
200	7.5	0.53	1.2
200	––	0.41	––
200	––	0.54	––
200	––	0.70	––
200	10	0.41	0.7
200	10	0.54	1.0
200	10	0.70	1.2

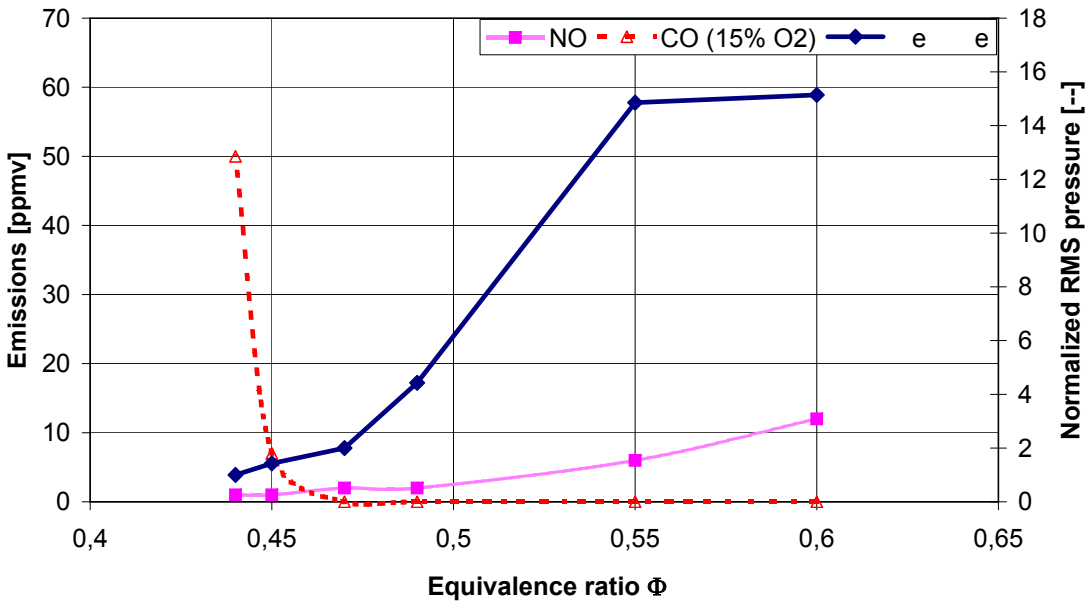

Figure B.2: Near the lean blowout, a small band existed where no instabilities occurred and CO emissions were still low. It is consistent with former investigations ([27, 53, 45]). The RMS pressure was normalized on the RMS level at $\Phi_{Total} = 0.44$.

Rayleigh Index

The instabilities found for the cases "PFI-550K" and "PFI-300K" were more closely investigated to better quantify the intensity of the instabilities. Therefore, the OH chemilumines-

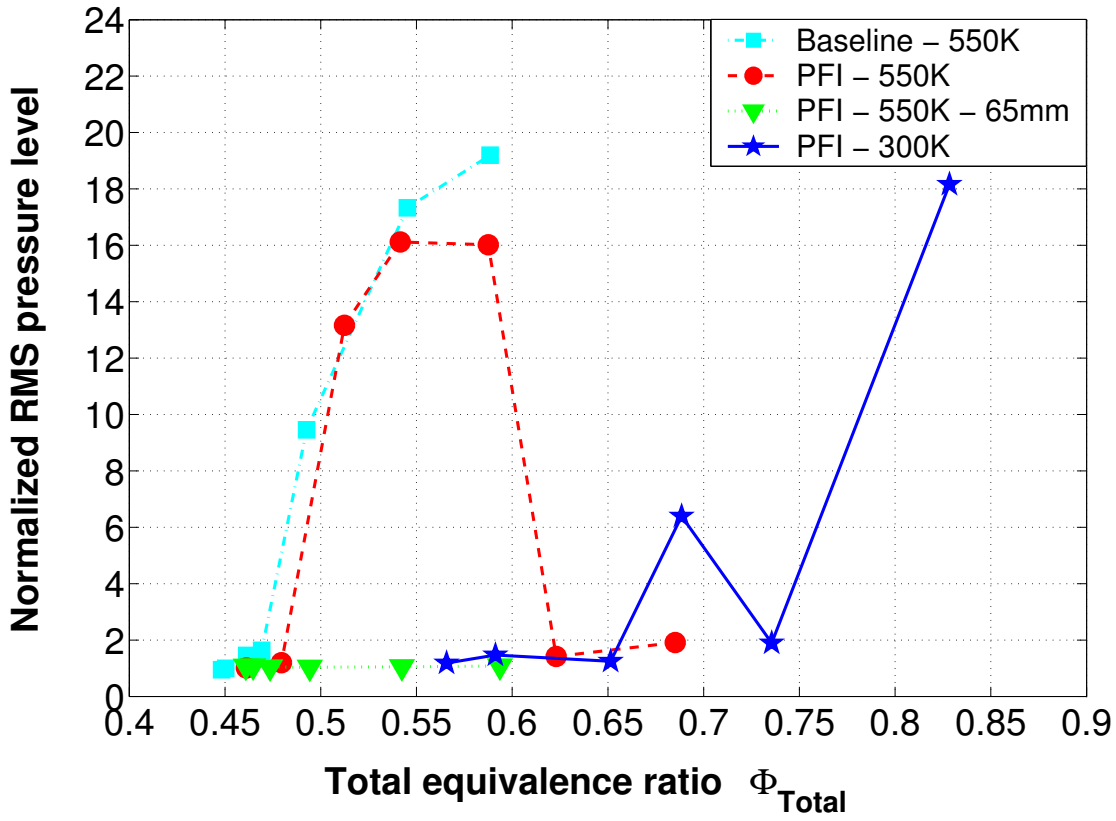

Figure B.3: Stability map of a swirl-stabilized combustor for different preheat air temperatures 300 K and 550 K and combustion outlet diameters 65 mm and 200 mm. The ignition device was in all cases off, so that no PFI flame was generated. Test with activated PFI flame for the "PFI-550K-65mm" did not show an impact on the pulsation level.

cence (OH^*) and the pressure fluctuations p' of the oscillating premixed flame were simultaneously recorded, which is shown in Fig. B.4 for the "PFI-550K"-case at $\Phi_{Total} = 0.55$. The phaseshift of less than 90° between these two signals indicates clearly unstable conditions. Also the Rayleigh index R, calculated by the formula:

$$R = \int_0^{Time} p'(t) \cdot (OH^*)'(t)dt \quad > 0 \tag{B.1}$$

was fulfilled and greater than zero, respectively (Fig. B.4).

Power spectrum and phase-averaged OH^* chemiluminescence

The power spectrum for the case "PFI-550K" at condition "PFI flame off" shows a distinct fundamental at 110 Hz with an amplitude nearly three orders of magnitude higher than the background noise (Fig. B.5). Note, the fundamental is successfully suppressed by the activated "PFI flame" and a new peak, but with two magnitude lower, can be observed at around 120 Hz. The difference between the frequency with and without PFI flame might be traced back on different flame temperatures and different combustion efficiencies. The assumption seems to be correct as the excess O_2 concentration and the NO_x emissions for the "PFI flame off" case

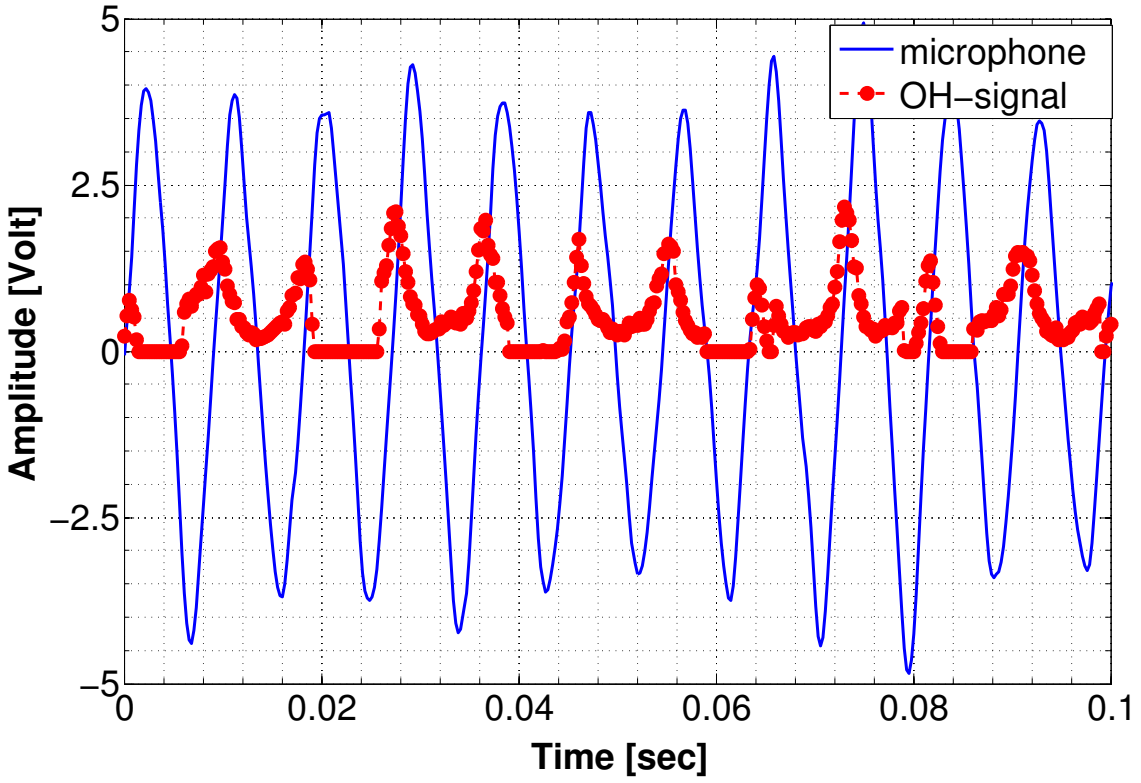

Figure B.4: OH-chemiluminescence and pressure signal for the case "PFI-550K" at $\Phi_{Total} = 0.55$.

are significantly higher when compared to the "PFI flame" case and correspond with reduced flame temperature and reduced frequency (Fig. B.5 and Fig. 6.9, section 6.3.2). To visualize

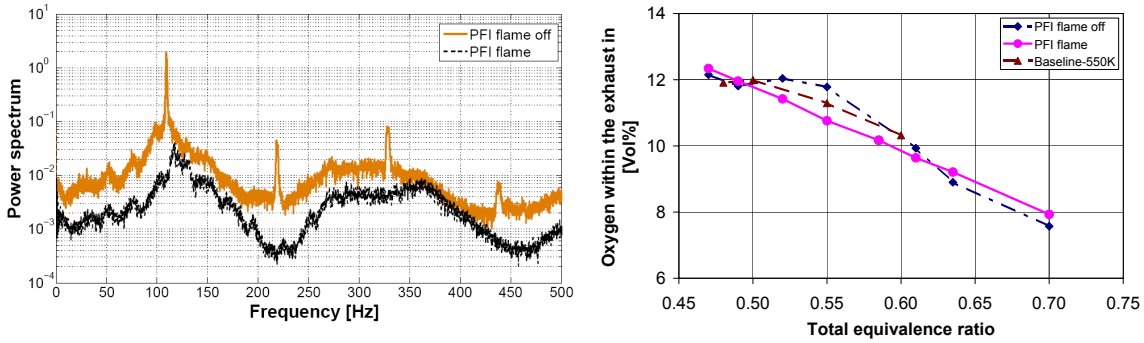

Figure B.5: Powersprectrum for the case "PFI-550K" with and without PFI flame at $\Phi_{Total} = 0.55$ (left) and corresponding excess oxygen within the exhaust.

the oscillating character of the unstable lean premixed (main) flame for the "PFI-300K" case at $\Phi_{Total} = 0.66$, phase-averaged OH^* images were recorded in 45 ° steps while the images for each phaseshift angle were calculated from 40 single images (Fig. B.6). At 45 ° the highest OH^*- chemiluminescence can be detected within the shear layer between the side and the central recirculation zone.

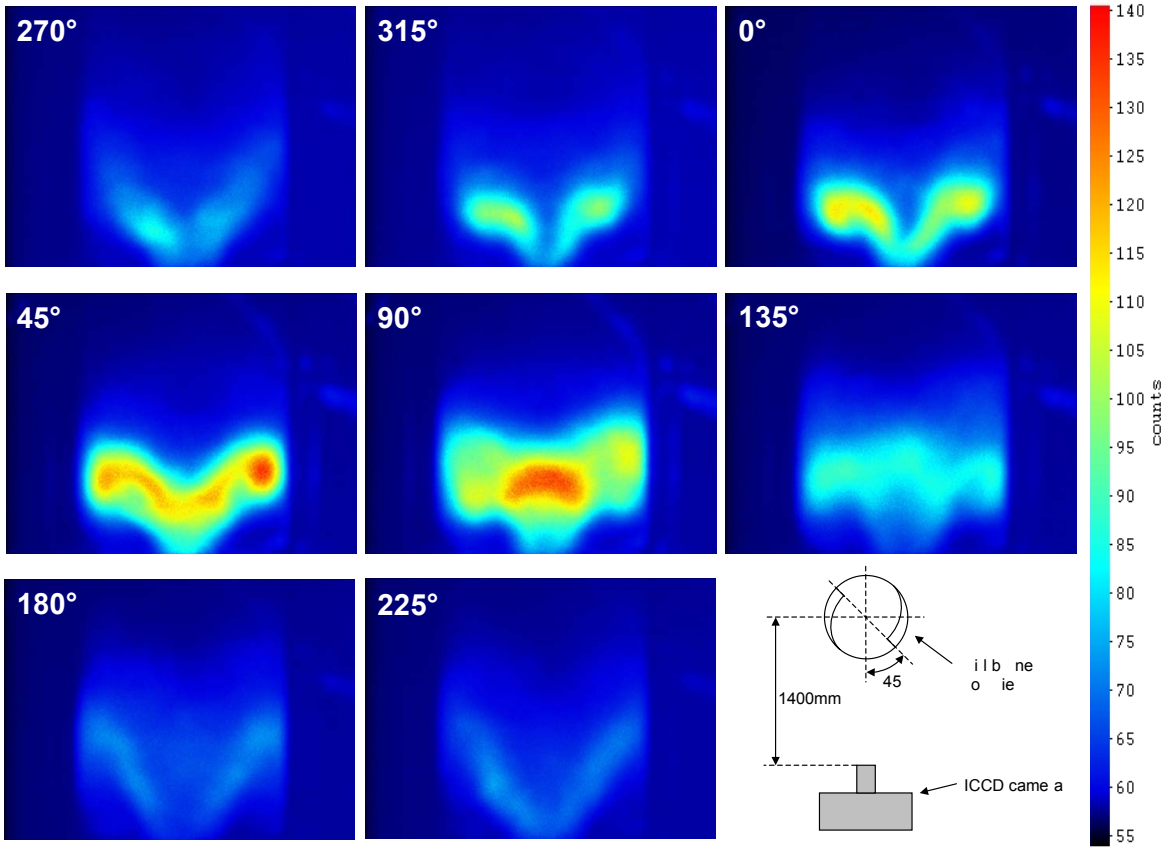

Figure B.6: Phase averaged OH^*-chemiluminescence images at different phaseshift angles at 200 kg/h main air mass flow rate, 300 K non-preheated air for $\Phi_{Total} = 0.66$. The instability occurred at 82 Hz.

Heat release visualization for different operating points

OH^* chemiluminescence images were also taken at different operating conditions when the pulsation behavior was investigated from rich to lean mixture (Fig. B.7, case "rich-lean"). Note, the tests were also conducted from lean to rich mixture (case "lean-rich") but the hysteresis effect described in several papers (e.g. [56, 92]) could not be observed. Assuming that the heat release is qualitative related to the OH^* chemiluminescence, the highest heat release rate at $\Phi_{Total} \geq 0.6$ could be detected within the shear layer between the side and central recirculation zone (Fig. B.7). The heat release rate at $\Phi_{Total} \leq 0.5$ (close to the lean blowout) could be detected within a greater region of combustion chamber as it can be seen from the OH^* image at $\Phi_{Total} = 0.48$. The right side of the combustor flame seemed to be more intense, especially at $\Phi_{Total} = 0.62$, but this could be attributed to the arrangement of the camera position and the swirl-stabilized burner. In this study, the cross section of the combustor outlet air slots were located in a 45 ° angle to the camera, as displayed in Fig. B.6.

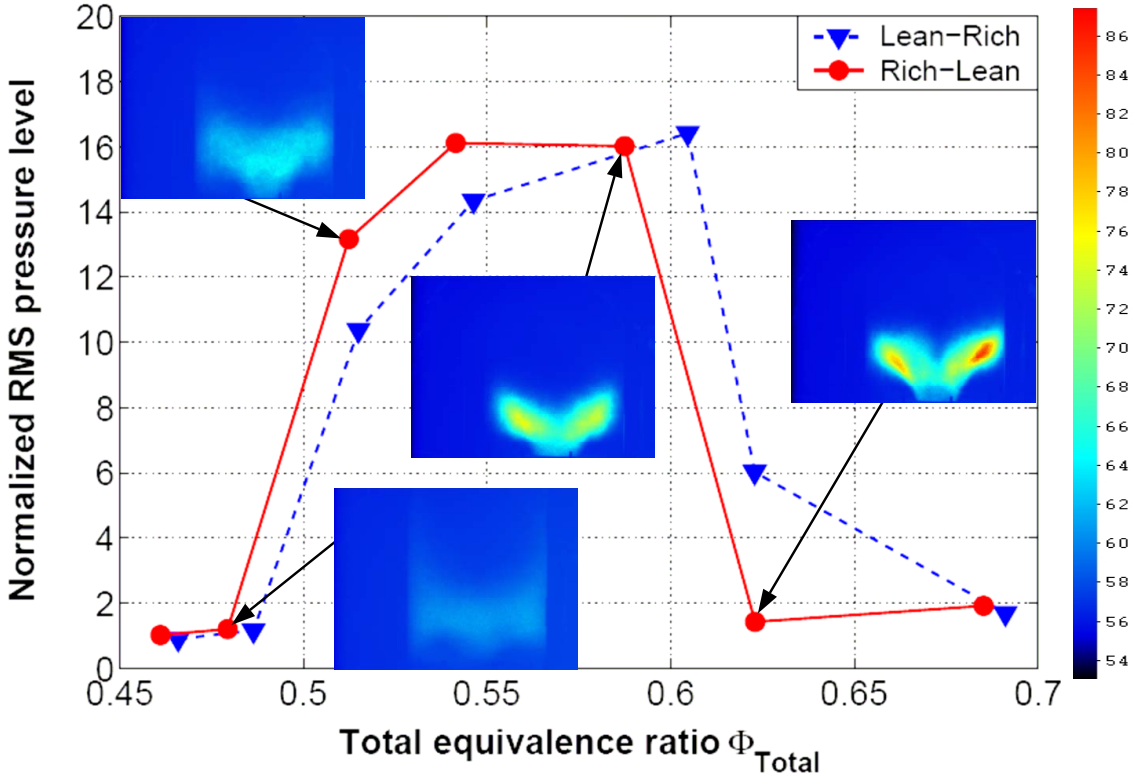

Figure B.7: OH^*-chemiluminescence images and RMS pressure level at different operating points for the case "PFI-550K"; sparkplug was not activated. While for the curve "rich-lean", the pressure fluctuations were investigated from rich mixture to lean mixture, the RMS pressure level were recorded for the curve "lean-rich" at the starting operating point Φ_{Total} near lean blowout. A hysteresis effect was not clearly visible.

Appendix C

Impact of different pilot injection concepts on the "RM" boundary

The impact of different pilot injection concepts on the "RM" boundary were closer investigated and evaluated in terms of its damping effect on p' and on its NO_x formation. While in one concept, a fuel split between the pilot ring and the PFI lance was set, only the premixed ring was activated in the other concept. Further details about the different pilot and ring injection are summarized in table C.1. It will be shown in the following that the injection of fuel/air through the pilot ring is efficient to suppress the instabilities while the NO_x emissions can be kept on low level. Furthermore, it is less complex when compared to the other concepts, where the pilot is injected through both, the PFI lance and the pilot ring.

Many tests without any pilot injection (baseline tests and referred as "1 0 0 0" in the following Figures) have shown that the main combustion at 200 kg/h and 550 K becomes firstly unstable at $\Phi_{Total} = \Phi_{Main} \approx 0.47$ (Fig. C.1 and Fig. C.2). Thereby, Φ_{Total} can be calculated with the following equation:

$$\Phi_{Total} = \left(\frac{\dot{m}_{Fuel,Main}}{\dot{m}_{Air,Total}} + \frac{\dot{m}_{Fuel,Pilot}}{\dot{m}_{Air,Total}}\right) \cdot \frac{1}{FAR_{Stoic}} \tag{C.1}$$

with	$\dot{m}_{Total}$	Total mass flow rate;	$(\dot{m}_{Total} = \dot{m}_{Main} + \dot{m}_{Pilot})$
	$\dot{m}_{Main}$	Main mass flow rate,	
	FAR_{stoic}	Fuel air ratio,	
	$\dot{m}_{Pilot}$	Pilot mass flow rate.	

Note, vertical red bars are included in all figures in this section and define the condition when CO emissions of the baseline case (1 0 0 0) will exceed 1 ppmv limit. To prevent or to delay the p' excitation, one proposal might be to operate the main flame at leaner condition than $\Phi_{Main} = 0.47$ while Φ_{Total} is varied by the amount of pilot fuel through the pilot ring. It is interesting to note that the efficiency of the fuel ring injection seems to be dependent from the parameter Φ_{Main} and Φ_{Total} (Fig. C.1 and Fig. C.3 right column, cases "1 0 0 1.4", "1 0 0 2.0" etc). While the initial increase of p' dependent on Φ_{Main} did not seem to be influenced by increasing the fuel ring mass flow rates from 1.4 to 2.5 kg/h, the initial increase of p' can be significantly delayed when p' versus Φ_{Total} is plotted. Obviously, the instability of the main flame is not influenced by the amount of ring fuel mass flow rate as p' versus on Φ_{Main} shows. The local heat release rate of the diffusion ring flame is only controlled by the local mixing processes so that fluctuations in air and fuel mass flow rates do not lead to higher heat

release fluctuations [59]. Therefore, the initial increase of p' can be delayed to higher Φ_{Total} by increased ring fuel mass flow rate. Unfortunately, the NO_x formation of the diffusion flame adversely affects the global NO_x level and is limited on gas turbine application with low NO_x requirements. Tests with fuel splitting between PFI and pilot ring injection for a constant $\dot{m}_{Fuel,Pilot}$ have been conducted (Fig C.5) to find an optimum between moderate NO_x emissions and the p' level. Thereby, the 50/50 fuel split was the most efficient method to reduce both parameters ("15 1.05 0 0.9"). Even though the tests results with ring fuel injection are promising for some configurations, the premixed ring is more practicable for p' damping without NO_x increase. The damping mechanisms (also described in section 6.3.4) can be explained by the high spreading of $\dot{Q}$ within the combustion chamber and the higher axial momentum of the pilot jet. The ring air injection only is also able to delay the p' increase to richer mixture (Fig. C.3 (a)) but the slope of p' is too high and the impact of ring air injection is not visible in Fig. C.1 (a), p' versus Φ_{Total}. The slope of p' decreases firstly if additional ring fuel is injected and represents the only tested configuration beside the "air ring" (1 0 15 0), where the initial p' increase is delayed to richer mixture (higher Φ_{Main}) when compared to the baseline case. Under these conditions, the delaying effect of p' excitation can be also detected in Fig. C.1 (a) due to the definition of Φ_{Total} (see equation C.1). Further tests with a combined operation of the pilot ring and the PFI lance show, that a PFI injection only in diffusion mode (fuel injection) leads to high pressure oscillations and high NO_x emissions whereas both parameters could be reduced with the combined premixed ring and PFI injection (Fig. C.1 (e)). But, the dynamic stability of the main flame was not improved when compared to the baseline case (Fig. C.3 (e)).

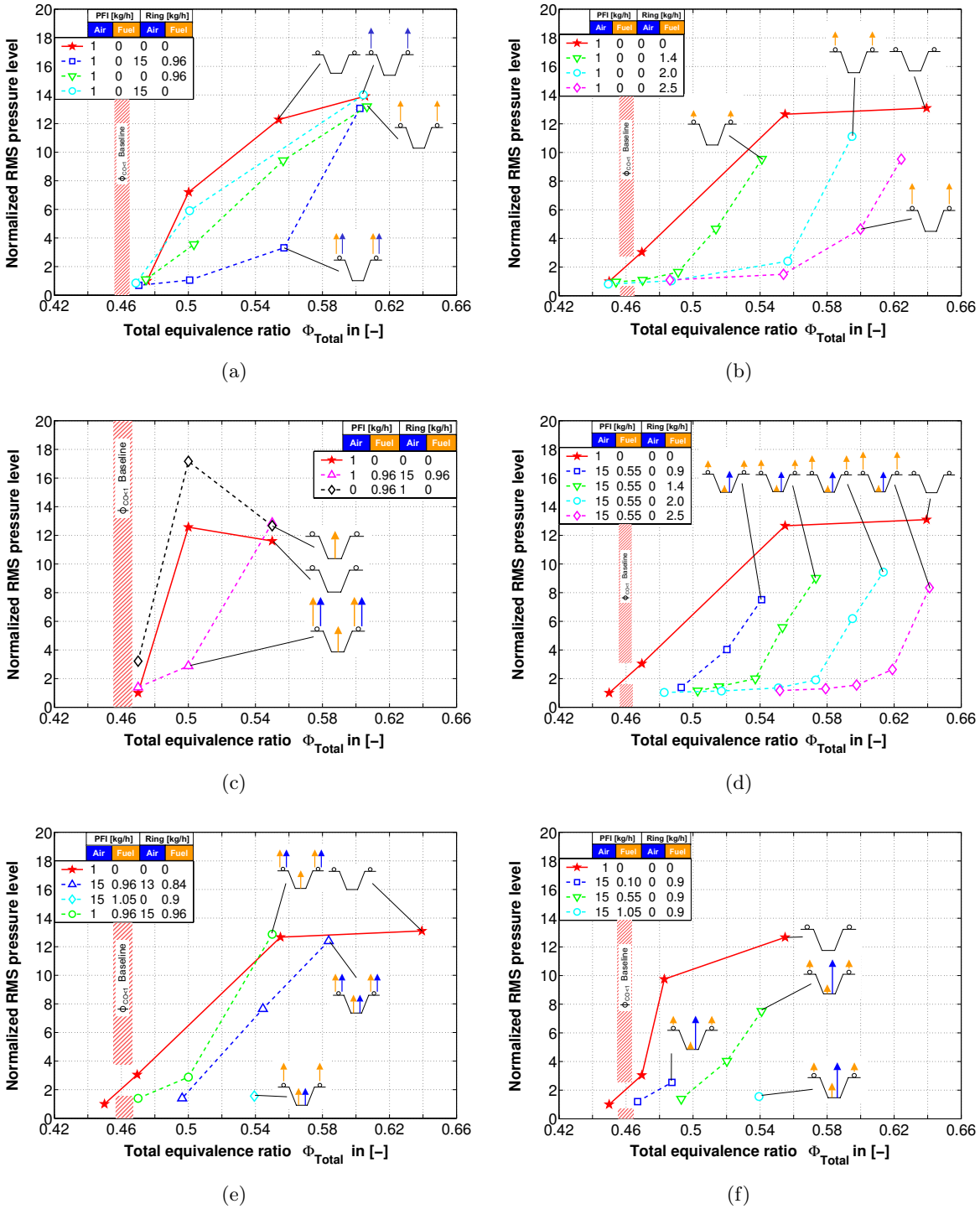

Figure C.1: p' level at different pilot injection locations versus Φ_{Total}: left column of test results show the p' behavior with premixed ring injection, the right column with diffusion ring injection. Simultaneously, the pilot fuel and the pilot air mass flow rate through the PFI lance were varied.

Table C.1: Detailed test conditions with pilot and ring injection. The tests were conducted at constant 200 kg/h main air mass flow rate, 550 K preheat temperature and with a combustion tube of 200 mm diameter.

Pilot air kg/h	**Pilot fuel in kg/h**	**Ring air kg/h**	**Ring fuel kg/h**
0	0.00	0	0.00
0	0.96	15	0.96
0	0.96	0	0.00
1	0.00	0	0.00
15	0.10	0	0.90
15	0.55	0	0.90
15	1.05	0	0.90
1	0.00	0	0.00
0	0.00	0	0.90
0	0.00	0	1.40
0	0.00	0	2.00
0	0.00	0	2.50
1	0.00	0	0.00
15	0.96	13	0.84
1	0.96	15	0.96
15	1.05	0	0.90
1	0.00	0	0.00
15	0.55	0	0.90
15	0.55	0	1.40
15	0.55	0	2.00
15	0.55	0	2.50
15	0.55	0	1.40
15	1.05	0	0.90
15	1.45	0	0.50
15	1.80	0	0.15
15	1.95	0	0.00

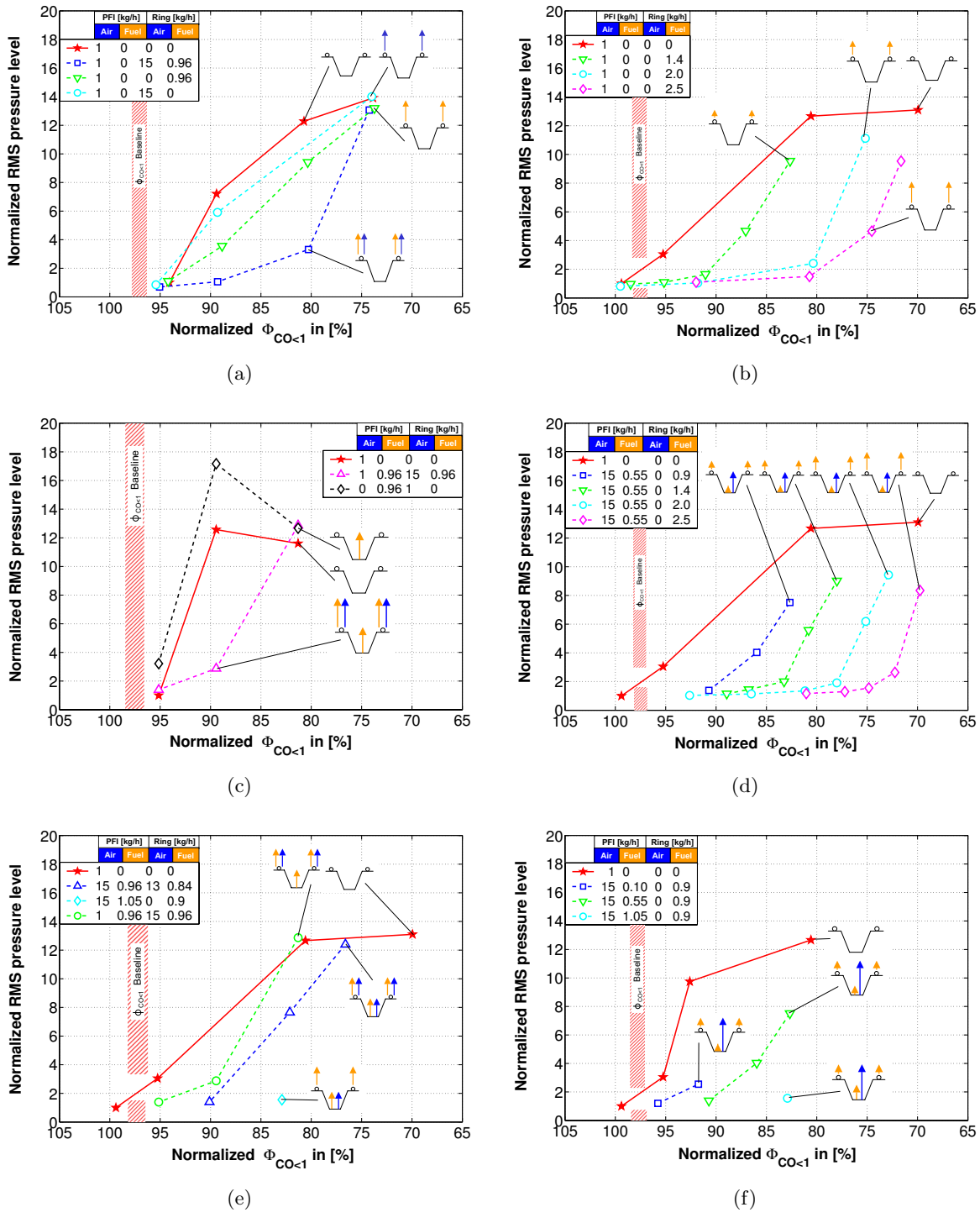

Figure C.2: p' level at different pilot injection locations versus $\Phi_{CO<1}$: left column of test results show the p' behavior with premixed ring injection, the right column with diffusion ring injection. Simultaneously, the pilot fuel and the pilot air mass flow rate through the PFI lance was varied.

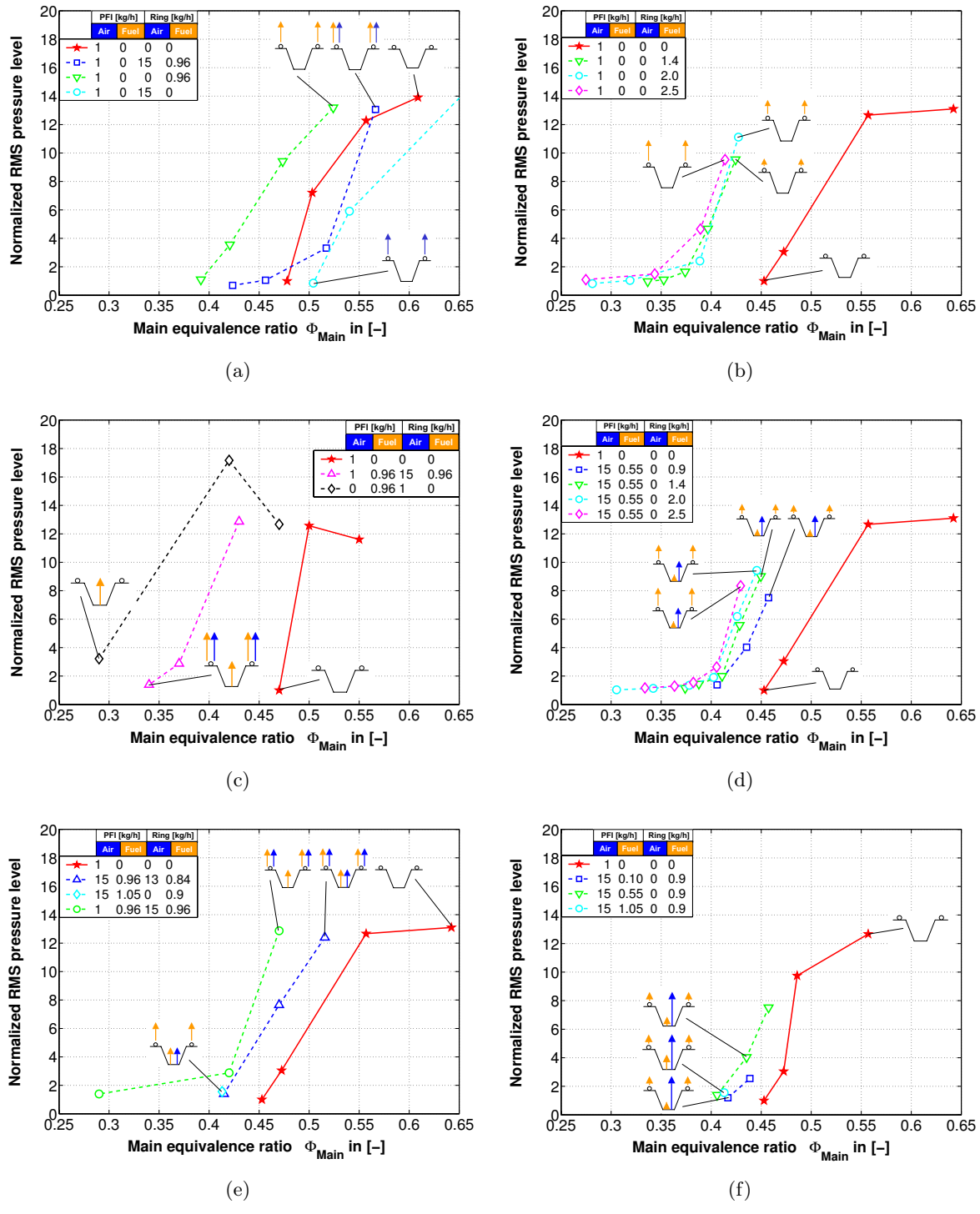

Figure C.3: p' level at different pilot injection locations versus Φ_{Main}: left column of test results show the p' behavior with premixed ring injection, the right column with diffusion ring injection. Simultaneously, the pilot fuel and the pilot air mass flow rate through the PFI lance was varied.

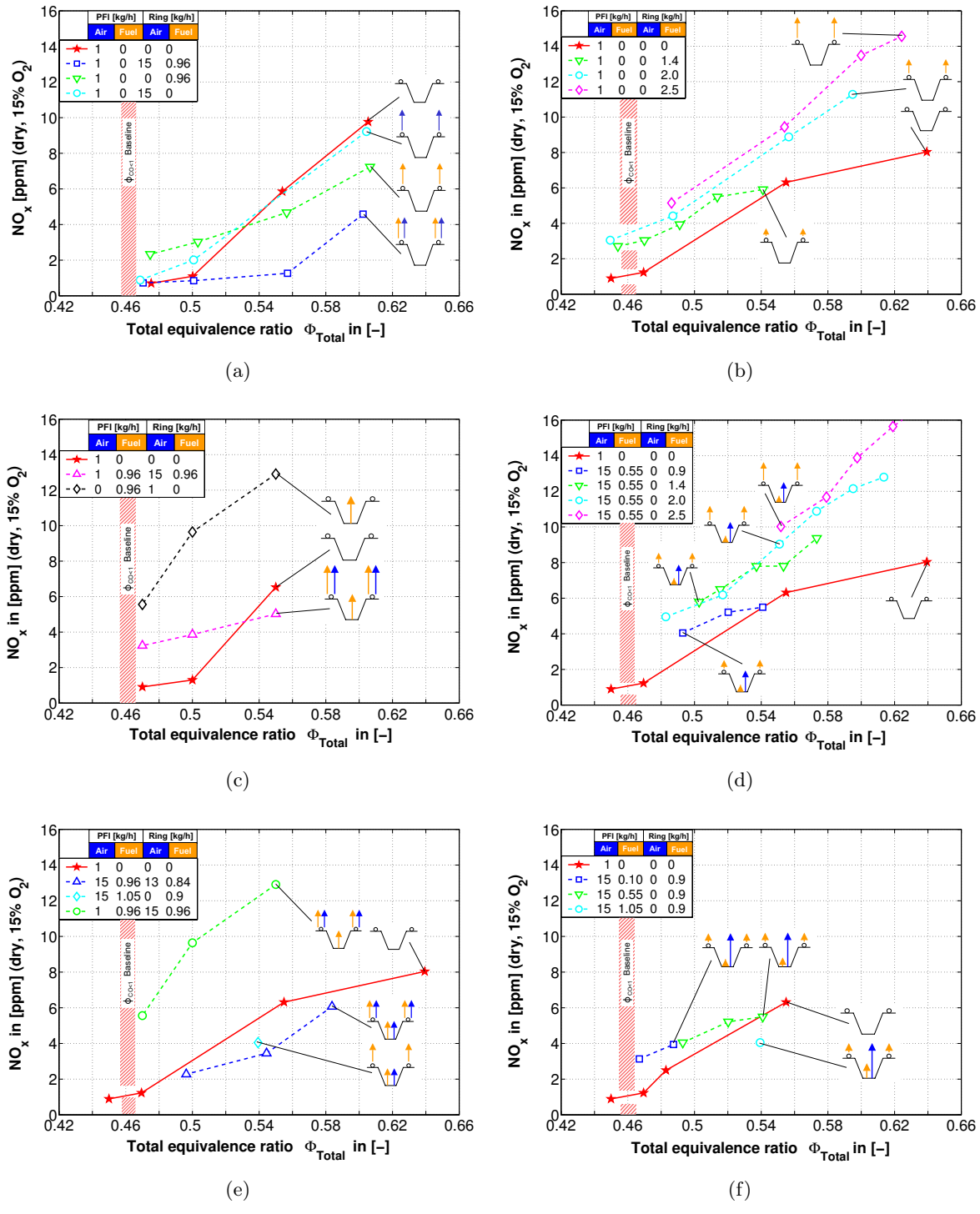

Figure C.4: NO_x level for different pilot injection locations versus Φ_{Total}: left column of test results show the p' behavior with premixed ring injection, the right column with diffusion ring injection. Simultaneously, the pilot fuel and the pilot air mass flow rate through the PFI lance was varied.

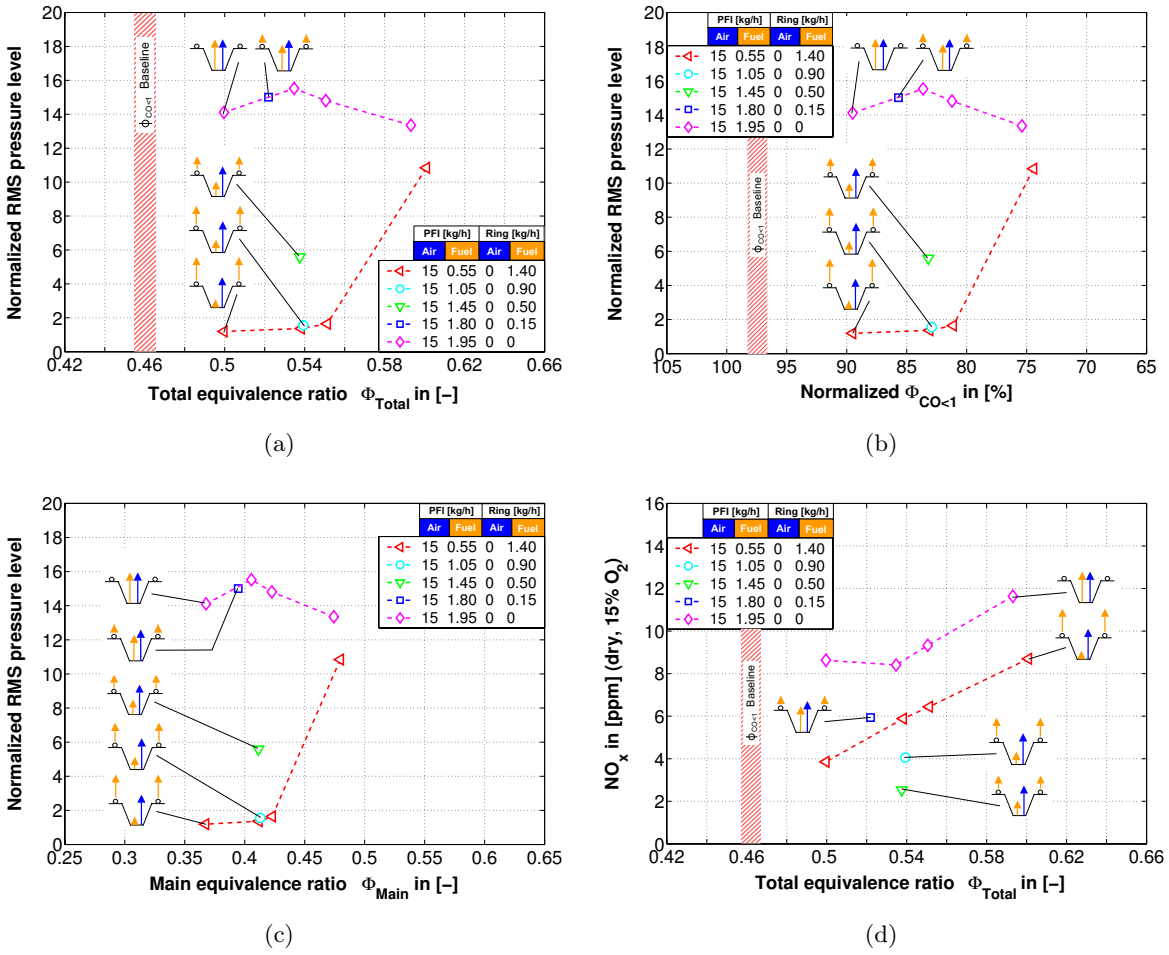

Figure C.5: p' level and NO_x level for different split of ring fuel and PFI fuel. The total pilot mass flow rate was kept constant.

Appendix D

Detailed test conditions of the operating points shown in the stability map (Fig. B.1)

In Fig. B.1 is shown the stability map of the EV-10 combustor for 550 K main air preheat temperature and for three different main air mass flow rates 200 kg/h, 225 kg/h and 250 kg/h with pilot injection while the total equivalence ratios Φ_{Total} was varied. For the pilot injection was chosen 0.33-0.7 kg/h pilot fuel mass flow rate that was only injected into the combustion chamber or was mixtured before injection with pilot air mass flow rates 7.5 kg/h or 10 kg/h.

Table D.1: Investigated operating points for the stability map at 550 K preheat temperature and at a tube diameter of 200 mm. For the pilot injection cases, the pilot mass flow were only injected through the pilot lance (combustor apex) while the spark plug was off. The pilot ring was not installed in these tests.

$\dot{m}_{Main,Air}$ **in kg/h**	$\dot{m}_{Pilot,Air}$ **in kg/h**	$\dot{m}_{Pilot,Fuel}$ **in kg/h**	Φ_{Pilot}
200	−−	−−	−−
225	−−	−−	−−
250	−−	−−	−−
200	−−	0.33	−−
200	−−	0.44	−−
200	−−	0.53	−−
200	7.5	0.33	0.7
200	7.5	0.44	1.0
200	7.5	0.53	1.2
200	−−	0.41	−−
200	−−	0.54	−−
200	−−	0.70	−−
200	10.0	0.41	0.7
200	10.0	0.54	1.0
200	10.0	0.70	1.2

Appendix E

Heat release distribution within the combustion chamber for different pilot injection configurations

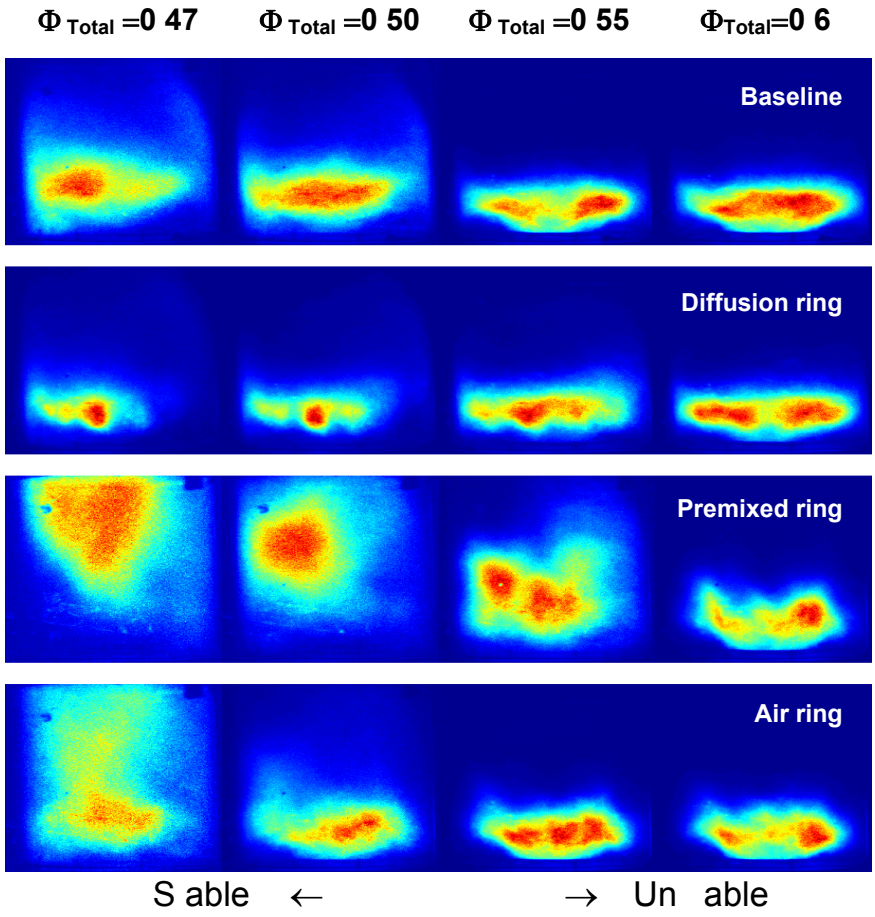

Figure E.1: Heat release distribution within the combustion chamber for different pilot injection configurations.

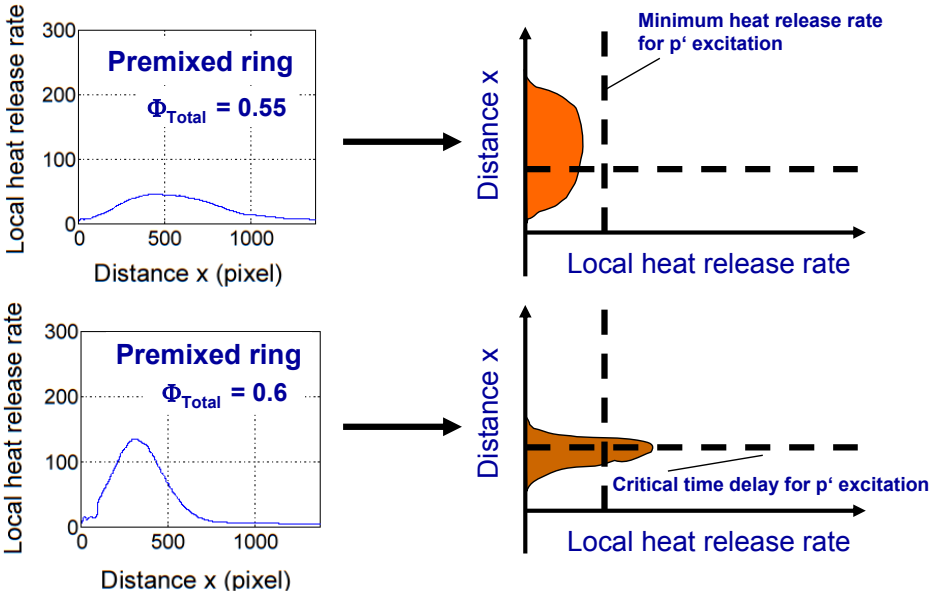

Figure E.2: Heat release distribution in axial direction for the "Premixed ring" case at $\Phi_{Total} = 0.55$ and $\Phi_{Total} = 0.6$. Left graphs are derived from heat release distributions shown in Fig. E.1 while the right graphs are only used for illustration issues and show only the qualitative distribution of the heat release rate at same Φ_{Total}.

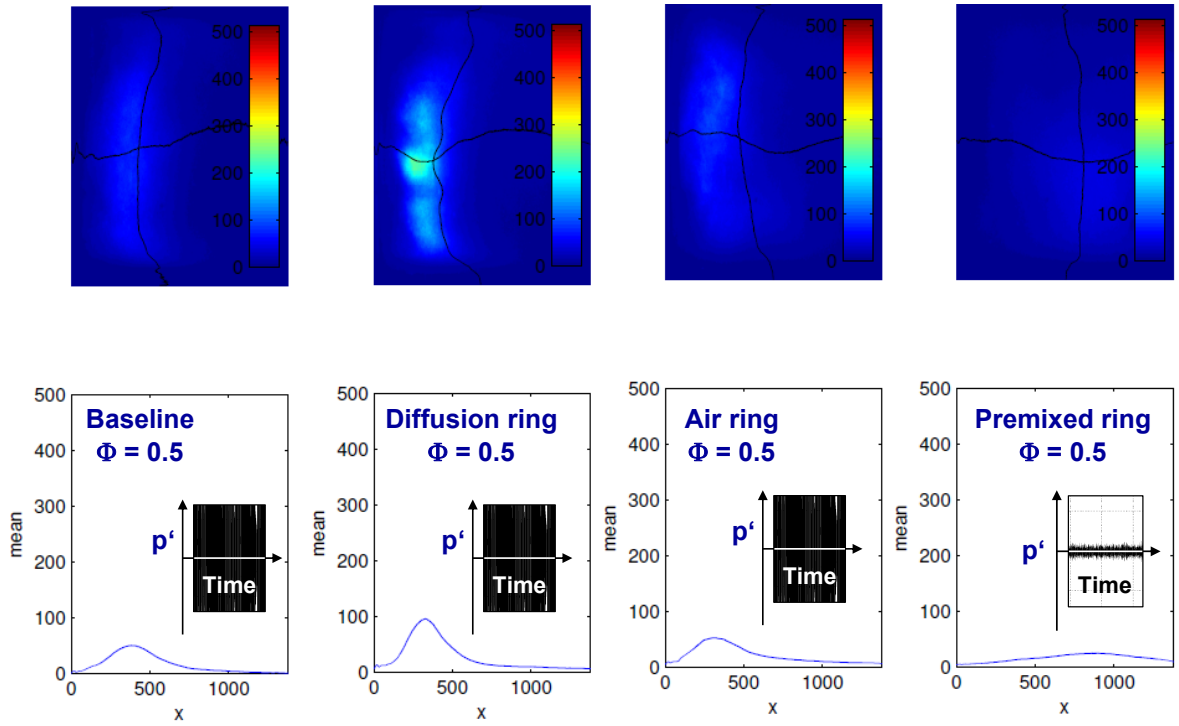

Figure E.3: Local heat release distribution and pressure fluctuation at $\Phi = 0.5$ and different injection location.

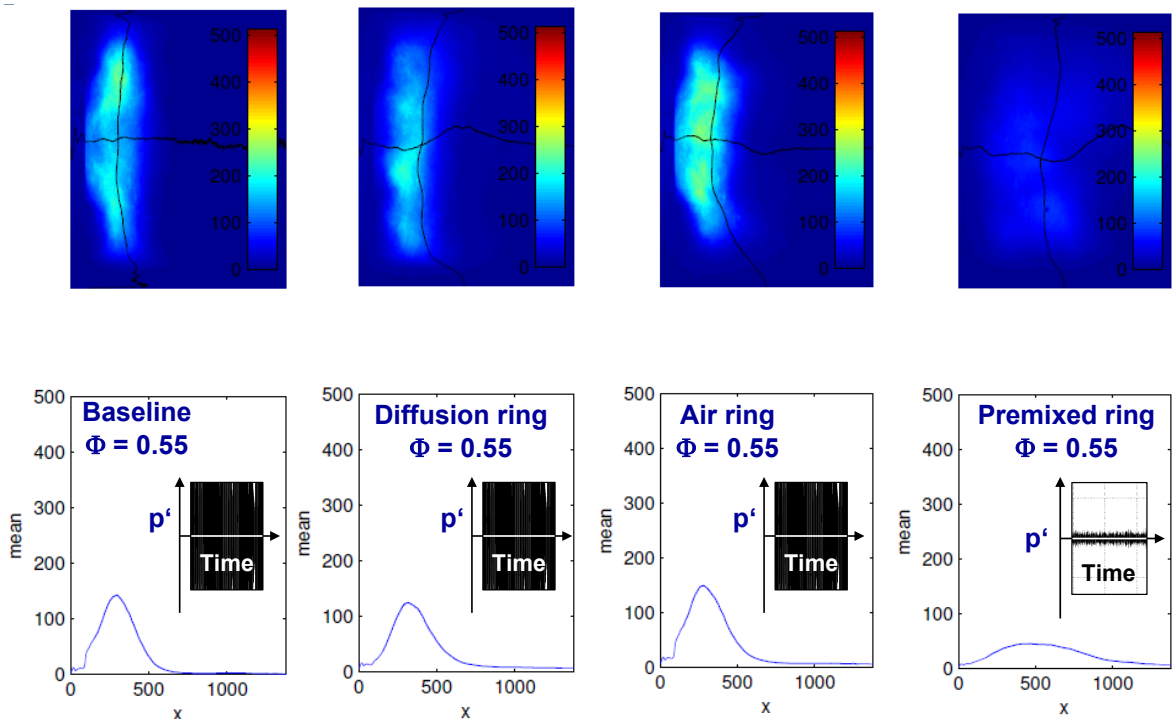

Figure E.4: Local heat release distribution at $\Phi = 0.55$ and different injection location.

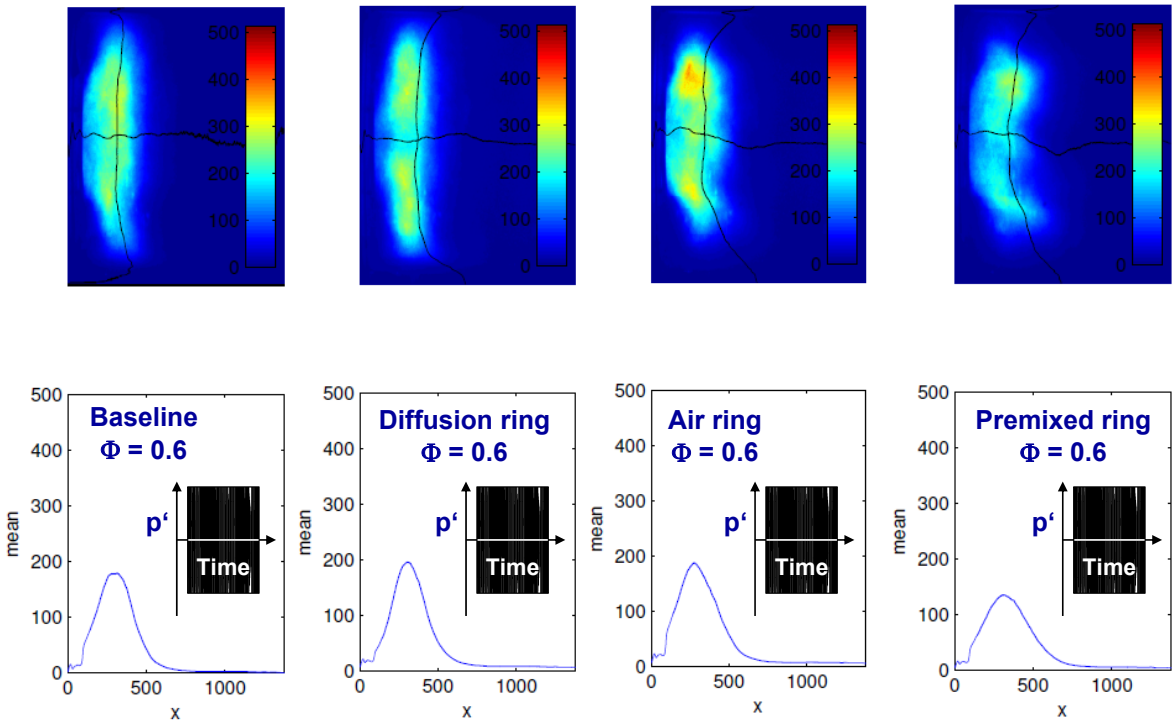

Figure E.5: Local heat release distribution and pressure fluctuation amplitude at $\Phi = 0.6$ and different injection location.

Bibliography

[1] Albrecht, P., 2007a. "Handbuch zum 240 kW Brennkammerprüfstand". Tech. rep.

[2] Albrecht, P., Bade, S., Dinkelacker, F., Gutmark, E., and Paschereit, C. O., 2009. "Pilot-premix flames: Higher operational flexibility in gas turbines without NOx increase". ASME GT2009-59181.

[3] Albrecht, P., Bauermeister, F., Bothien, M., Lacarelle, A., Moeck, J., o. Paschereit, C., and Gutmark, E., 2006. "Characterization and control of lean blowout using periodically generated flame balls". ASME 2006-GT-90340.

[4] Albrecht, P., Speck, S., Schimek, S., Bauermeister, F., Paschereit, C. O., and Gutmark, E., 2007. "Lean Blowout Control using an Auxiliary Premixed Flame in a Swirl-Stabilized Combustor". AIAA 2007-5632.

[5] Anderson, D. N., 1975. "Effects of Equivalence Ratio and Dwell Time on Exhaust Emissions from an Experimental Premixed Prevaporizing Burner". ASME 75-GT-69.

[6] Armbruster, J., 1996. *Flugverkehr und Umwelt: Wieviel Mobilität tut uns gut?* Springer. ISBN 3540603093.

[7] Armengaud, 1907. French patent. No. 376176.

[8] Ashurst, W. T., and Shepherd, I. G., 1997. "Flame front curvature distributions in a turbulent premixed flame zone". *Combust. Sci. and Tech.,* **124**, pp. 115–144.

[9] Bade, S., 2007. "Stabilitäets- und Emissionsuntersuchung einer verdrallten Vormischflamme nahe der Verlöschgrenze". Master's thesis, TU Berlin, Hermann-Foettinger-Institut.

[10] Ballal, D., and Lefebvre, A., 1979. "Weak extinction limits of turbulent flowing mixtures". *Journal of Engineering for Power,* **101**(3), pp. 343–348.

[11] Ballal, D., and Lefebvre, A. H., 1981. "Some fundamental aspects of flame stabilization". *Fifth international symposium on air breathing engines*, pp. 48.1–48.8.

[12] Basler, B., 2001. "Power plant emission reduction potentials achievements and future reduction potentials". 18th World Energy Congress, Buenos Aires, October 2001.

[13] Bauermeister, F., 2005. "Erstellung von Programmmodulen unter LabVIEW zur überwachung und Regelung eines Brennkammerprüfstand". Master's thesis, TU Berlin, Hermann-Föttinger-Institut.

[14] Bauermeister, F., and Schroedinger, C., 2007. Dokumentation der Abgasanlage. Tech. rep., Institut fuer Stroemungsmechanik und Technische Akustik.

[15] Baukal, C. E., 2004. *Industrial combustion pollution and control.* Marcel Dekker, Inc., New York, Basel.

[16] Beer, J., and Chigier, N. A., 1972. *Combustion aerodynamics.* Applied Science.

[17] Bothien, M. R., Moeck, J. P., and Paschereit, C. O., 2008. "Assessment of Different Actuator Concepts for Acoustic Boundary Control of a Premixed Combustor". ASME Turbo Expo 2008, June 9-13, Berlin. GT2008-50171.

[18] Conrwell, M., 2005. "Flameless combustion for high pressure ratio gas turbine engines". presented at the Flameless Combustion Workshop, Lund, Sweden June 19-21.

[19] Correa, S. M., 1991. "Lean Premixed Combustion for Gas Turbines: Review and Required Research". *Fossil Fuel Combustion.* ASME PD-Vol. 33.

[20] Dinkelacker, F., 2001. *Struktur Turbulenter Vormischflammen.* Lehrstuhl für Technische Thermodynamik, Technische Fakultät Friedrich-Alexander-Universität Erlangen-Nürnberg.

[21] Dinkelacker, F., Soika, A., Most, D., Hoffmann, D., Leipertz, A., Polifke, W., and Doebberling, K., 1998. "Structure of locally quenched highly turbulent lean premixed flames". *Twenty-Seventh Symposium (International) on Combustion/The Combustion Institute,* **27**, pp. 857–865.

[22] Eckbreth, A. C., 1988. *Laser diagnostics for combustion temperature and species.* Abacus Press. ISBN 0-85626-344-3.

[23] Energy Agency, I., 2003. *Energy to 2050 scenarios for a sustainable future.* IEA, *http : //www.iea.org/Textbase/publications/free_all.asp.*

[24] Esnault-Pelterie, 1906. French patent. No. 373141.

[25] Fenimore, C. P., 1971. "Formation of Nitric Oxide in Premixed Hydrocarbon Flames". *The Combustion Institute, Thirteenth Symposium (International) on Combustion,* **13**, pp. 373–380.

[26] Fischer, A., 2004. "Hybride, thermoakustische Charakterisierung von Drallbrennern". PhD thesis, Lehrstuhl für Thermodynamik, Technische Universität München.

[27] Fritsche, D., 2005. "Origin and Control of Thermoacoustic Instabilities in LeanGas Turbine Combustion". PhD thesis, Swiss Federal Institute of Technology Zurich, Swiss.

[28] Gaydon, A., 1974. *The Spectroscopy of Flames.* Chapman & Hall.

[29] Giezendanner, R., Keck, O., Weigand, P., Meier, W., Meier, U., Stricker, W., and Aigner, M., 2003. "Periodic combustion instabilities in a swirl burner studied by phase-locked planar laser-induced fluorescence". *Combustion Science and technology,* **175**, pp. 721–741.

[30] Gobbe, 1900. German patent. No. 118917.

[31] Gobbe, 1925. German patent. No. 441337.

[32] Gupta, S. B., Sekar, R., and Hillman, G. E., 2006. Laser based ignition system for natural gas reciprocating engines, laser based ignition system having capability to detect sucessfully detect ignition event; and distributor system for use with high-powered pulsed lasers. Patente US 7,114,858 B2.

[33] H. N. Najm And, P. H. P., Mueller, C. J., and Wyckoff, P. S., 1998. "On the adequacy of certain experimental observables as measurements of flame burning rate". *Combustion and Flame,* **113**, pp. 312–322.

[34] Hedman, P. O., 2002. "Observations of Flame Behavior in a Laboratory-Scale premixed Natural Gas/Air Gas Turbine Combustor from LDA Velocity Measurements". GT-2002-30053.

[35] Hermsmeyer, H., Prade, B., Gruschka, U., Schmitz, U., Hoffmann, S., and Krebs, W., 2002. "V64.3a Gas Turbine Natural Gas Burner Development". ASME GT-2002-30106.

[36] Hirschl, B., 2008. *Energiepolitik und Klimaschutz: Eine Multi-Level Policy-Analyse mit Focus auf den deutschen Strommarkt.* VS Research. ISBN 978-3-8350-7024-0.

[37] Huang, Y., and Yang, V., 2004. "Bifurcation of flame structure in a lean-premixedswirl-stabilized combustor: transition from stable tounstable flame". *Combustion and Flame,* **136**, pp. 383–389.

[38] István, S., 1984. *Einführung in die technische Mechanik.* Springer. ISBN 3-540-13293-7.

[39] Joos, F., 2006. *Technische Verbrennung: Verbrennungstechnik, Verbrennungsmodellierung, Emissionen.* Springer, Germany.

[40] Kaneshige, M., 1999. Detonations in mixtures containing nitrous oxide. 22nd international symposium on shock waves, july 18-23, Imperial College, London, UK, Paper 1640.

[41] Karawodine, 1906. French patent. No. 374124.

[42] Keller, J., 1995. "Thermoacoustic oscillations in combustion chambers of gas turbines". *AIAA journal, Vol. 33, No. 12, december*, pp. 2280–2287.

[43] Kendrick, D. W., Anderson, T. J., Sowa, W. A., and Snyder, T., 1999. "Acoustic Sensitivities of Lean-Premixed Fuel Injectors in a Single Nozzle Rig". *Journal of Engineering for Gas Turbines and Power,* **121**, pp. 429–436.

[44] Kokanovic, S., Guidati, G., Torchalla, S., and Schuermans, B., 2006. "Active combustion control system for reduction of nox and pulsation levels in gas turbines". ASME GT2006-90895.

[45] Kopitz, J., Huber, A., Sattelmayer, T., and Polifke, W., 2005. Thermoacoustic stability analysis of an annular combustion chamber with acoustic low order modeling and validation against experiment. Gt2005-68797.

[46] Kuechler, A., 2005. *Hochspannungstechnik.* Springer, Germany.

[47] Kunze, K., 2004. "Untersuchung des thermoakustischen Flammenübertragungsverhaltens in einer Ringbrennkammer". PhD thesis, Lehrstuhl für Thermodynamik, TU München.

[48] Kunze, K., 2004. "Untersuchung des thermoakustischen flammenübertragungsverhaltens in einer ringbrennkammer". PhD thesis, Lehrstuhl fuer Thermodynamik, Technische Universitaet Muenchen, Germany.

[49] Lacarelle, A., Faustmann, T., Greenblatt, D., Paschereit, C. O., Lehmann, O., Luchtenburg, D. M., and Noack, B. R., 2008. "Spatio-temporal characterization of a conical swirler flow field under strong forcing". GT2008-50970.

[50] Langhorne, P., 1988. "Reheat Buzz: An acoustically coupled Combustion Instability. Part i. Experiment". *J. Fluid Mech.,* **193**, pp. 417–443.

[51] Lechner, C., and Baukal, J. S., 2003. *Stationäre Gasturbinen.* Springer,VDI, Germany.

[52] Lee, J. G., and Santavicca, D. A., 2003. "Experimental Diagnostics for the Study of Combustion Instabilities in Lean Premixed Combustors". *Journal of Propulsion and Power,* **19**(5), pp. 735–750.

[53] Lenz, M., 1998. Experimentelle Optimierung des Stabilitätverhaltens von Gasturbinenbrenner. Tech. rep., Germany, University Erlangen-Nuernberg, Chair of Technical Thermodynamics.

[54] Leonard, G., and Stegmaier, J., 1993. "Development of an Aeroderivative Gas Turbine Dry Low Emissions Combustion System". *Journal of Engineering for Gas Turbine and Power,* **116**, pp. 542–546.

[55] Leonard, G. L., and Correa, S. M., 1990. "NOx Formation in Lean Premixed High-Pressure Methane Flames". *Second ASME Fossil Fuel Combustion Symposium,* **30**, pp. 69–74.

[56] Lepers, J., Krebs, W., Prade, B., Flohr, P., Pollarolo, G., and Ferrante, A., 2005. "Investigation of Thermoacoustic Stability Limits of an Annular Gas Turbine Combustor Test-Rig with and without Helmholtzresonators". ASME GT-2005-68246.

[57] Lieuwen, T., Torres, H., Johnson, C., and Zinn, B. T., 2001. "A Mechanism of Combustion Instability in Lean Premixed Gas Turbine Combustors". *Journal of Engineering for Gas Turbines and Power,* **123**, pp. 184–189.

[58] Lieuwen, T., and Wu, L., 2003. "Coherent acoustic Wave Amplification/Damping by wrinkled Flames". 41st AIAA Aerospace Sciences Meeting and Exhibit, Reno, Nevada. AIAA-2003-0114.

[59] Lieuwen, T., and Yang, V., 2005. *Combustion In in Gas Turbine Engines.* American Institute of Aeronautics and Astronautics.

[60] Lieuwen, T., and Zinn, B. T., 1998. "The Role of Equivalence Ratio Oscillations in driving Combustion Instabilities in low-NOx Gas Turbines". *Twenty-Seventh Symposium (International) on Combustion /The Combustion Institute,* **27**, pp. 1809–1816.

[61] Longwell, J. P., Frost, E. E., and Weis, M. A., 1953. "Flame stability in bluff body recirculation zones". *Journal of Industrial and Engineering Chemistry,* **45**, pp. 1629–1633.

[62] Marconnet, 1910. French patent. No. 412478.

[63] Merryman, E. L., and Levy, A., 1975. "Nitric Oxides Formation in Flames: The Role of NO2 and Fuel Nitrogen". *The Combustion Institute, Fifteenth Symposium (International) on Combustion,* **15**, pp. 1073–1083.

[64] Moesl, K. G., Vollmer, K. G., Sattelmayer, T., Eckstein, J., and Kopecek, H., 2008. "Experimental Study on Laser-Induced Ignition of Swirl-Stabilized Kerosene Flames". ASME Turbo Expo 2008, June 9-13, Berlin. GT2008?50487.

[65] Mortimer, C. E., 2003. *Chemie-Das Basiswissen der Chemie.* Thieme, Germany.

[66] Nair, S., and Lieuwen, T., 2003. "Acoustic Detection of Imminent Blowout in Pilot and Swirl Stabilized Combustors". ASME GT2003-38074.

[67] Nicol, D., Malte, P., Lai, J., Marinov, N., and Pratt, D. T., 1992. "Nox Sensitivities for Gas Turbine Engine Operated on Lean-Premixed Combustion and Conventional Diffusion Flames". ASME 92-GT-115.

[68] Paschereit, C., Schuermanns, B., and Bueche, D., 2003. "Combustion Process Optimization using Evolutionary Algorithm". ASME Paper 2003-GT-38393.

[69] Paschereit, C., Schuermans, B., and Campos-Delgado, D., 2001. "Active Combustion Control using an Evolution Algorithm". AIAA 2001-0783.

[70] Paschereit, C. O., and Gutmark, E., 2004. "The Effectiveness in Passive Combustion Control Methods". ASME Paper 2004-GT-53587.

[71] Paschereit, C. O., Gutmark, E., and Weisenstein, W., 1999. "Control of Thermoacoustic Instabilities in a Premixed Combustor by Fuel Modulation". AIAA Paper 99-0711.

[72] Paschereit, C. O., and Gutmark, E. J., 2008. "Combustion Instability and Emissions Control by Pulsating Fuel Injection". *submitted at the Journal of Turbomachinery and was accepted.*

[73] Pelster, R., Pieper, R., and Huettl, I., 2005. "Thermospannungen- viel genutzt und fast immer falsch erklärt!". *Physik und Didaktik in Schule und Hochschule,* **PhyDid 1/4**, pp. 10–22.

[74] Poinsot, T. J., Trouve, A. C., Veynante, D. P., Candel, S. M., and Esposito, E. J., 1987. "Vortex-driven acoustically coupled combustion instabilities". *Journal of Fluid Mechanics,* **177**, pp. 265–292.

[75] Prakash, S., Neumeier, Y., and Zinn, B. T., 2007. "Blowout margin estimation based on two precursor types". ASME GT2007-27874.

[76] Putnam, A. A., and Dennis, W., 1953. "A study of burner oscillations of the organ-pipe type". *Transactions of the American Society of Mechanical Engineers, vol. 75, pp. 15-28.*

[77] Rao, K. V., and Lefebvre, A. H., 1982. "Flame blowoff studies using large-scale flameholders". *Journal of Engineering for Power,* **104**, pp. 853–857.

[78] Ratliff, P., Garbett, P., and Fischer, W., 2007. "SGT5-8000H: Grösserer Kundennutzen durch die neue Gasturbine von Siemens". *VGB Powertech.*

[79] Rebhan, E., 2002. *Energiehandbuch: Gewinnung, Wandlung Nutzung von Energie*. VDI. ISBN 978-3-540-41259-5.

[80] Reynst, 1949. German patent. No. 944260.

[81] Reynst, F., 1955. Pulsating, pressure generating combustion systems for gas turbines. ASME 55–a-56.

[82] Richards, G., Yip, M., Robey, E., Cowell, L., and Rawlins, D., 1995. Combustion oscillation control by cyclic fuel injection. presented at the International Gas Turbine and Aeroengine Congress and Exposition, Houston, Texas, 95-GT-224.

[83] Rizk, N. K., and Lefebvre, A. H., 1986. "The relationship between flame stability and drag of bluff-body flameholders". *Journal of Propulsion and Power,* **2**(4), pp. 361–365.

[84] Roy, J., Frolov, S., Borisov, A., and Netzer, D., 2004. "Pulse detonation propulsion: Challenges, current status and future perspectives". *Progess in Energy and combustion science,* **30**, p. 562.

[85] Ryan, W., 2004. Method and appartuses for laser ignited engines. Patente US 6,796,278 B2.

[86] Scarinci, T., and Freeman, C., 2000. "The Propagation Of A Fuel-Air Ratio disturbance In A Simple Premixer And Its Influence On Pressure Wave Amplification". ASME Paper 2000-GT-0106.

[87] Scarinci, T., Freeman, C., and Day, I., 2004. "Passive Control of Combustion Instability in a low Emissions Aeroderivative Gas Turbine".

[88] Schade, H., and Kunz, E., 1989. *Strömungslehre*, Vol. 2., durchgesehene und verbesserte Auflage. deGruyter Lehrbuch.

[89] Schildmacher, K.-U., Koch, R., and Bauer, H.-J., 2006. "Experimental Characterization of premixed Flame Instabilities of a Model Gas Turbine Burner". *Flow, Turbulence and Combustion,* **76**, pp. 177–197.

[90] Schmidt, 1930. German patent. No. 532655.

[91] Seaton, A., MacNee, W., Donaldson, K., and Godden, E., 1995. "Particulate Air Pollution and Acute Health Effects". *Lancet,* **345**, pp. 176–178.

[92] Seo, S., 1999. "Parametric Study of Lean Premixed Combustion Instability in a Pressurized model gas turbine combustor". PhD thesis, The Pennsylvania State University, Department of Mechanical and Nuclear Engineering, USA.

[93] Shih, W.-P., Lee, J. G., and Santavicca, D.-A., 1996. "Stability and Emissions Characteristics of a Lean Premixed Gas Turbine Combustor". *The Combustion Institute,* **27**, pp. 2771–2778.

[94] Spalding, D., 1953. "Theoretical aspects of flame stabilization". *Aircraft engineering,* **25**, pp. 264–276.

[95] Speck, S., 2007. "Experimentelle Untersuchung von periodisch erzeugten Flammenbällen bei Variation der Randbedingungen". Master's thesis, Berlin Institutes of Technologies.

[96] Steele, R., Jarret, A., Malte, P., Tonouchi, J., and Nicol, D., 1995. "Variables affecting NOx Formation in Lean-Premixed Combustion". ASME 95-GT-107.

[97] Strube, G., 1993. "Struktur und Brenngeschwindigkeit turbulenter, vorgemischter Wasserstoff-Flammen". PhD thesis, Lehrstuhl A für Thermodynamik, TU München. BIB 8Ve8697.

[98] Sturgess, G. J., Zelina, J., Shouse, D. T., and Roquemore, W. M., 2005. "Emissions reduction technologies for military gas turbine engines". *Journal of Propulsion and Power,* **21**(2), pp. 194–217.

[99] Taupin, B., Vauchelles, D., Cabot, G., and Boukhalfa, A., 2002. Experimental Study of Lean Premixed Turbulent Combustion. l'universite saint Etienne du Rouvray (france).

[100] Wilhelm, K., 1999. Methoden der Regelung in der Luft- und Raumfahrt. Tech. rep., TU Berlin, Institut für Luft- und Raumfahrt.

[101] Wilson, K., Gutmark, E., and Schadow, K., 1992. "Flame-kernel pulse actuator for active combustion control". ASME winter annual meeting.

[102] Wuenning, J., and Wuenning, J. G., 1997. "Flameless oxidation to reduce thermal NO-formation". *Prog. Energy Combust. Sci.,* **23**(0360-1285/97), pp. 81–94.

[103] Zeldovich, J., 1946. "The oxidation of nitrogen in combustion and explosion". *Acta Physiochimica U.R.S.S., Academy of Science USSR,* **21**(4), p. 557.

[104] Zubay, E. A. D., 1950. "Characteristics of disk-controlled flames". *Aero Digest,* **61**(1), pp. 54–56, 102–104.

Acknowledgement

This thesis was mainly driven and supported by the following colleagues:

My thesis advisor, Prof. C. O. Paschereit, has to be especially thanked for his guidance, financial support of my project and for the opportunity to be his first assistant. I would like to thank Prof. F. Dinkelacker for refereeing this thesis and for the fruitful discussions. Moreover, special thanks goes to distinguished Prof. E. Gutmark. During my 1-month-stay in his laboratory, University of Cincinnati, Ohio, I was able to collect first experiences with explosive gases and with the high voltage ignition system. Without his support and suggestions in the beginning, I would never have found the initial idea for my work. Finally, I would like to thank all post docs, Ph.D. students, students and the technical staff of the institute for their help and support. Thereby, especially A. Lacarelle, S. Bade, Th. Renner, F. Bauermeister, V. Krawcyk, S. Schimek, S. Speck, W. Postel, H. Metchen, Th. Dessin, A. Bendiks, M. Trumper, J. Kaschenz, L. Lindemann, E. Kulzer and A. Paetzold are gratefully acknowledged.